Alma Mater Studiorum – Università di Bologna

DOTTORATO DI RICERCA IN

INGEGNERIA ELETTRONICA, TELECOMUNICAZIONI
E TECNOLOGIE DELL'INFORMAZIONE

Ciclo XXVIII

Settore Concorsuale di afferenza: 09/F1

Settore Scientifico disciplinare: ING-INF/02

CONTACTLESS ENERGY TRANSFER TECHNIQUES FOR INDUSTRIAL APPLICATIONS. POWER AND DATA TRANSFER TO MOVING PARTS

Presentata da: Riccardo Trevisan

Coordinatore Dottorato

Prof. Alessandro Vanelli-Coralli

Relatori

Chiar.ma Prof.ssa Ing. Alessandra Costanzo

Chiar.mo Prof. Ing. Tullio Salmon Cinotti

Correlatori

Prof. Ing. Diego Masotti

Ing. Dario Rea

Roberto Romagnoli

Esame finale anno 2016

To my family:

Sonia and Daniele

Abstract

This doctoral thesis is based on high-apprentice PhD carried out with the University of Bologna and I.M.A. – Industria Macchine Automatiche SpA based in Ozzano dell'Emilia, Bologna, Italy. IMA is a public company and world leader in the design and manufacture of automatic machines for the processing and packaging of pharmaceuticals, cosmetics, food, tea, coffee, and other dairy products.

Contactless energy transfer (CET) systems are gaining increasing interest in the automatic machinery industries. For this reason, circuit equivalent networks of CET systems considered in the literature are introduced with emphasis on their industrial applicability. The main operating principles and the required compensating networks, along with different topologies of power supplies optimised for wireless powering, are discussed. The analysis of the wireless transfer, at the maximum efficiency, of high power levels shows that, in the kHz range, highly coupled inductive links are needed and soft-switching power sources required. The employment of CET units in controlled systems requires combining a link for data communication with the wireless power channel. At low frequencies, capacitive and inductive couplings are integrated in a unique platform to implement the wireless data and power links, respectively. Differently, at UHF, an increased data channel transfer efficiency is made possible by exploiting auto-resonant structures, such as split-

ring resonators instead of capacitances, one at each far-end side of the link. The design procedure of a power CET system, including the dc/ac converter, a rotary transformer and its windings, is discussed and the results presented. A different version of a WPT system, which involves multiple transmitting coils and a sliding receiver, is also presented. A low frequency RFID capacitive data link is then combined with the rotary CET unit to provide the temperature feedback of a controlled system, wherein the rectifying part of a passive tag is exploited to simultaneously power and read a temperature probe. Subsequently, a split-ring based near-field UHF data link is designed to ensure an improved temperature detection in terms of accuracy and resolution. The sensor readout is performed at the transmitter side by measuring the reflected power by the load rectifier.

Contents

Abstract **i**

Contents **iii**

List of Figures **vii**

List of Tables **xi**

Abbreviations **xiii**

Introduction **xv**

1 Inductive Power Transfer **1**

1.1 Inductive Coupling 3

1.2 Compensation 5

1.3 Efficiency 7

1.4 Power Transfer Capability 8

1.5 Contactless Energy Transfer 9

1.5.1 Alternative Electrical Equivalent Representation . 11

1.5.2 Efficiency 12

1.5.3 Compensation 13

1.5.4 Losses 15

1.6 CET Systems 19

1.6.1 Power Transmitter 21

1.6.2 WPT Link 22
1.6.3 Power Receiver 26

2 Power Supplies for WPT **27**

2.1 Voltage-current Behaviour of the IPT System 28
2.2 A Voltage-fed IPT Converter: ZVS-PS Inverter 30
2.3 A Current-fed IPT Converter: CF-PR-PP Inverter 34
2.4 A Hybrid IPT Converter: LCL Resonant Power Supply . 38

3 Wireless Sensing **41**

3.1 RFID Sensing 43
3.1.1 System Operation 44
3.1.2 Theory Formulation 45
3.1.3 Chipless Sensing 47
3.1.4 Temperature Sensing 48
3.2 Direct Passive Sensing 49
3.2.1 Reflected Power Sensitivity 50
3.2.2 RF Rectifier for Industrial DC Probes 52
3.2.3 Link Attenuation of Power Sensitivity 53
3.2.4 Reflected Power Isolation 53

4 Industrial IPT Systems **55**

4.1 A Rotary CET Unit 58
4.1.1 CET System Design 58
4.1.2 Thermal Analysis 61
4.1.3 Experimental Setups 63
4.1.4 Results 68
4.1.5 Remarks 73
4.2 A Sliding WPT Application 73
4.2.1 Analysis and Design 74

4.2.2 Circuit Simulation 77
4.2.3 Remarks 79

5 Passive Sensing for WPT Systems 81
5.1 WPT with Temperature Sensing at UHF 82
5.1.1 Capacitive Data Channel 82
5.1.2 Direct Passive Sensing Implementation 84
5.1.3 Experimental System Results 85
5.1.4 Remarks 89
5.2 UHF Sensing Link 89
5.2.1 Near-Field Resonating Link 90
5.2.2 Experimental Setup 94
5.2.3 Single SRR 94
5.2.4 Reactive link based on two faced SRRs 96
5.2.5 Experimental System Results 99
5.2.6 Remarks 106

Conclusions 107

Acknowledgements 111

List of Achievements 113

Bibliography 115

List of Figures

1 Nikola Tesla's sketch of his experiment on the transmission of energy without wires. xvi

2 Example of a disassembled pot core for contactless energy transfer. xviii

3 The interoperability scenario of an industrial machine. . . xix

1.1 Circuit equivalent representation of an IPT device. 3

1.2 Compensation topologies. 6

1.3 Power dissipated on the load and IPT device efficiency. . . 10

1.4 Alternative electrical equivalent representation used to model a CET unit. 12

1.5 Efficiency versus magnetising inductance. 14

1.6 Voltage magnitude across capacitor C1. 15

1.7 Comparison between core and winding loss ratios. 20

1.8 Overview of a CET system. 20

1.9 3D representations of a linear transformer and a sliding transformer. 24

1.10 Representation and prototype of a pot core. 25

2.1 Conceptual diagram of a ZVS-PS inverter. 30

2.2 Approximated timing waveforms of a ZVS-PS inverter. . . 32

2.3 Simplified schematic of a CF-PR-PP inverter. 35

2.4 Simplified timing waveforms of a CF-PR-PP inverter. . . . 35
2.5 Realistic schematic of CF-PR-PP inverter. 37
2.6 Timing waveforms of a CF-PR-PP inverter. 37
2.7 Hybrid series-parallel LCL resonant inverter. 38

3.1 Example of a concurrent wireless power and data transfer in a closed-loop system. 42
3.2 Overview of a passive RFID system. 44
3.3 Simplified data exchange between RFID reader and tag. . 45
3.4 Model of a chipless RFID sensing system. 48
3.5 Maximum sensitivity mismatch explanation. 51
3.6 Block diagram of the direct passive sensing system. 51

4.1 Layout of a tea bag packaging machine. 57
4.2 Concept design of a wirelessly powered mover. 57
4.3 Circuit representation of the experimental CET system. . 58
4.4 Thermal model of the pot-core half. 61
4.5 Test bench of the CET system. 65
4.6 SPICE simulation of the ac/ac quasi-resonant converter. . 68
4.7 FEM simulation of the pot-core transformer. 69
4.8 Input impedance magnitude and phase of the CET link. . 70
4.9 Primary and secondary winding voltage and primary current. 71
4.10 Computed FFT spectra of primary currents for the two setups. 72
4.11 Example of planar coils for a sliding system. 75
4.12 Geometrical definitions of the planar coils used for numerical optimisation. 76

4.13 Coupling factor between moving and fixed coils connected in series. 76
4.14 Measured and predicted coupling factor between the moving and the series-connected fixed coils. 76
4.15 Photograph of the setup used for experimental validation. 77
4.16 Circuit representation of the sliding link. 78
4.17 Predicted output voltage and power transfer efficiency of the link. 79

5.1 Cut view of a rotating implementation of a WPIT device. 83
5.2 WPIT equivalent diagram and CPT link. 84
5.3 Electric diagram of the DP-RFID link. 85
5.4 Picture of the prototype. 86
5.5 Geometrical definitions of the prototyped DP-RFID link. . 87
5.6 S_{21} of the resonant capacitive link. 88
5.7 Peak detector input power and output voltage. 89
5.8 Drawing of a split-ring resonator with ground plane. . . . 92
5.9 Model representation of a SRR with ground plane as in [16]. 92
5.10 Final stack up of the SRR link 93
5.11 Geometric definitions of the manufactured SRRs. 94
5.12 Picture of the first SRR prototype. 95
5.13 Comparison of the port reflectivity of a single SRR. 96
5.14 Picture of the two stacked SRR prototypes. 97
5.15 Comparison of the reflection coefficient at the port 1 of two faced SRRs. 98
5.16 Comparison of the transmission coefficient of two faced SRRs. 98
5.17 Measured transmission coefficients of two faced SRR . . . 99

5.18 Relationship between the time required for temperature conversion and the rotation of the remote split ring. . . . 100
5.19 Circuit-equivalent schematic of the entire wireless UHF passive sensing system. 101
5.20 Effects of optimisation on the DP-RFID link. 103
5.21 Measured and predicted power levels on the RTD load. . . 105
5.22 Sensed temperature and power detector output voltage. . 105
5.23 End-to-end link efficiency measured on the RTD load. . . 106

List of Tables

1.1 Overview on WPT technologies, as in [1]. 2

1.2 Conversion expressions between alternative CET and IPT representations. 12

1.3 CET systems comparison. 23

4.1 Configuration of setups. 64

4.2 Electrical parameters of the transformers. 70

4.3 Losses and efficiency comparison. 72

4.4 Core temperature increase. 73

5.1 DP-RFID component values. 86

5.2 Geometrical dimensions of the DP-RFID link. 87

5.3 SRR geometric dimensions. 95

5.4 System component values 102

Abbreviations

ASIC	Application-Specific Integrated Circuit
CET	Contactless Energy Transfer
CF-PR-PP	Current-Fed Parallel-Resonant Push-Pull
CPT	Capacitive Power Transfer
CW	Continuous Wave
DP-RFID	Direct Passive Radio Frequency IDentification
EM	Electro-Magnetic
EMC	Electro-Magnetic Compatibility
EMI	Electro-Magnetic Interference
EV	Electric Vehicle
FFT	Fast Fourier Transform
HMI	Human Machine Interface
IC	Integrated Circuit
ICET	Inductive Contactless Energy Transfer
IGBT	Insulated Gate Bipolar Transistor
IPT	Inductive Power Transfer
LCIPT	Loosely Coupled Inductive Power Transfer
MCU	MicroController Unit
MOSFET	Metal-Oxide-Semiconductor Field-Effect Transistor
MPTP	Maximum Power Transfer Principle
MSM	Maximum Sensitivity Mismatch

PEEK	PolyEther Ether Ketone
PF	Power Factor
PP	Parallel-Parallel
PS	Parallel-Series
PTS	Positive Temperature Sensor
RCS	Radar Cross Section
RF	Radio Frequency
RFID	Radio Frequency IDentification
RTD	Resistive Temperature Detector
SP	Series-Parallel
SRR	Split-Ring Resonator
SS	Series-Series
UHF	Ultra High Frequency
VNA	Vector Network Analyzer
WIPT	Wireless Inductive Power Transfer
WPIT	Wireless Power and Information Transfer
WPT	Wireless Power Transfer
WSN	Wireless Sensor Network
ZCS	Zero-Current Switching
ZVS	Zero-Voltage Switching
ZVS-PS	Zero-Voltage Switching Phase-Shift

Introduction

"The Transmission of Electrical Energy Without Wires"

So the unprecedented Serbian-American inventor Nikola Tesla titles his article appeared on *Electrical World and Engineer*, back in March 1904. The first idea of transferring electricity, which belonged to Tesla in terms of remote powering electrical loads, was subsequently put into practice. In late experiments, dating 1921, he effectively showed the possibility to enlighten bulbs from distance, without wires. Evidence of this experiment is presented in Fig. 1. His following articles, letters, and patents remained almost unexplored for several years. In the meantime, scientific research on wireless techniques was devoted to *radio signals*, which represented an unforgettable leap in the knowledge of the mankind. Academic interest in wireless powering picked up much later, at the beginning of the 90s [2, 3]. Since then, and during the following years, wireless power transfer (WPT) has become a major trend of the on-going research in electrical, electronics, and telecommunications sciences. Nowadays, the WPT scientific community is aware that potential applications cover a wide range of fields, including automotive, energy generation, energy harvesting, bio-medical and industrial [4, 5, 6, 7, 8, 9]. The motivations that bear such a broad set of applications are also many and various. In the automotive industry, for example, electric vehicles

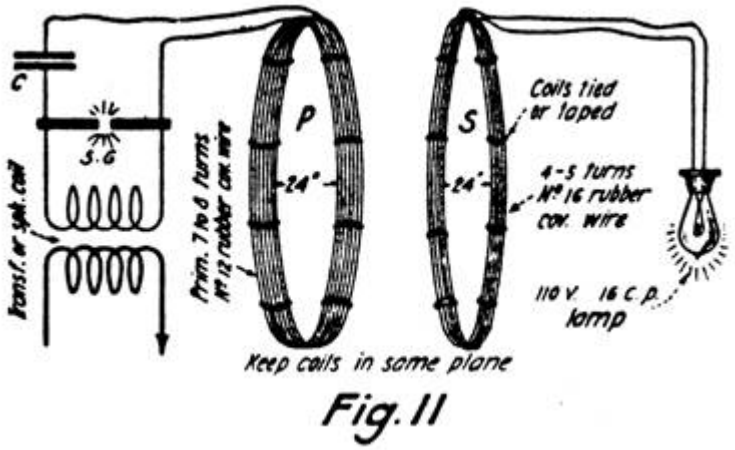

Figure 1: Nikola Tesla's sketch of his experiment on the transmission of energy without wires.

have a key impact in the next future. Moreover, in many industrial plants the need for contactless delivery of energy to moving loads is currently almost mandatory since it allows to overcome limitations in terms of performance, reliability and machinery maintenance due to the presence of sliding contacts or movable power cords. Solutions designed to replace such hardwired joints with contactless energy transfer links are widely envisaged in literature and stimulated the interest of many industrial activities, as well as numerous research and academic institutions [2, 10, 11].

Fortunately, most advances in WPT research can be shared among research groups that work on different topics, thus maximising the payback of their efforts. Some features, however, require special attentions, and demand for dedicated optimisation procedures. Let us consider again the case of industrial applications. Safety, reliability, and electro-magnetic compatibility (EMC) concerns on manufactured assemblies, for instance, dominate over efficiency and miniaturisation issues. Nevertheless, on large-scale production, the feasibility and, more important, the cost of assembled products have a foremost impact. In particular, power ap-

plications must seriously take into account absolute maximum ratings of components, such as voltages, currents, and operating temperatures. Furthermore, large safety margins should be considered during the development of a brand-new design. Obviously, these considerations also apply to WPT systems. One of the most common technologies employed in WPT is the inductive power transfer (IPT), which relies on the mutual inductance between coils to deliver electrical power without any physical connection. IPT technology well suits a wide range of applications, which rate from a few milliwatts to several of kilowatts [12, 13, 14]. For high power systems, the considerations explained above introduce significant differences in the design of a high-power IPT unit. These include ferromagnetic cores, simplified compensation schemes, lower operating frequencies, and stranded wires, just to cite some examples [15, 16]. As a result, some properties of the IPT device, such as efficiency, geometries, and versatility, are affected. For all these reasons, and in order to account for the different design approaches adopted in power systems, these ones are sometimes named differently, and referred to as contactless energy transfer (CET) systems [16, 17, 18, 19, 1, 20, 21, 22]. Cited works emphasise the key aspects of the CET system design, including evaluation of magnetic losses, predicted temperatures, and analysis of the external power supply. In fact, a CET application design includes wider aspects than the sole WPT unit modelling. In particular, the power converter behaviour is strongly related to the electrical description of its load (the WPT device, in this case), and the choice of the optimal topology is not a simple task [23]. For that reason, the power supply design must be considered as a constituent element of the entire CET system.

The trend toward wireless solutions in the industry is not limited to the contactless transfer of electrical power. Industrial machines repres-

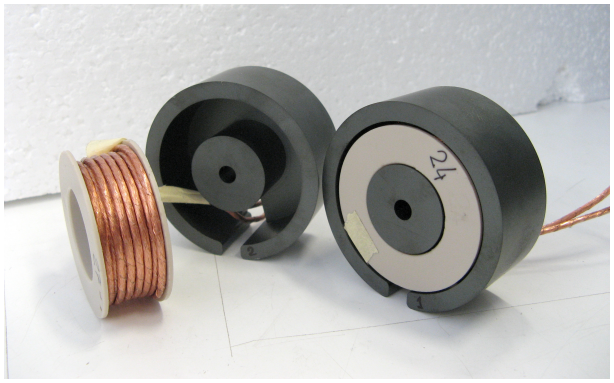

Figure 2: Example of a disassembled pot core for contactless energy transfer.

ent an excellent example of the automated interoperation of *mechanics*, *electricity*, and *information technologies*. The linkage between them is realised by means of hybrid entities, as shown in Fig 3. A *human machine interface* (HMI) allows operators to easily define the software variables that control the mechanical operation of the machine. Concurrently, electrical power is usually supplied to *actuators*, such as servomotors, heaters, or other tools, in order to convert electrical energy into mechanical energy. At the same time, information is collected from *sensors* and bytes of data are exchanged between the software controlling units and the *electronic drives*. Many on-board devices, including sensors and actuators, are enclosed within moving mechanical assemblies as rollers, arms, or sliding loads. In such cases, energy and data are traditionally delivered through sliding electric contacts, which notoriously suffer from early degradation, low reliability, and require frequent maintenance. With the increase of parallel data signals to be delivered (e.g. digital buses, multiple real time values, etc.), the limits of electric contacts turn out to be even more significant. Furthermore, the evolution of pervasive sensors technology has recently become attractive in industrial plants where monitoring of several parameters is needed in harsh environments; such has the inner parts of automatic machineries. Tra-

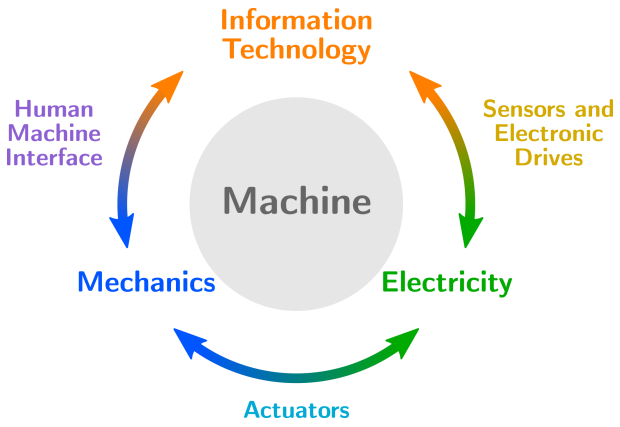

Figure 3: The interoperability scenario of an industrial machine.

ditionally, sensing elements are connected by means of cables or sliding contacts to the main controller. Once more, wired connection of machine sensors represents a limitation to the electric design flexibility and is responsible for a reduced wiring reliability.

In the pervasive interconnection scenario, the RFID technology has been proposed as a key enabling technology to identify, energize, and measure processed objects or materials [24]. Dedicated RFID sensing platforms have also been developed [25]. They are generally based on computational boards that embed a sensing unit powered by the RFID harvested energy. Usually, the sensor read-out is encoded by the microcontroller and sent to the RFID reader by back-scattering modulation. Nearly all possible sensor types can be employed. However, such approach requires a high level of active electronic integration on the sensing platform. Passive RFID-based sensing is also subject of recent research activities [26]. In this case, the RFID tag itself is exploited as a sensor by monitoring the antenna impedance variations with respect to the corresponding environment quantity to be monitored (e.g. temperature or humidity). This approach has similarities with surface acoustic wave (SAW) sensors, which are also considered RFID-enabled devices [27].

A drawback of such systems is that the sensor accuracy is frequently degraded by the radio channel.

Indeed, for industrial machinery applications, contactless sensor communication, combined with wireless inductive power transfer (WIPT), is seen as a great opportunity to optimise the productivity of the machine and reduce its maintenance. This is for example the case of power supplying rotary machineries with parameters of the remote branches to be monitored [22]. RFID technology is a good candidate for solving this problem. One proposed solution consists of exploiting a contactless capacitive channel to achieve information transfer or to realize an additional wireless power link besides the WIPT channel [28, 29].

The thesis is structured as follows: in Chapter 1 the theoretical background on IPT, its compensation, and maximum efficiency conditions are presented; in Chapter 2 different power supply solutions for WPT systems are discussed; in Chapter 3 an overview on both the RFID chipless passive sensing and the direct passive sensing techniques is given; in Chapters 4 and 5 several experiments involving IPT, CPT, and near-field UHF are presented and the results shown; finally, in the conclusive chapter some remarks are drawn.

Chapter 1

Inductive Power Transfer

Contactless energy transfer (CET) systems are gaining increasing interest for industrial applications, even when high powers are involved. Various techniques are suitable for WPT, depending on the medium used and the required power [1]. In Table 1.1 a short survey on WPT technologies is reported. Acoustic waves exploit mechanical pressure to transfer energy, generally for sensing purposes. Although they have the advantage that can be used where EM fields are not allowed, the power and distance ranges are relatively small. Light is often used to transport data, or signals, rather than power. In space applications can also be used to deliver electrical energy, but practical applications are very limited. Capacitive CET systems are gaining popularity. They exploit the electric field between capacitive plates placed at a certain distance with an air gap in between. Although they present good transfer efficiency and ensure a certain degree of movement of the power receiver, the main limitation is given by the maximum channel length: very short compared to other solutions. Finally, inductive CET, which can be employed for wireless delivery of huge amounts of energy, up to 100 kW and beyond. It is the only affordable solution for such power levels. Considerable

Table 1.1: Overview on WPT technologies, as in [1].

Technology	Frequency	Power range	Distance range	Applications
Acoustic	[20, 100] kHz	100 W	300 mm	Sensing, biomedical
Light	$\sim$ THz	100 W	1 km	Biomedical, space, telecom
Capacitive	[0.1, 100] MHz	50 W	1 mm	Sensing, phones
Inductive	[10 kHz, 10 MHz]	200 kW	2 m	Batteries, actuators

distances can also be covered and a wide frequency range is supported. Electro-magnetic interference may become an issue, although effective shielding techniques that are already employed in different application areas can be easily adapted.

The description of WPT techniques briefly proposed clearly provides the guidelines for choosing the right technologies for industrial applications: acoustic and capacitive solutions can be adopted for sensing purposes, whereas inductive CET ensures the proper combination of power and design flexibility. For this reason, much emphasis is given to IPT throughout the thesis. In particular, in this Chapter, the IPT circuit equivalent networks considered in the literature are introduced and the main operating principles discussed. Possible circuital resonant solutions are also discussed together with the required compensating networks. Then the problem of transferring, at the maximum efficiency, high power levels (of the order of 1 kW or higher) is considered, showing that highly coupled inductive links are needed, requiring to refrain from the resonance condition. These systems are usually referred to as CET systems, since the link distances are negligible with respect to the

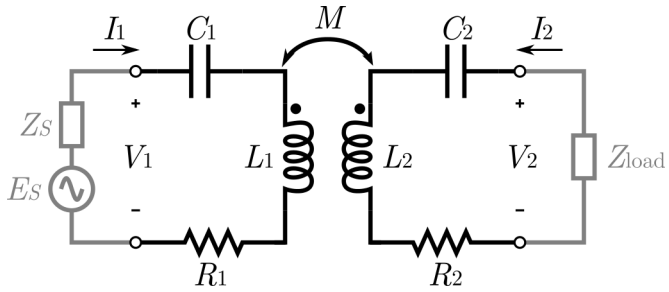

Figure 1.1: Circuit equivalent representation of an IPT device.

coils dimensions. The operating frequencies are of the order of tens to hundreds of kilohertz. The fundamental figures of merit are analytically defined and used to measure the actual limitations involved in this class of systems, including aspects related to realisation feasibility with respect to voltages and currents limitations. Finally, state-of-the-art CET works are surveyed, and realistic applications for different operating frequencies are considered and critically compared.

1.1 Inductive Coupling

The IPT technology for WPT exploits the variation of the magnetic field flux shared among two or more physically decoupled coils to transfer electric power to one, two, or more loads [13]. Electric transformers are based on inductive coupling too, although are usually designed to transform the voltage, or ensure galvanic separation between circuits, instead of establishing a wireless link for energy transfer. The widely used equivalent representation of an IPT device is based on coupled inductors, and usually also includes compensating (or resonant) capacitances and winding resistances, as show in Fig. 1.1.

IPT systems are sometimes referred to as loosely coupled inductive power transfer (LCIPT) systems, in order to emphasize the fact that the

coupling k

$$k = \frac{M}{\sqrt{L_1 \cdot L_2}},$$

between windings is way far from optimal [30]. As we will show shortly, in these cases the IPT system requires two compensating capacitances (C_1, C_2 in Fig. 1.1) designed to resonate with the coil inductances L_1, L_2. The resonant radian frequency ω_0 defines the series compensating capacitances as follows:

$$C_1 = \frac{1}{\omega_0^2 L_1}, \quad C_2 = \frac{1}{\omega_0^2 L_2}.$$

At resonance, resistances R_1, R_2 define the quality factors of the *unloaded* coils as follows [12]:

$$Q_{1,\text{unloaded}} = \frac{\omega_0 L_1}{R_1}, \quad Q_{2,\text{unloaded}} = \frac{\omega_0 L_2}{R_2}. \tag{1.1}$$

These quantities are useful to estimate the native losses and efficiencies of single coils, although differ from the common expression of Q-factors of loaded coils:

$$Q_{1,\text{loaded}} = \frac{\omega L_1 \left(R_1 + R_{\text{load}}\right)}{\omega M^2}, \quad Q_{2,\text{loaded}} = \frac{\omega L_2}{R_2 + R_{\text{load}}}, \tag{1.2}$$

which are employed to optimise the behaviour of the systems in terms of global efficiency, and power transfer capability of IPT systems [31, 11, 32, 33].

Primary and secondary impedances are defined as follows:

$$\begin{aligned} Z_1 &= R_1 + jX_1 = R_1 + j\left(\omega L_1 - \frac{1}{\omega C_1}\right) \\ Z_2 &= R_2 + jX_2 = R_2 + j\left(\omega L_2 - \frac{1}{\omega C_2}\right). \end{aligned} \tag{1.3}$$

From the inductors' constitutive equations

$$\begin{aligned} V_1 &= Z_1 I_1 + j\omega M I_2 \\ V_2 &= Z_2 I_2 + j\omega M I_1 \end{aligned} \tag{1.4}$$

we can infer the reflected impedance from the secondary to the primary by dividing the secondary voltage by the primary current resulting in:

$$Z_r = \frac{\omega^2 M^2}{Z_2 + R_{\text{load}}} .$$

Hence, the power transferred from the primary to the secondary is given by

$$P_{1\to 2} = \text{Re}\left[Z_r\right] I_1^2 ,$$

showing that, at resonance, the only limits to the system power transfer capability are set by the mutual behaviour of the coupled inductors, the load value, and the rating of the power source.

1.2 Compensation

The main goals in the design of an IPT device are its *efficiency* and its *power transfer capability* [34]. As described in next sections, in order to reduce losses in the system and maximise the transferred power, the inductance of the coils needs to be compensated [35]. An optimal compensation can be obtained by adding series or parallel capacitances that resonate with the coil inductances. Depending on the characteristics of the selected IPT devices and the constraints on load and source impedances, the optimal configuration of the compensating network (C_1, C_2 in Fig. 1.1) may vary. In Fig. 1.2, four possible compensation arrangements are shown. Primary and secondary compensating capacitors (C_1,

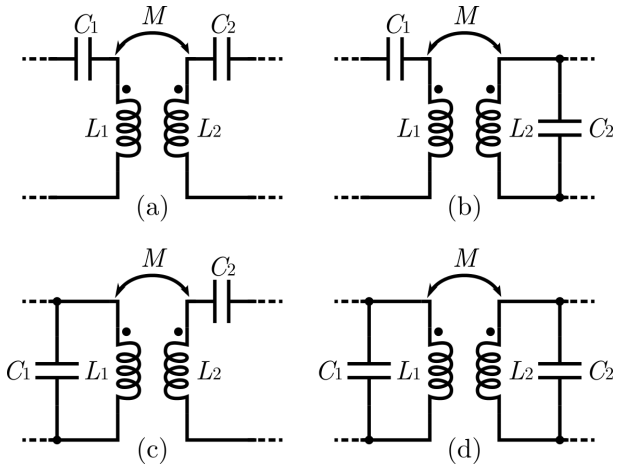

Figure 1.2: Compensation topologies: (a) SS; (b) SP; (c) PS; (d) PP.

C_2) are placed either in series (S) or in parallel (P) with the respective self-inductance (L_1, L_2).

Literature provides several guidelines for choosing the best compensating topology, according to the system constraints, in order to maximise the IPT device efficiency or its power transfer capability, providing reliable values for the electrical quantities. As general rules, we can summarise the following considerations:

- If the load is variable, the system requires series primary compensation, since C_1 in SS or SP does not depend on R_{load} [36].

- If the magnetic coupling is variable, the system also requires series secondary compensation, since C_1 and C_2 in SS do not depend on M [16].

- If load and coupling are fixed, the best secondary compensating topology can be chosen according to load value and secondary inductance [30, 37].

- If the parasitic parallel capacitance of the windings is not negligible, the system requires parallel compensation, since the parallel

resonator can also account for the parasitic capacitance of the coil [38].

- If the real part of the equivalent impedance at the input port of the IPT device is dominated by coil resistances (e.g. dominating winding losses), the system requires parallel compensation, since a parallel capacitance can affect the real part of the equivalent impedance [39, 40].

Although even more complex compensation networks have been studied, such as adaptive matching [11, 41] and additional self-resonant coils [35, 42], the SS compensation still represents a widely adopted solution, mainly because of its insensitivity to other parameters such as load and mutual inductance variations [1]. For this reason, only SS will be considered in the following.

1.3 Efficiency

According to the previous paragraph, the expression of the efficiency of an IPT device is not unique, but depends on the adopted compensating network configuration. As said, SS compensation, although sub-optimal for certain cases, represents a robust topology, since capacitances only depend on the windings self-inductances L_1, L_2. Thus, let us consider the IPT device of Fig. 1.1. Its power efficiency η can be expressed as follows:

$$\eta = \frac{P_{\text{load}}}{P_1} = -\frac{\text{Re}\left[\mathbf{V}_2\mathbf{I}_2^*\right]}{\text{Re}\left[\mathbf{V}_1\mathbf{I}_1^*\right]} = \frac{R_{\text{load}}}{R_1\frac{(X_2+X_{\text{load}})^2+(R_2+R_{\text{load}})^2}{\omega^2M^2}+(R_2+R_{\text{load}})}, \tag{1.5}$$

where $X_2 = \omega L_2 - 1/(\omega C_2)$ and $Z_{\text{load}} = R_{\text{load}} + jX_{\text{load}}$. Eq. 1.5 shows that the relationship between efficiency and coupling (expressed by M)

as well as between efficiency and resistance of windings (L_1, L_2) is not straightforward. Nevertheless, we can infer that primary resonance (or compensation) does not affect the efficiency, whereas secondary resonance (or compensation) and strong coupling improve the efficiency by mitigating the negative effect of R_1.

1.4 Power Transfer Capability

In a realistic case, the generator introduces a series impedance ($Z_S \neq 0\,\Omega$, in Figure 1), which accounts for additional losses. If the source impedance Z_S is given, we may be interested into knowing the maximum available power at the output port of the IPT device. In other words, the power transfer capability should be optimised.

As for the SS topology, the maximum output power on the load is expressed by:

$$P_{\text{load}} = \frac{1}{2}\text{Re}\left[\mathbf{V}_2\mathbf{I}_2^*\right] = \frac{R_{\text{load}}}{2}\frac{|E_s|^2}{\left|\frac{(Z_S+Z_1)(Z_2+Z_{\text{load}})}{\omega M} + \omega M\right|^2}\,. \tag{1.6}$$

In this case, primary and secondary compensations provide a direct advantage in terms of maximum available power at the output port. If we consider purely resistive load and source impedance (i.e. $X_{\text{load}} = X_S = 0\,\Omega$), and the coils are resonant (i.e. $\omega = \omega_0 = 1/\sqrt{L_1C_1} = 1/\sqrt{L_2C_2}$), Eq. 1.6 turns into:

$$P_{\text{load}} = \frac{R_{\text{load}}}{2}\frac{|E_s|^2}{\left|\frac{R_S R_{\text{load}}}{\omega_0 M} + \omega_0 M\right|^2} \tag{1.7}$$

and the power transfer capability is maximised. Further improvements can be achieved if the final load is a design parameter and is not given, by differentiating the second term of Eq. 1.7 with respect to R_{load},

as explained in [35].

1.5 Contactless Energy Transfer

The collection of possible IPT applications covers a wide range of power ratings, from a few milliwatts to several of kilowatts [12, 13, 14]. As the requirement on the transferred power increases, the system operating frequency is limited by the switching speed of the power converter [17]. Fig. 1.3 shows the variations of the output power and of the efficiency with respect to the winding inductances for three configurations of resonant coils at 50 kHz, 500 kHz, and 5 MHz, respectively. The Q-factor of each coil is held constant (equal to 10), as can be obtained by piecewise optimisation of coil and wire geometries, and the winding resistance of each ith-coil computed as

$$R_i = \frac{\omega L_i}{Q}\,, \quad i = 1, 2\,,$$

according to Eq. 1.1.

As expected, as the frequency decreases, the best efficiency is obtained at higher values of inductance. In these cases, air coils may not be sufficient to achieve the required inductance, and ferromagnetic cores become necessary to limit the dimension of the IPT unit and contain winding losses by increasing the Q-factor.

In the literature, the distinction between *inductive power transfer* and *contactless energy transfer* is vague. Some works (e.g. [43, 29]) refer to CET systems to aggregate different WPT technologies in the same device, such as inductive and capacitive power transfer or simply consider WPT systems based on non-inductive devices. However, the CET term should be adopted in place of the IPT one, to indicate systems

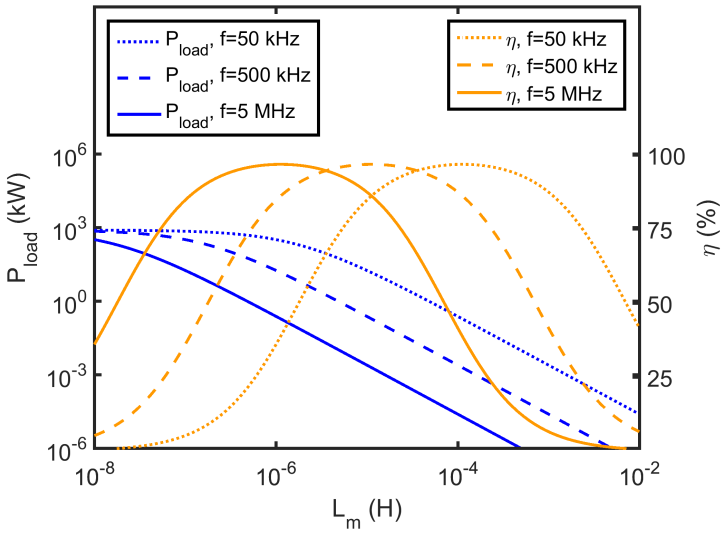

Figure 1.3: Power dissipated on the load and IPT device efficiency versus winding inductance ($E_S = 100$ V; $Z_S = 0$ Ω; Q_1, $Q_2 = 100$; C_1, C_2 resonant; $R_{\text{load}} = 50$ Ω; $k = 0.9$).

characterised by strong magnetic coupling (equal to or greater than 0.8, often including magnetic cores) and low operating frequency (from 10 to 500 kHz); this allows high WPT efficiency (usually greater than 70 %), and relatively high power ratings (e.g. more than a kilowatt) [17, 18, 44, 45]. In these cases, the necessity of a contactless transfer of electrical power usually comes from the need of supplying moving parts, such as rotating disks or sliding loads.

The strong coupling and the high Q-values of CET systems are mandatory at high powers not only for preserving the system efficiency but, more important, for ensuring protection from the EMI point of view. This can be obtained by combining two technological realisations:

1. Air gap between coils negligible with respect to their dimensions (e.g. less than a tenth of the coil radius).

2. Coils wound on ferromagnetic cores.

The combination of the two features into the same CET device results

into the design of an IPT unit that can be also considered as an *electrical transformer* [2]. Coils, however, can be differently shaped, in order to feature a proper magnetic circuit for the specific application. Although most systems adopt circular coils, rectangular windings are not uncommon [20, 46]. The latters have comparable performance, since at the CET operating frequencies, which lie in the kilohertz range, the conductor edges do not contribute significantly to the overall power losses. The coils shape also defines the geometry of the magnetic core: for circular coils, pot cores are generally employed, whereas for rectangular windings of sliding tracks the core shape can be more arbitrarily chosen. In these cases, E-shaped cores or rectangular blocks of ferromagnetic material can be used to enclose the magnetic flux.

1.5.1 Alternative Electrical Equivalent Representation

Because of the similarity between a CET unit and a transformer, the adopted equivalent electrical representation of the device is sometimes different from the diagram of Fig. 1.1, and the T-parameter representation visible in Fig. 1.4 is considered. The leakage inductances L_{lk1}, L_{lk2} and the magnetising inductance L_m are shown instead of the self-inductances L_1, L_2. In addition, the number of turns of coils N_1, N_2, and the resistance R_m, which accounts for losses in the magnetic core, are shown, whereas the other parameters remain unchanged.

A quick conversion between the CET representation and the IPT representation of a WPT unit is always possible by using equivalences summarised in Table 1.2, with the exception of the core resistance R_m. In some cases, indeed, as for resonance analysis, the IPT diagram is more convenient [47].

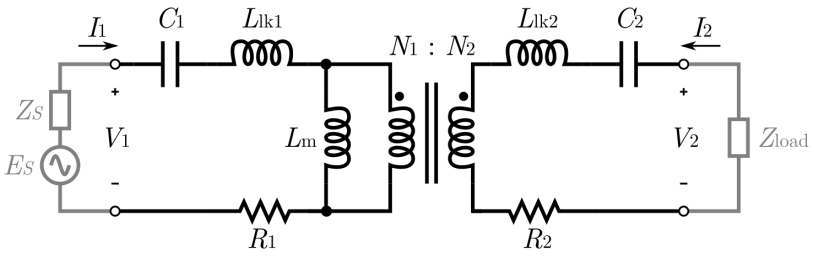

Figure 1.4: Alternative electrical equivalent representation used to model a CET unit.

Table 1.2: Conversion expressions between alternative CET and IPT representations.

IPT Parameter		Alternative CET
L_1	=	$L_{lk1} + L_m$
L_2	=	$L_{lk2} + \left(\frac{N_2}{N_1}\right)^2 L_m$
M	=	$\frac{N_2}{N_1} L_m$

1.5.2 Efficiency

Especially when the power rating of the system becomes considerable, the CET design should maximise the efficiency of the IPT unit, rather than its power transfer capability, in order to contain power losses that contribute to the system self-heating. In literature, analytical expressions of the power transfer capability of a CET unit are quite uncommon indeed, whereas efficiency expressions may assume different forms. Forms based on the Q-factors of the coils have the advantage to characterise the system by geometrical and material properties only, although do not implement the dependence on the core resistance R_m [48]. Conversely, forms based on the R- and L- parameters of Fig. 1.4 can include core losses as well [44, 49, 50]. By adopting the compensation topology of Fig. 1.4, the CET unit efficiency, as defined in Eq. 1.5, can be rewritten

as

$$\eta = \frac{R_{\text{load}} n^2}{\text{Re}\left[Z_{in}\right] \left| \frac{(Z_2 + R_{\text{load}}) n^2}{Z_m} + 1 \right|^2}, \tag{1.8}$$

where

$$n = \frac{N_1}{N_2}\,, \quad Z_i = j\omega L_{lki} + \frac{1}{j\omega C_{lki}} + R_i\,, \quad i = 1, 2\,,$$
$$Z_m = \frac{j\omega L_m R_m}{j\omega L_m + R_m}\,, \quad Z_{in} = Z_1 + \frac{n^2 \left(Z_2 + R_{\text{load}}\right) Z_m}{n^2 \left(Z_2 + R_{\text{load}}\right) + Z_m}\,.$$

At resonance frequency ω_0, Eq. 1.8 can be strongly simplified if we suppose $R_{\text{load}} \gg R_2$ and neglect core losses. In this particular case, the expression of efficiency turns into

$$\eta = \frac{1}{1 + \frac{R_1 R_{\text{load}} n^2}{\omega^2 L_m^2}}\,. \tag{1.9}$$

It can be easily verified that, by applying the third relationship of Table 1.2, Eq. 1.9 turns into a simplified form of Eq. 1.5 supposing, at resonance, $X_2 = X_{\text{load}} = 0$ and $R_{\text{load}} \gg R_2$. Although core losses should not be neglected in a CET unit, Eq. 1.9 confirms that strong coupling, combined with the appropriate compensating network, improves the efficiency, as expected.

1.5.3 Compensation

CET systems usually implement capacitive resonance. A high coupling coefficient, however, can partially alleviate the absence of compensation. For example, works presented in [15, 21] do not explicitly implement capacitive compensation, thus do not operate at resonance. Fig. 1.5 shows the plots of the efficiency versus the magnetising inductance for different coupling coefficients in resonant and non-resonant conditions. In these plots, the coils Q factor is held constant; hence, as the inductance in-

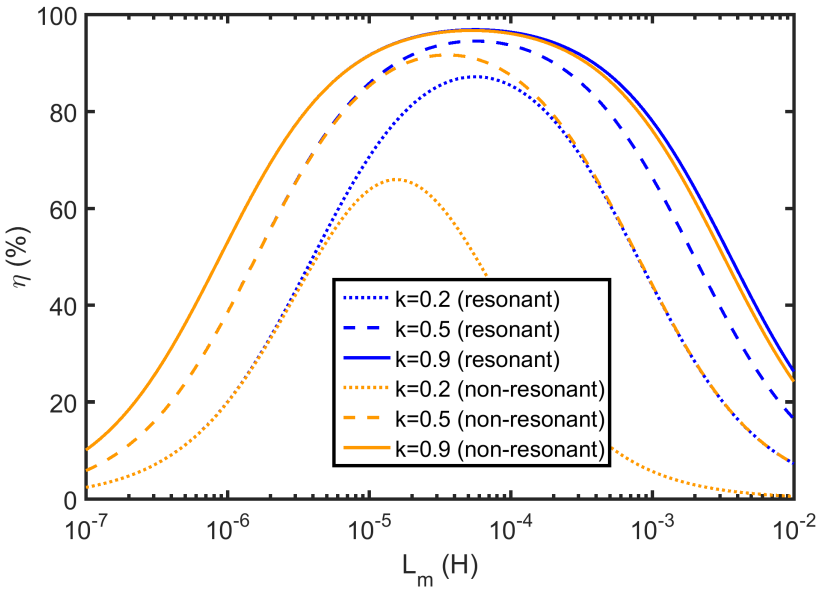

Figure 1.5: Efficiency versus magnetising inductance for different coupling coefficients in resonant and non-resonant conditions ($E_S = 100$ V; $Z_S = 0$ Ω; $N_1 = N_2$; Q_1, $Q_2 = 100$; $R_{\text{load}} = 50$ Ω; $f = 100$ kHz; $R_m \to \infty$).

creases, the coil resistance increases as well, and the system efficiency begins to decrease after a certain point with a non-symmetrical behaviour.

As can be noticed, as the mutual coupling increases, the difference in terms of efficiency between the resonant (compensated) and non-resonant (not compensated) cases becomes smaller. Therefore, a non-resonant design should be considered. In fact, for certain values of inductance and current ratings, the voltage levels across the corresponding resonant capacitor terminals may result prohibitive. To quantify this, we can compute the voltage magnitudes V_C across capacitor C_1, under resonance conditions and $N_1 = N_2$, as:

$$V_C = \frac{E_S}{k\left(\frac{R_1}{\omega L_m} + \frac{\omega L_m}{R_2 + R_{\text{load}}}\right)}.$$

The corresponding behaviour is plotted in Fig. 1.6, versus the magnet-

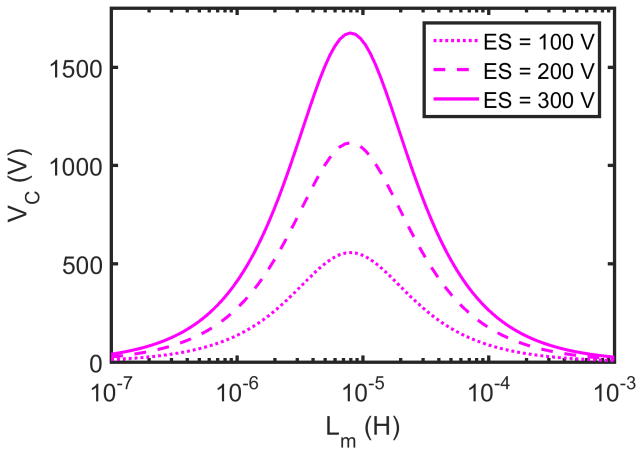

Figure 1.6: Voltage magnitude across capacitor C1 versus magnetising inductance for different source voltages ($Z_S = 0\ \Omega$; $N_1 = N_2$; $k = 0.9$; $R_{1,2} = 0.5\ \Omega$; $R_{\text{load}} = 50\ \Omega$; $f = 100$ kHz; $R_m \to \infty$).

ising inductance, for different source voltages (100, 200, and 300 V) and fixed windings resistance. Fixed resistances can be easily obtained by increasing the conductors effective section. In this case, a symmetrical behaviour is observed, since the Q factor varies with the inductance.

At 50 kHz, the resonant capacitance for a magnetising inductance equal to 20 µH is approximately 500 nF. Commercial capacitors of such values can difficultly rate more than a few hundred volts, whereas the computed voltage is well above 1500 V. For this reason, as far as the power factor of the CET unit is not a concern, is not unusual to design high-power IPT systems way far from their resonant frequencies.

1.5.4 Losses

Power losses in CET systems cannot be neglected. Although efficiencies of CET units are often above 90 %, a few tens of dissipated watts are enough to increase the device temperature to warning levels and put the whole system reliability in jeopardy. Three main factors are responsible for power losses in a CET unit: *skin effect* and *proximity effect* in

windings, and *eddy currents* in the core.

Winding Losses

The first parasitic element considered is the well-known *skin effect*, which results in an increase in the wire resistance when ac currents at high-frequencies circulate through them. The skin depth δ is defined as the depth below the surface of the conductor at which the current density J has fallen to $1/e$ of the current density at the surface J_S. In round conductors, it is well approximated as:

$$\delta = \sqrt{\frac{2\rho}{\omega\mu}}\,, \tag{1.10}$$

where ρ is the resistivity of the conductor, ω is the angular frequency of current, and μ is the absolute magnetic permeability of the conductor.

Wires stacked in layers, the ones above the others, also suffer from the *proximity effect*, that contributes to reduce the effective wire current cross-section due to the induced magnetic field from adjacent conductors [51]. Many works estimate the equivalent ac resistance of windings in magnetic components, when skin effect and proximity effect losses are considerable, such as [52, 53]. Generally, a strong reduction of these effects is obtained by adopting stranded wire, also called *litz wire*. Sullivan in [54] proposes a method to optimise the number of strands in a litz wire, by considering wire's thickness as well as core's geometries. Given the dc resistance of the winding, R_{dc}, its dc + ac resistance can be estimated as follows:

$$R_{\mathrm{ac+dc}} = R_{\mathrm{dc}} \left(1 + \frac{\pi^2\omega^2\mu_0^2 N^2 n^2 d_c^6 \gamma}{768\rho_c^2 b_c^2}\right)\,. \tag{1.11}$$

In Eq. 1.11 the current is supposed sinusoidal and ω is the radian fre-

quency, n the number of strands, N the number of turns, d_c the diameter of the copper in each strand, ρ_c the resistivity of the copper, b_c the breadth of the window area of the core, and γ a factor accounting for non-uniform field distribution in windings, usually equal to one.

Hence, electrical losses of windings, $P_{\text{loss},e}$, can be computed as follows:

$$P_{\text{loss},e} = \frac{1}{2} |I_1|^2 R_1 + \frac{1}{2} |I_2|^2 R_2 \,. \tag{1.12}$$

Core Losses

Core losses represent a considerable portion of the total losses of a CET unit. The choice of the material employed as ferromagnetic core is essential to prevent an excessive self-heating and ensure high efficiency. The frequency range of CET systems (usually 20–200 kHz) demands for high-resistivity ferromagnetic materials, in order to prevent the circulating of strong eddy currents within the core. Soft ferrites are commonly employed in the frequency range of interest because, despite the lower point of magnetic saturation compared to steel, their high resistivity significantly reduces those parasitic currents. Eddy currents and magnetic hysteresis, both proportional to the **B**-field (or magnetic flux density), are responsible for magnetic core losses $P_{\text{loss},m}$ within the core. An approximate computation of $P_{\text{loss},m}$, which includes eddy currents and magnetic hysteresis contributes, is possible thanks to the Steinmetz's equation [55]:

$$P_{\text{loss},m} = C_m C(T) f^x \hat{B}^y V_e \,, \tag{1.13}$$

where V_e is the effective volume of the core, $\hat{B}$ the peak flux density of a sine wave at frequency f, C_m, x, y material constants, and $C(T)$ a temperature correction factor. Such parameters can be derived from materials data sheets or retrieved from available surveys [56, 57]. The

peak flux density can be calculated by estimating the magnetising current i_m, or computing the current i_m iteratively, due to the dependence of R_m on $P_{\text{loss},m}$. The relation between B and i_m can be obtained from the Ampere's circuital law [58]. It states that the line integral of the **H** field equals the enclosed current:

$$\oint \mathbf{H} \cdot \mathrm{d}\ell = i_{\text{enc}} \,.$$

For a practical circuit as a pot-core transformer, the Ampere's law can be rewritten as

$$H l_e = N_1 i_m \,, \tag{1.14}$$

wherein l_e is the mean path length, or *effective length*, and Ni_m the number of primary turns times the magnetising current of the core. By applying the definition $B = \mu H$, (Eq. 1.14) results in:

$$\frac{B}{\mu} l_e = N_1 i_m \,.$$

Hence, the peak quantities are expressed as follows:

$$\hat{B} = \frac{\mu}{l_e} N_1 \hat{\imath}_m \,.$$

Since L_m is defined as

$$L_m = \frac{N_1^2}{\mathcal{R}_c} = N_1^2 \frac{\mu A_e}{l_e} \,,$$

wherein $\mathcal{R}_c$ is the core reluctance and A_e the *effective area* of the core, the **B**-field peak can be rewritten as:

$$\hat{B} = \frac{L_m}{N_1 A_e} \hat{\imath}_m \,.$$

If the voltage V_1 applied to the primary winding is known, an approximation of the **B**-field peak can be obtained by neglecting the leakage inductance L_{lk1} and supposing i_m sinusoidal. In this case, $\hat{i}_m = \hat{V}_1/(\omega L_m)$. This yields to

$$\hat{B} = \frac{\hat{V}_1}{\omega N_1 A_e}\,,$$

which is sufficiently accurate for preliminary estimations.

Computed $P_{\text{loss},m}$, the core resistance R_m can be approximated by neglecting the leakage inductance L_{lk1} as:

$$R_m = \frac{1}{2}\frac{|V_1|^2}{P_{\text{loss},m}}\,.$$

From Eqs. 1.12 and 1.13 we can straightforwardly evaluate the loss ratio as:

$$R_{loss,i} = \frac{P_{loss,i}}{P_{out}}\,, \quad i = m, e\,.$$

In Fig. 1.7 these quantities are plotted versus number of turns for a constant output power (900 W) at two different frequencies, 50 and 100 kHz. The ferrite core considered in the analysis is a ®Ferroxcube 3C81 P66 pot core [59].

From the picture it is evident how the computation of the optimal trade-off among several design parameters, such as number of turns, frequency, and core type, is not immediate ad may require to be evaluated iteratively.

1.6 CET Systems

Fig. 1.8 shows an overview of a CET system, represented by several building blocks.

In a CET system, the primary source of energy is usually the mains.

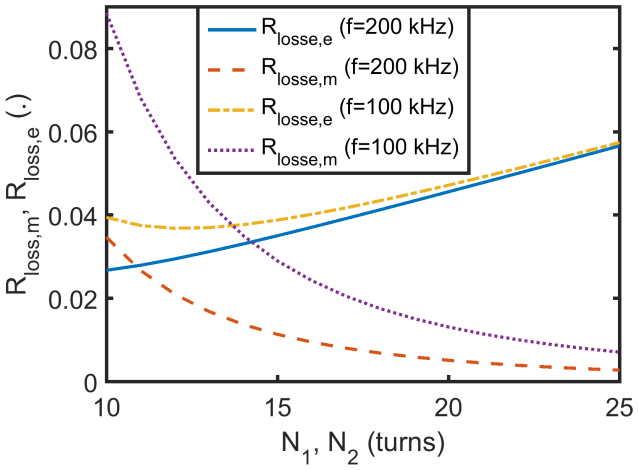

Figure 1.7: Comparison between core and winding loss ratios versus number of turns at different frequencies for a constant output power (V_2 = 300 V; C_1 , C_2 resonant; $R_{\text{load}} = 50\,\Omega$; $k = 0.9$; coil radius = 18.5 mm; coil resistance per unit of length = 9.7 mΩ/m; strands number = 50; strand diameter = 0.1 mm; core window breadth = 10.6 mm; core reluctance = 9.8 10^{-5} turns^2/H; ferrite = ®Ferroxcube 3C91; effective area = 717 mm^2; effective volume = 88200 mm^3).

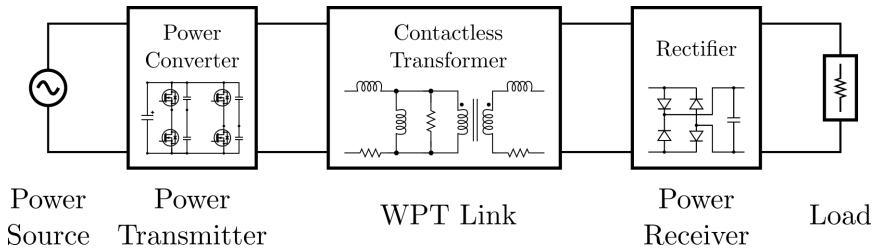

Figure 1.8: Overview of a CET system.

A switching-mode power supply is used to convert the mains frequency up to tens of kHz and acts as power transmitter for the WPT link. The inductive CET unit (i.e. a contactless transformer, in this case) constitutes the WPT link and the power receiver is often represented by an ac/dc power converter, or rectifying stage. Sometimes, the ac/dc conversion is unnecessary, and the final load is directly connected to the WPT link and represents the power receiver itself.

1.6.1 Power Transmitter

In order to contain the size of the magnetic core, thus preventing its saturation, the mains 50-(or 60-) Hz voltage should be switched at a higher frequency. The direct generation of a pure sine wave is almost impossible at power ratings of CET systems. In these cases, the widely employed solution is represented by switching mode power supplies (SMPS). The state-of-the-art SMPS adopt soft-switching techniques in order to alleviate turn-on and turn-off losses of the switching network, theoretically extending the devices lifetime and avoiding possible electromagnetic interference (EMI) [60, 61]. Soft-switching techniques rely on inductive loads to achieve zero-voltage or zero-current commutation of the switches [58, 62]. For high-power and high-frequency operation, zero-voltage switching (ZVS) converters are preferred over zero-current switching (ZCS) ones, because the parasitic elements of switching components facilitate the soft-switching mechanism [63]. An extensive description of power supply topologies suitable for WPT systems is provided in Chapter 2.

The presence of an inductive element (i.e. WPT link) suggests that the contactless transformer itself can be used to store the energy controlled by the converter. Authors of [23], for example, propose a phase-

shift ZVS full-bridge converter that exploits the inductive equivalent input impedance of the transformer and four parallel capacitances to achieve soft switching of active elements. Differently, the work presented in [19] introduces primary compensation and exploits this capacitance to realise a resonant tank that eases the resonant process of the converter.

Table 2 shows comparisons of some state-of-the-art CET systems considered in this review. The adopted power converter topologies are shown, as well as system ratings, geometry of magnetic circuits (discussed next), and specifications of power receivers.

1.6.2 WPT Link

The WPT link represents the core of the system. In previous paragraphs, we described the theory of operation of a CET unit. In the following, instead, we present two different implementations of the IPT device widely discussed in CET-related literature: the *sliding transformer* and the *rotary transformer*.

Linear Transformer

The description of a CET system based on a *linear transformer* is formally introduced in [44], though studied in numerous other works, such as [9, 65, 66]. A linear transformer, is composed by a *linear track* that constitutes a long magnetic primary circuit, or a long primary winding loop, and one or more secondary winding wound about a 'magnetic pickup' free to move on the linear track, as shown in Fig. 1.9(a).

As described in [46, 67], for example, the linear transformer can also be intended differently. Authors of cited works propose a *sliding transformer* in which the primary track is segmented into several primary coils wound about several core blocks, and some secondary pickups that

Table 1.3: CET systems comparison.

Converter Topology	f **(kHz)**	P_{load} **(W)**	**CET Geometry**	**Max** k	**Max** η **(%)**	**Output Rectifier**	**Ref.**
Resonant full-bridge	30	N/A	Linear track	0.8	N/A	4-diode bridge	[9]
Half-bridge	191	33	Planar array *	0.3	89	4-diode bridge	[64]
ZVS full-bridge	1000	1000	Rotary transf.	>0.9	N/A	2 diodes, central tap	[23]
Resonant half-bridge	30	20	Linear track *	0.2	†76	4-diode bridge	[65]
Resonant full-bridge	90	1000	Rotary transf.	0.8	82	2 diodes, central tap	[19]
ZCS full-bridge	60	3000	Rotary transf.	0.8	†93	4-diode bridge	[16]
Resonant full-bridge	165	1000	Sliding transf.	N/A	†95	4-diode bridge	[46]
ZVS/ZCS full-bridge	100	1600	Gapped transf.	0.8	†94	4-diode bridge	[21]
ZVS full-bridge	50	1000	Rotary transf.	0.9	98	None	[50]

* Not a proper CET system due to the weak coupling. † Includes power electronics efficiency.

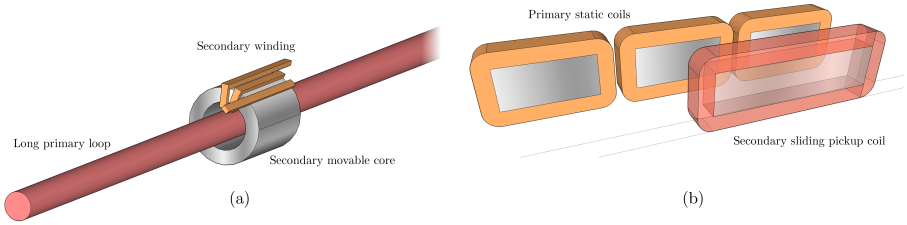

Figure 1.9: 3D representations of (a) a linear transformer as in [44]; and (b) a sliding transformer as in [46].

face primary coils along a secondary parallel track, as depicted in Fig. 1.9(b). This way, magnetic leakage and ohmic losses can be reduced, and the efficiency improved.

Finally, planar *array* geometry can be derived from the sliding transformer, as proposed in [68]. Similarly to a segmented primary linear track, several primary coils are distributed over a 2D surface, and a secondary pickup is free to move along two axes.

Typical applications of linear transformers are represented by electrical delivery systems for planar moving platforms. Some examples are drive belts, linearly moving motors, and power rails.

Rotary Transformer

A *rotary* (or *rotatable*) *transformer* design represents one of the first implementation of a CET system [2, 14]. Rotatable transformers are usually based on *pot-core ferrite cores*. A pot-core transformer is composed by two separate half cores, as shown in Figure 10.

In a standard application, a pot-core transformer encloses two windings wrapped about its central leg and a through-hole screw, or an external spring, tightens the half cores together. Conversely, pot cores for CET applications exploit the physical separation of the halves to allow the rotation of the one with respect to the other. Physical separation is obtained by ensuring an air gap between the halves.

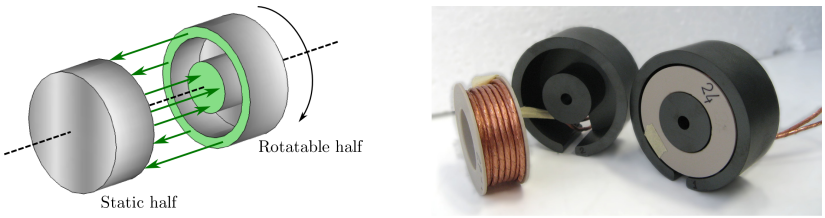

(a) (b)

Figure 1.10: (a) 3D representation of two half pot cores and their magnetic flux lines as in [50]; (b) prototyped version of a pot-core transformer with air gap as in [69].

In order to allow relative rotation, the windings must be detached as well. Two different winding topologies are possible, either *adjacent windings* or *coaxial windings* [15]. In the former topology each winding is placed in its own half core, whereas in the latter windings are concentric. Many works compare the two different topologies, e.g. [70]. Depending upon the final application, the one might be more favourable than the other. On the one hand, for example, the adjacent topology exploits the available room for windings in the window area of the core more efficiently, resulting in a lower magnetising current and, in turn, lower losses. On the other hand, coaxial windings share the whole magnetic flux path of the transformer, resulting in lower leakage inductances and therefore higher coupling coefficient.

Typical applications of rotatable transformers are meant to replace rotary electrical joints, also known as *slip rings*. Such joints have wide use in both industrial and military areas, for example in robot arms, rotary working tools (as drilling machines, or sealers), and radars. For instance in [50, 69], a CET system has been prototyped for power supplying rotatable parts of automatic machineries, namely sealing rollers. The system performance is also reported and compared in Table 1.3.

1.6.3 Power Receiver

The power receiver usually implements a rectifying stage. The ac/dc conversion is necessary when the system load operates in the dc regime, such as batteries, logics, or dc drives. In these cases, the rectifier is constituted by a 4-diode bridge or, alternatively, a 2-diode bridge if the CET unit provides for a central tap. Authors of [71] propose a 'reversible rectifier,' instead, to allow bidirectional energy flow. Differently, when the system load is resistive, (a heater or a sealer, for example, as in [50]), the ac/dc conversion may be unnecessary if the resulting parasitic load reactance is negligible at the operating frequency.

Chapter 2

Power Supplies for WPT

An excellent design of the IPT system becomes useless if the appropriate power source, as well designed as the CET unit, is not attached to its primary port. The main functionality of the CET power source is to convert the energy from mains into a suitable from for the inductively coupled system. The line frequency provided by power utilities (50 or 60 Hz) is too low in order to design compact IPT units characterised by weak magnetic coupling and would demand huge core geometries to prevent ferrite saturation [4, 13]. A frequency conversion is then required to ensure an acceptable efficiency. For this reason, ac/ac power converters are usually employed to increase the supplied voltage frequency and to regulate the amount of energy transferred by controlling the switching network. Thanks to the improvements in electronic switches, as MOSFETs or IGBTs, 10 to 500 kHz switching converters are not an issue, even for powers in the kW range.

The presence of an inductive element (i.e. the natural impedance of the IPT unit) suggests that the link itself can be used to store the energy controlled by the converter. Several topologies such as flyback, resonant, quasi-resonant, and self-resonant converters can be employed

in this case [23]. The usage of *soft-switching* techniques in power converters alleviates turn-on and turn-off losses of the switching network, theoretically extending the devices lifetime and avoiding possible electromagnetic interference (EMI) [61, 60]. The mentioned flyback converter is suitable to achieve a zero-current switching scheme. For high-power and high-frequency operation, however, practical issues due to parasitic components worsen controlling capabilities. On the contrary, zero-voltage switching is more appropriate for high-power and high-frequency converters, because parasitic elements generally improve its performance [63].

2.1 Voltage-current Behaviour of the IPT System

The constitutive equations 1.4 of the IPT circuit offer the starting point for an interesting consideration. Let us suppose to operate the system at resonance ($\omega = \omega_0$) and to neglect losses in coils, namely the terms R_1 and R_2 in Eq. 1.3. Hence, impedances Z_1 and Z_2 are nearly zero. If we are interested into the output (i.e. secondary) current I_2, we can manipulate the first of Eqs. 1.4 to obtain:

$$I_1 = \frac{V_1 - j\omega M I_2}{Z_1}\,,$$

and, by replacing I_1 in the second, we obtain:

$$-Z_1\, I_2\, (R_L + Z_2) = j\omega M\, (V_1 - j\omega M I_2) \quad \Rightarrow$$
$$I_2 \simeq \frac{V_1}{j\omega M}\,,$$

which clearly shows that the output current only depends on the input (i.e. primary) voltage V_1, the mutual inductance, and the frequency. Conversely, if we are interested into the output (i.e. secondary) voltage V_2, we can manipulate the second of Eqs. 1.4 to obtain:

$$V_2 \left(1 + \frac{Z_2}{R_L}\right) = j\omega M I_1 \quad \Rightarrow$$

$$V_2 \simeq j\omega M I_1 \,,$$

which clearly shows that the output current only depends on the input (i.e. primary) current I_1, the mutual inductance, and the frequency. After all, this is not surprisingly. If we recall the Magnetic Ohm's Law,

$$Ni = \mathscr{R}\phi \,,$$

where N is the number of turns of a coil, i the current which flows in the coil, $\mathscr{R}$ the reluctance of the magnetic path enclosed within the coil, and ϕ the magnet flux along the path, and the Lenz's Law,

$$e = N\frac{d\phi}{dt} \,,$$

where e is the induced voltage across the coil terminals, it is clear that a constant-amplitude alternate current at the primary side generate a constant-amplitude alternate magnetic field, thus flux, that, in turn, induces an electromotive force (i.e. a voltage) at the secondary regardless the load attached. Then, we can summarise the behaviour of the IPT system as follows:

Primary		**Secondary**
constant voltage	$\Rightarrow$	constant current
constant current	$\Rightarrow$	constant voltage

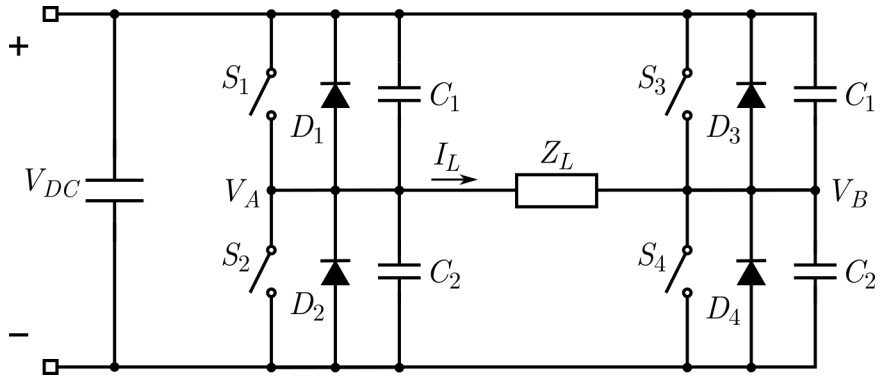

Figure 2.1: Conceptual diagram of a ZVS-PS inverter.

In the following, these two cases are considered.

2.2 A Voltage-fed IPT Converter: ZVS-PS Inverter

The wide availability of ac/ac converter topologies makes the combination of ac/dc line rectifiers and dc/ac bridge inverters a popular choice. Among the possible configurations, energy-efficient solutions, such as soft-switching schemes, are preferred. In *pseudo-resonant* (or *quasi-resonant*) topologies, the switches turn on and off at zero voltage, and the input voltage of a switch is clamped at the input dc voltage. Authors of [23], for example, employ a phase-shift full-bridge converter which exploits the inductive equivalent input impedance a contactless transformer and four parallel capacitances to achieve soft switching of active elements. Generally, half-bridge and full-bridge (also known as H-bridge) versions are both available for each resonant converter topology. Since for the same output power the switch currents for a full-bridge are one-half of those for a half-bridge—at a modest increased complexity, given the actual cost of electronics—only the 'H' configuration will be considered [58].

Zero-voltage switching (soft-switching, or quasi-resonant) phase-shift (ZVS-PS) converters and their circuital variants are well covered in literature [63, 72, 73, 74, 75]. A conceptual diagram of a ZVS-PS converter is shown in Fig. 2.1. Switches and diodes 1 to 4 represent ideal MOSFETs with the intrinsic junction diodes. The inverter load Z_L should be considered strongly inductive, in such a way that the output current can ease the soft switching as described in the following. The output voltage is controlled via phase control: the crossing pairs of the H-bridge, namely S_1, S_4 and S_3, S_2, operate at a fixed 50% duty cycle or less, and the phase difference between the half bridge pairs, namely S_1, S_2 and S_3, S_4, is controlled to obtain the ac output voltage regulation [62].

The switching process can be described by the following phases, as visually presented in Fig. 2.2:

1. S_2 and D_4 conduct. The output voltage is zero and the output current negative.

2. S_2 is switched off. The negative output current causes C_1 and C_2 to charge, and V_A to increase. At the same time, the negative output current starts decreasing in magnitude. During this phase, the output inductance and the two capacitances form a resonant network.

3. If the resonant network has sufficient energy stored in the output inductance, V_A reaches V_{DC}, by activating D_1 that clamps V_A to the dc voltage. I_L is still negative. S_4 can be turned on at zero-voltage at any time, as D_4 is forward biased.

4. At this point, S_1 can be switched on at zero voltage, as D_1 is already conducting. The output current becomes positive. If the resonant network did not have sufficient energy to activate D_1, non-

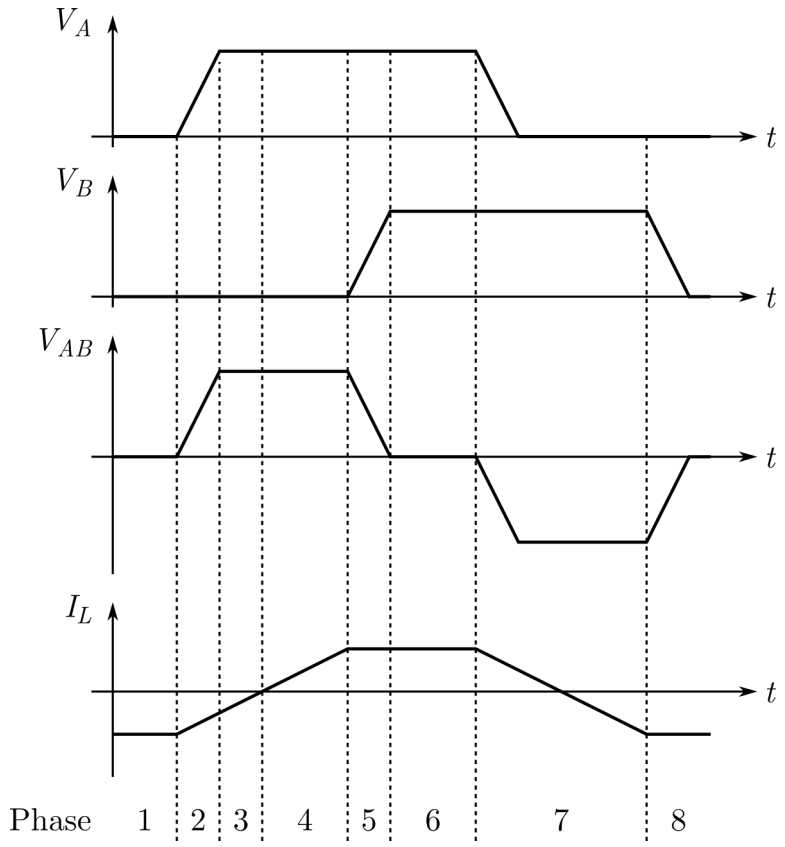

Figure 2.2: Approximated timing waveforms of a ZVS-PS inverter.

zero voltage commutation occurs in this phase, with a subsequent switching loss. S_4 must be already on, as D_4 would naturally switch off with a positive I_L.

5. I_L reaches its maximum and becomes flat. S_4 is switched off. At this point, I_L starts charging C_3 and C_4. V_B increases.

6. D_3 becomes forward biased and clamps V_B to V_{DC}. This time, the current required to charge C_3 and C_4 and to activate D_3 comes from the dc bus through S_1, which is still on, not from the energy stored in the load. S_3 can be turned on at zero-voltage at any time, as D_3 is activated.

7. S_1 is switched off. The positive output current starts decreasing in magnitude, as well as V_A. After discharging C_2, D_2 becomes forward biased and S_2 can be switched on before I_L inverts its sign and becomes negative again.

8. At this point, a symmetrical behaviour involving S_3 and D_4 is observed: the switch is turned off, V_B decreases, and the diode becomes forward biased, starting off from phase 1.

Transitions involving the *left* half bridge elements, namely S_1, D_1 and S_2, D_2, are also referred to as 'passive-to-active,' because turn-on transitions are initiated by the energy stored in the load. Conversely, transitions involving the *right* half bridge elements, namely S_3, D_3 and S_4, D_5, are also referred to as 'active-to-passive,' because turn-on transitions are initiated by the energy supplied by the source.

Thanks to the zero-voltage transitions, this converter exhibits low primary-side switching loss and generated EMI. Compared to an ideal 'hard-switched' topology, in which commutations do not trigger resonances, conduction losses are slightly increased because of the additional

currents that flow in the output inductor. This contribute, however, is much smaller than the power saving of the soft switching. Efficiencies well greater than 90 % are not uncommon. In [74], for example, an efficiency of 95 % at 112 kHz for 670 W is obtained, whereas in [75] 93 % at 120 kHz for 2 kW.

2.3 A Current-fed IPT Converter: CF-PR-PP Inverter

An alternate-current power source is the most common solution to energize primary loops of WPT systems [76, 77]. The main advantage is the constant output voltage at the secondary side, regardless the load value.

The simplest, though effective, current-fed inverter is described as class D current-source parallel-resonant inverter in [78, 79, 80], also called current-fed parallel-resonant push-pull (CF-PR-PP) inverter [81]. The diagram of a CF-PR-PP inverter is based on a constant dc current source commuted across a resonant load by a pair of electronic switches, usually MOSFETs, as shown in Fig. 2.3 [82]. If the switches are commuted at the resonance frequency given by $\omega_0 = 1/\sqrt{LC}$, its operation principle is pretty simple and can be visually described as in Fig. 2.4. The parallel LC resonator act as a rough bandpass filter: its impedance is ideally zero at the resonant frequency and different from zero elsewhere. This way, the load R_L is supplied with a single-tone sinusoidal current. Also, in this case, the switches turn on and off at zero voltage, resulting in no commutation losses.

A more realistic circuital diagram of a CF-PR-PP inverter is shown in Fig. 2.5. The ideal current generators are replaced with a dc voltage supply, whose current is split into two inductors L_1 and L_2 that act as RF chokes. The supply current is considered approximately constant,

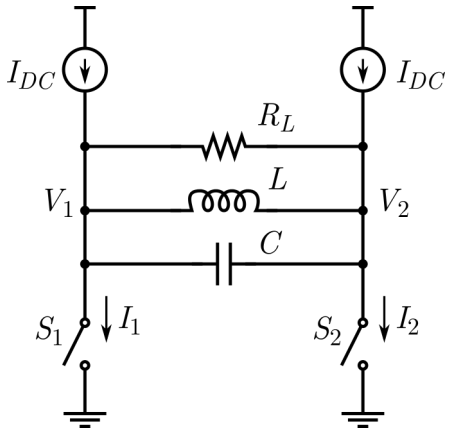

Figure 2.3: Simplified schematic of a CF-PR-PP inverter.

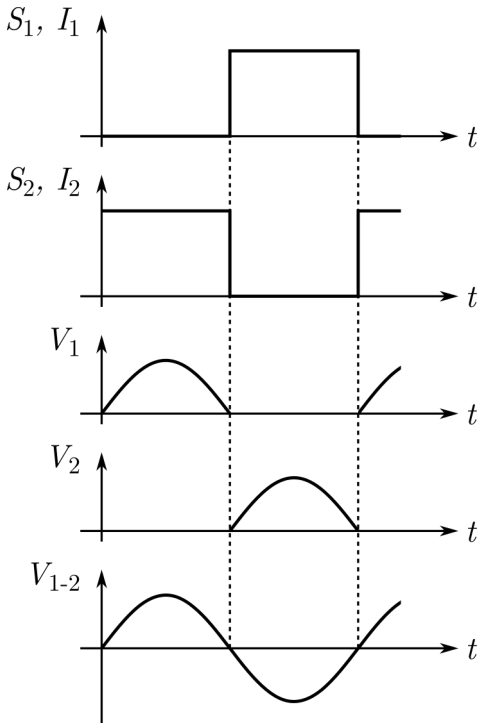

Figure 2.4: Simplified timing waveforms of a CF-PR-PP inverter.

provided that the series inductor L_{DC} is sufficiently large. When MOSFETs are employed, it is a good practise to include the series diodes D_1 and $D_{2.}$ In fact, at resonance, their presence is unnecessary in principle, since the voltages across the MOSFETs naturally become zero every semi-period. If the switching frequency f_s does not match the resonance frequency $f_0 = \omega_0/(2\pi)$, however, a tricky condition occurs. For example, if the switching frequency is lower than the resonance frequency ($f_s < f_0$) the load is inductive, and the MOSFET currents I_1, I_2 lag the load voltages V_1, V_2 (and the load current lags the load voltage), as shown in Fig. 2.6. If series diodes D_1 and $D_{2.}$ are not included, this results into temporary negative voltages on MOSFETs drains that activate the intrinsic junction diodes of Q_1 and Q_2, sourcing an undesired current from ground to load. In addition, despite the series diodes, turn-on transitions of MOSFETs are not zero-voltage, resulting into switching losses. The case $f_s > f_0$ is similar, although switching losses occur in both turn-on MOSFET transitions and reverse-recovery turn-off diode transitions, turning $f_s > f_0$ into an even worse design choice. To eliminate the risk of possible mismatch between the resonance and the switching frequencies, switches are often controlled in a closed loop with complementary pulses obtained by the differential output voltage comparison. In this case, a suitable start-up strategy or circuitry is required [83, 84].

Supposing a perfectly resonant operation of the inverter, power losses are represented exclusively by conduction losses. Namely, losses in the choke inductors, in the MOSFETs, in the series diodes, and in the resonant circuit. The cited literature reports different efficiencies depending on frequency and output power. In particular, in [81] authors reached 96 % of efficiency in converting 15 W at 255 kHz, whereas in [82] efficiency equals 78 % for almost 1 W at 700 MHz by exploiting non-conventional

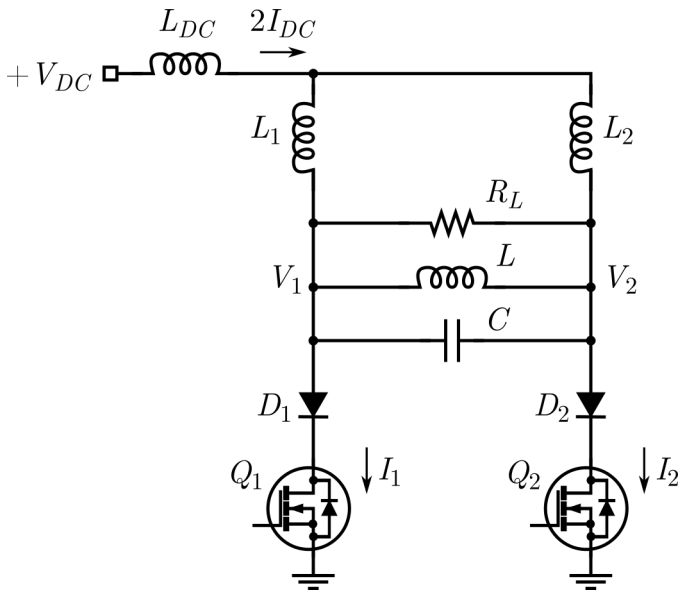

Figure 2.5: Realistic schematic of CF-PR-PP inverter.

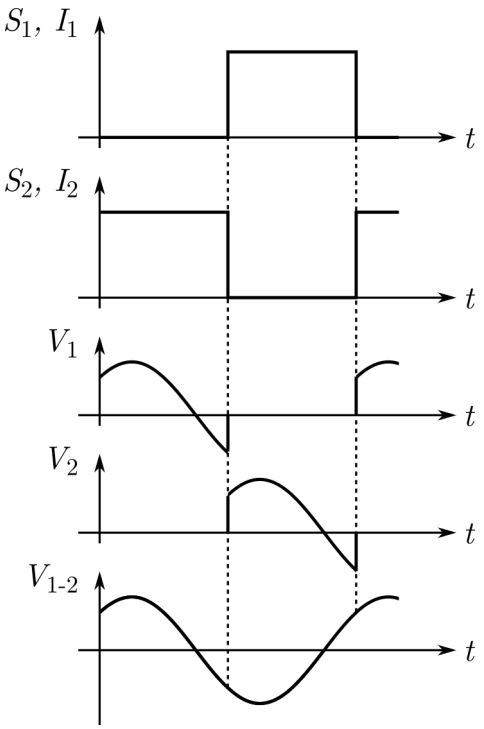

Figure 2.6: Timing waveforms of a CF-PR-PP inverter in case of $f_s < f_0$.

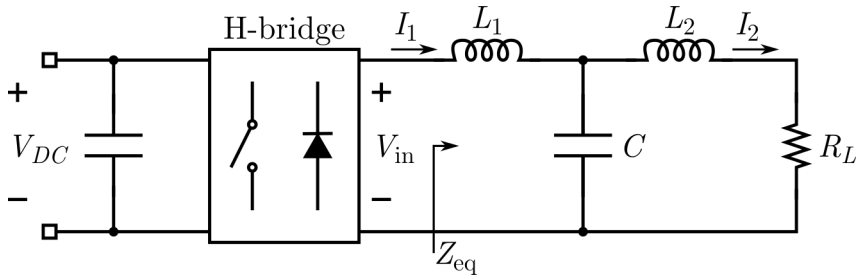

Figure 2.7: Hybrid series-parallel LCL resonant inverter.

GaAs heterojunction bipolar transistors.

2.4 A Hybrid IPT Converter: LCL Resonant Power Supply

Hybrid resonant power supplies are seen as an interesting alternative to current-fed IPT converters employed in constant-current WPT systems [85, 86]. Such solutions are based on the combination of a conventional resonant voltage-fed voltage supply (e.g. ZVS-PS inverter) with a series-parallel LCL resonant network, that acts as an *impedance inverter*, as shown in Fig. 2.7. The main advantage is that, thanks to the resonant LCL network, a constant voltage from the voltage inverter generates a constant current on the load, independently of its value [87, 88, 89].

The constant output current formulation is demonstrated in [87]. The equivalent load impedance Z_{eq} can be defined as

$$Z_{\text{eq}} = R_{\text{eq}} + jX_{\text{eq}}\,,$$

where

$$R_{\text{eq}} = \frac{R_L}{(\omega C R_L)^2 + (1-\omega^2 L_2 C)^2}$$
$$X_{\text{eq}} = \omega L_1 + \frac{\omega L_2 - \omega C\left(\omega^2 L_2^2 + R_L^2\right)}{(\omega C R_L)^2 + (1-\omega^2 L_2 C)^2}\,.$$

The inductors should be chosen such that $L_1 = L_2 = L$ to make it

resonant at a frequency $\omega_0 = 1/\sqrt{LC}$. In this case, at $\omega = \omega_0$, the LCL network realises an ideal impedance inverter, leading to $R_{\text{eq}} = (\omega L)^2 / R_L$ and $X_{\text{eq}} = 0$. Then, by analytical or circuital manipulation, it can be obtained that

$$I_2 = \frac{V_{\text{in}}}{j\omega L}\,.$$

In other words, the output current is independent of the load and controllable by the inverter output voltage level.

From the system perspective, an additional advantage is evident: the second inductance L_2 can be replaced by the uncompensated input of the IPT unit. In this case L_1 has to be chosen carefully to match the input inductance of the IPT unit.

Efficiency considerations for this class of inverters are similar to the ones of the ZVS topology. In addition, since the output network includes an additional inductor, at least, we expect a further degradation of the overall efficiency. The available literature reports that efficiencies greater than 90 % are difficult to reach. To make an example, in [87], an efficiency of 85 % is obtained at 100 kHz for 200 W.

Chapter 3

Wireless Sensing

Among all the possible WPT application areas, the increasing performances of industrial machines, in terms of reliability and low maintenance, make this field a potential market for wireless power applications. The upcoming industrial solutions demand for an innovative and robust technology to simultaneously supply energy and deliver data signals. Indeed, this is critical in monitoring remote subsystems located in isolated sites difficult to be reached. Some complex industrial equipments, as automatic machines, for example, demand for wirelessly powered actuators that are controlled through complex feedback loops. In these cases, remote sensors may be located in proximity of actuators, but require independent energy supply and communication links physically decoupled from the actuator power link due to robustness and safety requirements [90]. A simultaneous wireless transmission of power and data in an automatic machine environment can be represented as shown in Fig. 3.1. The upper part of the diagram shows the actuator supply: electric power is modulated by the switching dc/ac converter and wirelessly delivered to the actuator (e.g. a heater) by an inductive unit. The lower part of the diagram shows the feedback path of the sensor data: its readout is con-

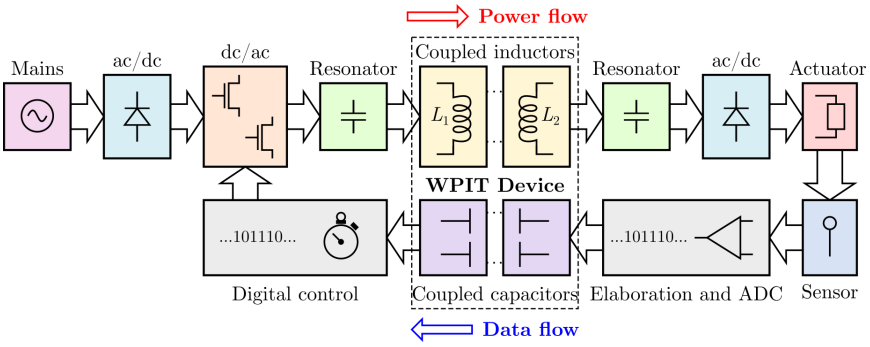

Figure 3.1: Example of a concurrent wireless power and data transfer in a closed-loop system.

ditioned, digitalized, elaborated and sent back to the controller through a secondary wireless interface. Many contactless industrial applications do not necessarily involve large air gaps between the energy source and the electric load (sensor, actuator, etc.). This allows to investigate the use of UHF signals in the near-field range for passive sensing purposes.

The passive sensing technology embrace a broad set of solutions, which differ for frequency bands, sensing elements, and control circuitry. Low frequency RFID charge mechanisms for backscattering digital sensing platforms were not uncommon research topics a few years ago and are still the subject of recent studies [91]. With the advances in RF and microwave technologies, the UHF band has become the preferred option for passive systems [92, 93]. Nevertheless, backscattering modulation is still adopted by many passive sensing solutions, thus requiring implementing sophisticated electronic hardware on remote boards (also known as chip-enabled RFID) [25]. Although this approach ensures a high flexibility in the choice of sensing elements and digital data elaboration, it cannot be considered the most genuine embodiment of the passive sensing technique.

Recent studies describe truly passive sensing systems, which do not include any active element on the remote board that hosts the sensor

[27]. In such cases, sensing elements are based on chipless RFID circuits that modify their reflection coefficient depending on the physical quantity to be measured (e.g. temperature, or humidity). This modification, resulting in a different reflected power or a shift in the resonance frequency, is then detected by the transmitter and can be digitally related to the physical quantity after a system characterization [94, 95].

Such solutions have the advantage of exploiting the whole input characteristic of the RFID circuit specifically designed to operate in the designated frequency band, leading to excellent sensitivity and compactness. Most chipless RFIDs, however, have environmental limits and cannot operate under extremely harsh conditions. Many industrial applications, for example, require the remote measurement of temperatures greater than 300 °C. For those temperature ranges, reliable and accurate resistive temperature detectors (RTDs) have already been developed and successfully employed for several decades [96].

3.1 RFID Sensing

Along with the increasing popularity of wireless sensor networks (WSNs), the interest for their integration with passive RFID technologies is also growing in scientific communities. The processing of backscattered signals reflected by RFID tags has become a low-cost alternative to remote sensing [97]. Compared to battery-powered, or passively-powered RFID tags, passive RFID tags are cheaper, lighter, and have a potentially longer lifetime. As explained in the following, they consist in the integration of a passive sensor into a chipless tag. The tag response to the reader interrogation is affected by physical modifications induced by its sensing part, making environmental quantities detectable at the reader side.

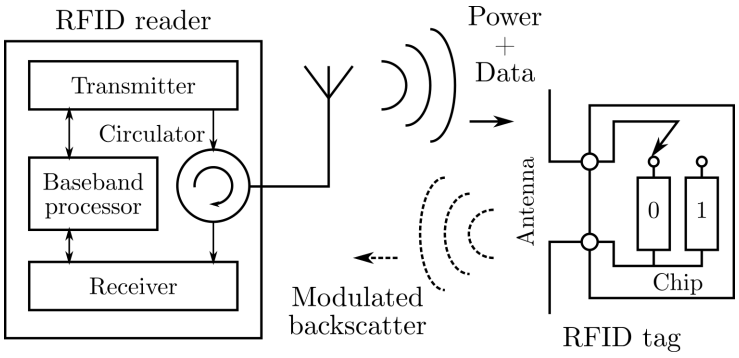

Figure 3.2: Overview of a passive RFID system.

3.1.1 System Operation

The operation of a passive RFID system can be described as illustrated in Fig. 3.2 [98]. A typical system is composed by an RFID *tag* and a base station, referred to as RFID *reader*. The tag may be passive, as in Fig. 3.2. In this case, it consists of an antenna and application-specific integrated circuit (ASIC) chip, characterised by complex impedances. The purpose of signal transmitted by the reader is twofold: first, the tag powering; second, sensing commands or queries to the tag. On the tag side, the received power allows to send data back by switching the chip impedance between two states, logically '0' and '1', physically *high* impedance and *low* impedance, for instance. This results into a modulation of the backscattered signal.

The data modulation of the transmitted and backscattered signals can employ different coding schemes (e.g. Manchester coding over amplitude modulation). In Fig 3.3, a simplified data exchange between an RFID reader and a tag is shown. As can be seen, the transmitted signal is composed by both a continuous wave (CW) and modulated commands (e.g. interrogations). At the tag side, the operation is divided into several phases: first, the tag exploits the CW to build-up electric charge into an internal capacitor, which provides the energy to perform subsequent

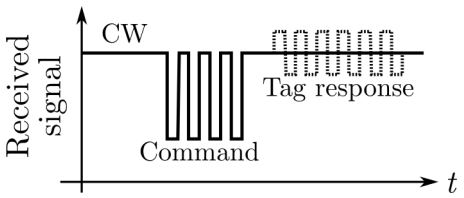

Figure 3.3: Simplified data exchange between RFID reader and tag.

actions; second, the powered IC interprets the received commands; third, in response, the chip sends data back to the reader by modulating the internal impedance accordingly; as a result, the impedance match (or mismatch) between the tag antenna and the IC is affected, resulting into the modulation of the backscattered signal. Back at the reader side, the receiver starts listening to incoming signals as soon as the transmitter has sent out the commands. The variation of the backscattered power, corresponding to the impedance mismatch, is detected and evaluated to infer the tag response.

3.1.2 Theory Formulation

In RFID tags both the antenna and the chip have complex impedances, namely $Z_a = R_a + jX_a$ and $Z_c = R_c + jX_c$. During the charge phase, it is important for the tag to match the two impedances (i.e. $Z_a = Z_c^*$), in order to maximise the power transfer to the charge capacitor. In fact, the fraction of the reader input power P_{in} that is absorbed by the tag is:

$$P_a = \left(\frac{\lambda_0}{4\pi d}\right)^2 G_R G_T \tau P_{\text{in}} \eta_p \,, \tag{3.1}$$

where λ_0 is the free-space wavelength, d the reader-tag distance, G_R is the gain of the reader antenna, G_T the gain of the tag antenna, τ the power transmission coefficient of the tag, defined as

$$\tau = \frac{4R_a R_c}{|Z_c + Z_a|^2} \,,$$

and η_p the polarization efficiency between the reader and the tag [99]. When the absorbed power by the tag exceeds its microchip sensitivity, the IC is able to receive commands from the reader and to send data back by backscattered modulation. The chip acts as a programmable switch between the two loads that define the modulating impedance Z_m. During the backscattering phase, the RFID system can be considered a *monostatic radar* [100], whose radar range equation is given by

$$\frac{P_r\left(d\right)}{P_{\text{in}}} = \sigma \frac{G_R^2}{4\pi} \left(\frac{\lambda_0}{4\pi d^2}\right)^2 ,$$

where $P_r\left(d\right)$ is the power received back by the reader at distance d and σ the radar cross section (RCS) defined as "the area intercepting that amount of power which, when scattered isotropically, produces at the receiver a density which is equal to that scattered by the actual target" [101]. In the case of an RFID tag, the RCS becomes [98]

$$\sigma = \frac{\lambda_0^2}{4\pi G_T^2 \rho} ,$$

where ρ is a modulation parameter resulting in

$$\rho = \frac{4R_a^2}{\left|Z_m + Z_a\right|^2} .$$

The radar range equation can be then rewritten as

$$\frac{P_r\left(d\right)}{P_{\text{in}}} = \left(\frac{\lambda_0}{4\pi d}\right)^4 G_R^2 G_T^2 \rho ,$$

which allows to evaluate the impact of the modulating impedance on the backscattered power. The low modulation state, virtually obtained by an open circuit $Z_m = \infty$, produces no significant backscatter, whereas the strongest backscatter is produced by a high modulation state, obtained

by either $Z_m = 0$ or $Z_m = Z_c$, depending on the chip family.

3.1.3 Chipless Sensing

Any antenna placed on, or in proximity of, a real object shows different radiation characteristics depending on the physical properties of the object itself. Likewise, in a RFID system, the strength of the backscattered power depends on the physical properties of the tagged object. In case of tags placed on objects with variable permittivity ε, for example, the absorbed power defined in Eq. 3.1 includes a dependency on both d and ε, i.e. $P_a = P_a(d, \varepsilon)$. Theoretically, if the distance between reader and tag is known, as well as the other static quantities that appear in Eq. 3.1, the change in the target permittivity could be detected by monitoring the backscattered power level at the reader side for a given Z_m. Traditional programmable tags (e.g. [25]) encode the digital sensor readout into the backscattered signal by switching Z_m between the two states. Conversely, chipless tags are loaded with a single element Z_L whose impedance strongly depends on a physical property of the object [102]; in case of permittivity, for example, $Z_L = Z_L(\varepsilon)$.

The system operation of a chipless RFID sensor tag is slightly different with respect to what described in Section 3.1.1. The reader, or radar, transmits a pulse, rather than a CW. The pulse hits the sensor tag, which acts as a scattering antenna, and the incoming wave is partially absorbed by the tag, partially backscattered toward the radar, as shown in Fig. 3.4. The tag has two scattering modes: the *structural* mode, which depends on the antenna topology; and the *tag* mode, which depends on the reflection coefficient Γ_L of the load. The higher the reflection coefficient, the stronger the tag-scattered pulse. The two backscattered pulses are spaced in time by adding a delay line between the antenna and the load.

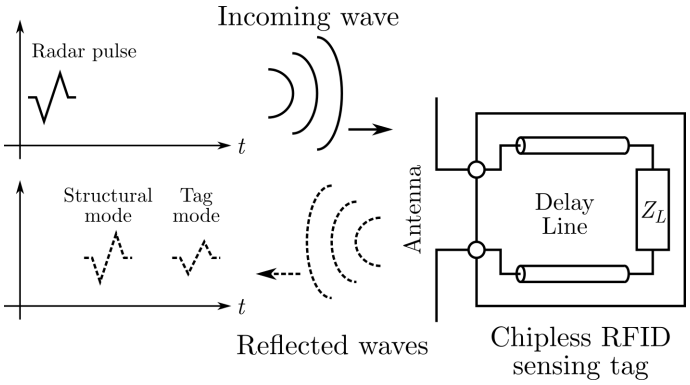

Figure 3.4: Model of a chipless RFID sensing system.

The ratio between the structural and tag modes can be used to estimate the load value. If its impedance Z_L is sensitive to any physical quantity of the object the tag is attached on, or immersed in, the same ratio can be used to extract the physical property of interest (e.g. ε).

3.1.4 Temperature Sensing

Programmable tags can be easily employed as temperature sensors. If the reader is within the range of activation of the tag, the radar successfully activates the chip that, in turn, carries out temperature conversion and backscattering modulation toward the reader [103].

In the case of chipless tags, the sensing strategy becomes more challenging. The sensing element can be as simple as a positive temperature sensor (PTS) used as tag load. Its resistance is strongly dependent on its temperature. This reflects into a temperature dependency of its reflection coefficient Γ_L, because of the mismatch with the transmission line impedance. It has been proved [94] that the ratio between the amplitudes of the structural and tag mode waves $\mathrm{ST_{ratio}}$ is related to the resistance value of the sensing element. In particular, a calibration technique can

be described by the following relationship:

$$\frac{\mathrm{ST}_{\mathrm{ratio}}\left(R_L\right)}{\mathrm{ST}_{\mathrm{ratio}}\left(R_{\max}\right)} = \frac{\Gamma_L\left(R_L\right)}{\Gamma_{\mathrm{DC}}\left(R_{\max}\right)},$$

where $R_{\max}$ is a preferably very large resistance, $\Gamma_{\mathrm{DC}}\left(R_{\max}\right)$ the ideal reflection coefficient at $R_{\max}$, and R_L the load value. Hence, after the calibration has been performed (i.e. $\mathrm{ST}_{\mathrm{ratio}}\left(R_{\max}\right)$ and $\Gamma_{\mathrm{DC}}\left(R_{\max}\right)$ have been measured once), the reflection coefficient can be estimated and the load resistance evaluated by measuring the actual ratio $\mathrm{ST}_{\mathrm{ratio}}\left(R_L\right)$:

$$\Gamma_L\left(R_L\right) = \Gamma_{\mathrm{DC}}\left(R_{\max}\right)\frac{\mathrm{ST}_{\mathrm{ratio}}\left(R_L\right)}{\mathrm{ST}_{\mathrm{ratio}}\left(R_{\max}\right)}$$
$$R_L = Z_0\,\frac{1+\Gamma_L\left(R_L\right)}{1-\Gamma_L\left(R_L\right)}.$$

3.2 Direct Passive Sensing

In case of resistive or capacitive measurements, chipless passive RFID sensing has some advantages compared to its chip-enabled counterpart. Compactness, temperature range of operation, robustness, to cite some. In general, however, the radio channel between the reader and the sensor increases the readout uncertainty in terms of resonance frequency shifts and attenuation. In fact, some chipless RFID are based on changes in phase of reflected signal, which may be unpredictably affected by the environment [104]. In other cases, the readout is achieved by estimating the reflected power by the sensor at the reader output port for a given frequency [69]; reasonably, in this case, if the radio channel cannot be characterised, the measurement uncertainty is even larger. In some cases, however, the channel is short, invariant, and very well known. This allows to include its model in the system characterisation and exclude such uncertainties, as also presented in [105]. Hence, sensing becomes

direct, other than *passive*.

3.2.1 Reflected Power Sensitivity

For high-temperature industrial equipment, resistive temperature sensors, or RTDs, are used. Thus, when used at the far end of a near field wireless resonant link (either inductive or capacitive) the RTD acts as the variable resistive load of the link, and the reflection coefficient Γ_L variations can be retrieved at the transmitter side [106, 34]. This work exploits this simple, well known circuital operation for converting the sensor (the link resistive load) data at the transmitter side of the near-field link. It is well known that if a near-field resonant link is time-invariant (i.e. the link distance/alignment is fixed), its resonant frequency does not change with load variations. Based on this knowledge, in the following, the analytical formulation of a novel passive sensor readout is developed, with reference to the very basic circuit model of the receiver part of the link, shown in Fig. 3.5. The voltage generator with its internal impedance represents the receiver input port and the load represents the sensor. Given the available power $P_{L\mathrm{av}}$, the reflected power is derived as $P_L^- = P_{L,\mathrm{av}} \cdot |\Gamma_L|$. As well-known from the maximum power transfer principle (MPTP) [107], in matched conditions, the reflected power is minimum and all the available power is delivered to the load, as shown in Fig. 3.5(b). In fact, considering the non-reactive load case, for the sake of simplicity, the incident power is

$$P_L^+ = \frac{1}{2}\left|V_g\right|^2 \frac{R_L}{\left(R_L + R_g\right)^2} = P_{L,\mathrm{av}} 4R_g \frac{R_L}{\left(R_L + R_g\right)^2}\,. \tag{3.2}$$

Since the reflected power P_L^- is computed as

$$P_L^- = P_{L,\mathrm{av}} - P_L^+\,, \tag{3.3}$$

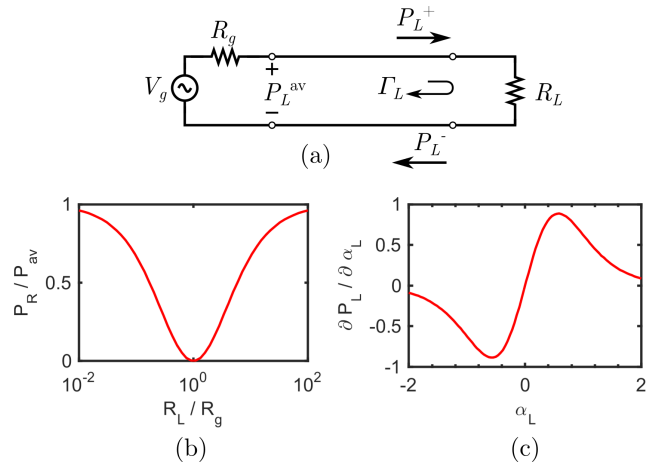

Figure 3.5: Maximum sensitivity mismatch explanation. (a) equivalent diagram; (b) normalized reflected power versus normalized load; (c) first derivative of the normalized power with respect to the 10-base logarithm of the load (see (6)).

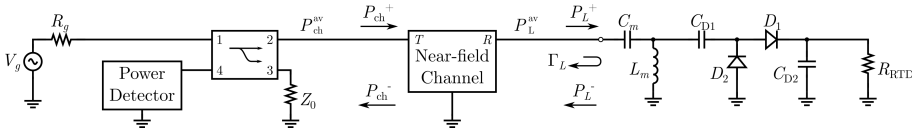

Figure 3.6: Block diagram of the direct passive sensing system.

its maximum sensitivity with respect to R_L can be found by its second derivative with respect to R_L:

$$\frac{\partial^2 P_L^-}{\partial R_L^2} = \frac{\partial^2 P_L^+}{\partial R_L^2} = 0\,. \tag{3.4}$$

In most cases, however, logarithmic variations of the load can be adopted, as in Fig. 3.5(b), which means that if the load is expressed as

$$R_L = 10^{\alpha_L}\,, \tag{3.5}$$

differences of α_L have equal weight, rather than of R_L itself. In other words, logarithmic quantities are compared instead of linear ones. For this reason, it is convenient to evaluate the derivative of P_L^- with respect

to α_L, as shown in Fig. 3.5(c). Solving

$$\frac{\partial^2 P_L^-}{\partial \alpha_L^2} = 0 \tag{3.6}$$

results in

$$\begin{aligned} \alpha_L &= \log\left(R_g\left(2 \pm \sqrt{3}\right)\right) , \\ R_L &= R_g\left(2 \pm \sqrt{3}\right) , \end{aligned} \tag{3.7}$$

which defines the optimal load values to maximize the sensitivity with respect to its small exponential variations. Thus, if the receiving part of the link is set to operate in such conditions, which can be called maximum sensitivity mismatching (MSM), a lot far from the conjugate matching, it is possible to reach the needed accuracy, at the transmitter side, to transduce the sensor measurement from the reflected power at the receiving side.

3.2.2 RF Rectifier for Industrial DC Probes

Industrial RTDs are uncommon loads for RF designs. Their severe parasitic components, especially parallel capacitances, make it impossible to supply such sensors directly at RF. This problem can be solved by introducing, between the link and the load, the rectifying part of a passive UHF RFID tag. This is shown in Fig. 3.6 where the RTD is driven by the rectified voltage and current of the RF excitation. The resulting nonlinear circuit of the link receiver side is optimised with the goal of providing the largest range of reflected power at its input port, with respect to the interval variations of the RTD load. During this nonlinear circuit optimisation the RF input power and the MSM components are used as the design variables. As will be shown by the numerical results of Section II, a quite high input RF power resulted at the end of the optimisation process. This is explained as the best trade-off to operate the

diode at such signal levels that the resistive losses are minimized [92]. It is noteworthy that, for the applications addressed in this work, the need for passive sensing capabilities is mandatory to get rid of sensor reading circuit and power supply at the high temperature sensor far end side, rather than to minimize power consumption.

3.2.3 Link Attenuation of Power Sensitivity

Up to this point, with reference to Fig. 3.6 where the transmitting and receiving link ports are referred to as T and R respectively, it is possible to evaluate the reflected power sensitivity at the receiver input port P_L^-. Unavoidably, the evaluation of the reflected power at the channel input port P_{ch}^- suffers from further reduction due to the link transmission coefficient S_{TR}. Thus, P_{ch}^- can be calculated as follows:

$$\begin{aligned} P_{\text{ch}}^- &= P_L^- \left|S_{TR}\right|^2 \\ &= P_{L,\text{av}} \left|\Gamma_L\right|^2 \left|S_{TR}\right|^2 \\ &= P_{\text{ch}}^+ \left|S_{RT}\right|^2 \left|\Gamma_L\right|^2 \left|S_{TR}\right|^2 \\ &= P_{\text{ch,av}} \left(1 - \left|S_{TT}\right|^2\right) \left|S_{RT}\right|^2 \left|\Gamma_L\right|^2 \left|S_{TR}\right|^2 , \end{aligned} \tag{3.8}$$

where $S_{ij},\ i,j = T,R$, refers to the scattering matrix of the near-field link of Fig. 3.6 and $P_{\text{ch,av}}$ is the power available at the link input. From (7), we infer that the link must be matched and lossless in order to minimize the contributes of reflected power and power loss due to the link itself.

3.2.4 Reflected Power Isolation

The reflected power at the channel input port can be easily decoupled from the other power contributes by exploiting the isolated port of a

directional coupler connected as shown in Fig. 3.6. Alternatively, a circulator can be used. In the case of circulator, we recall that the coupling factor C also indicates the fraction of the entering power from the through port 2 that is coupled to the isolated port 4 [108]:

$$C = 10 \log \left(\frac{P_1}{P_3} \right) = 10 \log \left(\frac{P_2}{P_4} \right) = -20 \log |S_{24}| \ , \qquad (3.9)$$

where the subscripts are referred to the convention of Fig. 3.6. Since a high $|S_{24}|$ is desired in order to detect reflected power variations, the coupling factor should be as low as possible.

Chapter 4

Industrial IPT Systems

Traditionally, electrical joints between static and rotatable parts of automatic machineries are realised by means of sliding contacts, usually slip rings. Older materials employed in sliding contact manufacturing were subject to early degradation, leading to unacceptable increase in the contact resistance. In order to overcome this phenomenon and improve contact reliability, some studies toward innovative brush plates were made [109]. In spite of that, rotatable joints represent a common point of failure, because their lifetime is strongly related to the cumulated number of revolutions. For this reason, contactless rotary joints would significantly increase the overall machine reliability, reducing costs of maintenance and the consequent downtimes.

In industrial environments, sliding contacts are often used to transfer electrical power to movable parts of automatic machines. The replacement of such hardwired joints, as well as moving power cables, with contactless energy transfer links has been widely envisaged in literature [44, 66, 13]. As reviewed by [1], several wireless energy transfer media can be employed, such as sound, light, capacitance, or inductance, depending on the application and the order of magnitude of the power to be

transferred. Among the possible IPT implementations, CET solutions represent wirelessly powered systems characterised by strong magnetic coupling, high efficiency, and relatively high power ratings [17, 48, 67]. Hence, CET systems meet the requirements of many industrial applications, such as robots, manipulators, sensors, and actuators. Literature provides several examples of CET units employed in industrial environments. For instance, units based on linear transformers [44, 67] can be used in electrical delivery systems for planar moving platforms such as drive belts, linearly moving motors, and power rails. Conversely, CET units based on rotary transformers [2, 18, 16], as in Fig. 1.10, are meant to replace rotary electrical joints. In fact, the *axial symmetry* of rotary transformers makes them innovative replacing units for the unreliable slip rings employed in rotary organs of automatic machines. As an example, in Fig. 4.1 the layout of a tea bag packaging machine is shown. Some rotary electrical tools of significant importance are highlighted. The replacement of their traditional sliding-contact supplying devices with CET units reflects into a considerable advantage in terms of reliability and overall performances.

Linear or sliding transformers are just a possibility to achieve WPT systems along rails or linear tracks, as envisaged in [fig:lineartrafo]. The increasing popularity of electric vehicles (EVs) contributed to research novel solutions for wireless powering 'on-the-move.' In the industry, wireless powered EVs can be exploited on a different scale. Sliding elements, or *movers*, may act as small autonomous convoys included into industrial equipment, such as a production line or an automatic machine. Movers, supplied by the coupled magnetic field, and controlled via an integrated wireless interface, are designed to transport certain items through predefined guided paths, selectively stop at particular stations along the

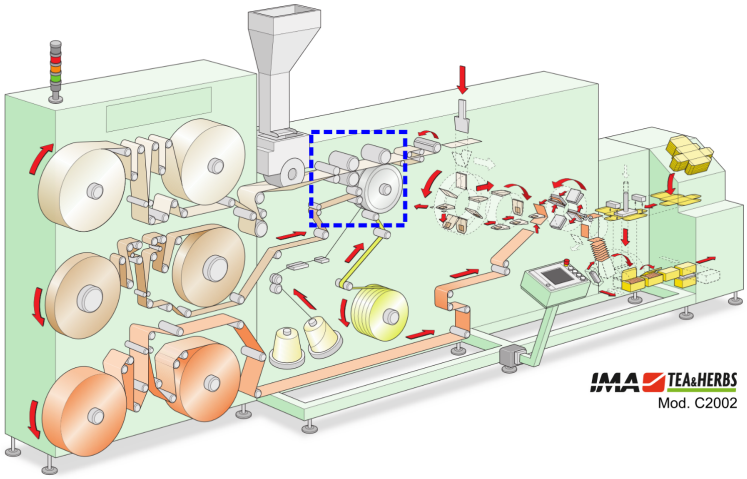

Figure 4.1: Layout of a tea bag packaging machine. The blue dashed box encloses rotary electrical tools traditionally supplied by means of slip rings. *Picture courtesy of I.M.A. SpA.*

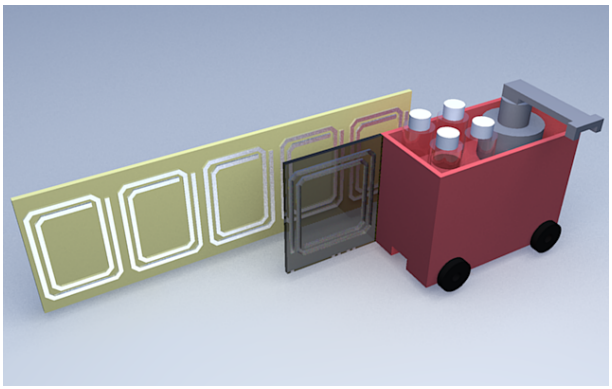

Figure 4.2: Concept design of a wirelessly powered mover.

path, and carry out some simple tasks by exploiting on-board manipulators. A schematic rendering of a wirelessly powered mover is shown in Fig. 4.2. The advantage of on-board energy availability is twofold: first to actuate the convoy by an electric motor along a mechanical guide; second, to perform tasks, such as item loading/unloading or item sealing, which are again actuated by on-board electrical work tools.

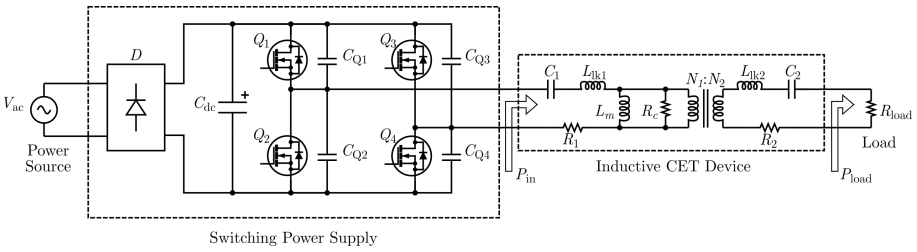

Figure 4.3: Circuit representation of the experimental CET system.

4.1 A Rotary CET Unit

In this section, a WPT inductive link based on a pot-core transformer to be used as replacement for the slip rings usually employed to supply sealing roller resistors is presented. Two different solutions for the pot-core transformer are discussed with respect to system efficiency, power factor (PF), and electro-magnetic compatibility (EMC), in order to define the best system configuration. This is first obtained by an accurate analysis of the system devices and of their interconnections based on the combination of circuital, electromagnetic and thermal simulations. Then the design results are validated by means of an extensive measurement campaign.

4.1.1 CET System Design

The experimental CET system shown in Fig 4.3 is now described according to its constitutive parts.

Rotary Transformer

The physical separation of the rotatable transformer is ensured by adding a small air gap (0.6 mm in our case) between the ferrite cores. The air gap does not break the magnetic flux path, though significantly reduces the coupling coefficient of the transformer. The decrease of the coupling coefficient is related to two main contributions: separation of the wind-

ings (discussed next), and increased core reluctance in proximity of the gap. As it will be evident in the next paragraph, however, these contributes can be included in the transformer model and their effect in terms of magnetic coupling can be accurately evaluated before prototyping.

An estimation of the core inductances, as represented in Fig. 1.4, can be obtained by following the reluctance-network approach presented in [110]. Single reluctances are computed starting from geometrical and magnetic properties of the core such as radii, widths, heights, and permeability. The electrical equivalent circuit is then solved to calculate primary, secondary, and mutual inductances, as known from magnetics theory.

Compensation

As discussed in Section 1.2, four different arrangements (SS, SP, PS, and PP) of the compensation capacitances are possible, depending on the positioning of each capacitance in series (S) or in parallel (P) to the primary or secondary winding, respectively. At the primary section, parallel-compensating capacitors have the disadvantage of depending on the load and on the magnetic coupling. Additionally, if parallel compensation is chosen at secondary side, this will cause a reactive behaviour at the primary side, thus requiring the primary compensation to consider magnetic coupling [4]. More sophisticated compensation techniques involve additional external resonators to act as impedance matching systems [111, 42]. Yet, SS compensation still represents a widely adopted solution, mainly because of its insensitivity to other parameters such as load and mutual inductance variations. In this case, series capacitors compensate the self-inductance at the desired resonance radian frequency

ω_0:

$$C_1 = \frac{1}{\omega_0^2 L_1}\,, \quad C_2 = \frac{1}{\omega_0^2 L_2}\,. \tag{4.1}$$

As a result, compensation also has the advantage to improve the PF of the IPT device, which can be evaluated as

$$\mathrm{PF} = \cos\left(\tan^{-1}\frac{\mathrm{Im}[Z_{\mathrm{in}}]}{\mathrm{Re}[Z_{\mathrm{in}}]}\right)\,, \tag{4.2}$$

where Z_{in} is the impedance at the input port if the CET unit.

Windings

In order to allow relative rotation, hence physical separation of the halves, the windings must be detached as well. In the case of automatic-machine applications, in which harsh environment conditions apply, the robustness and the reliability of rotating windings must be also taken into account. Due to the concentric geometry of the coaxial topology, radial tolerances of the windings should be as low as possible to prevent friction during rotation. For this reason, in order to guarantee high reliability despite of the limited tolerances of the wound-wire radius, we choose the adjacent winding topology, detailed in Section 1.6.2.

Power Converter

In *pseudo-resonant* (or *quasi-resonant*) full-bridge topologies, the switches turn on and off at zero voltage, and the input voltage of a switch is clamped at the input dc voltage. In addition, the inductive input impedance of the WPT unit can be exploited to store the energy controlled by the converter and ease the soft switching of its elements. For this reason it represents an excellent choice and it has been selected for the purpose of this experiment.

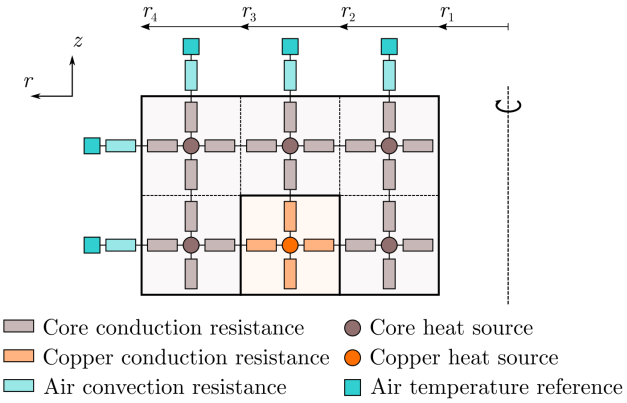

Figure 4.4: Thermal model of the pot-core half.

The electric diagram of the selected quasi-resonant converter is also shown in Fig. 4.3. The zero-voltage switching is obtained through two resonant intervals, as explained in Section 2.2: the 'passive-to-active' transition and the 'active-to-passive' transition. The former occurs when Q_2 and D_4 (i.e. the diode in parallel with Q_4) conducts, and Q_2 is turned off; the current in the primary winding causes C_{Q1} and C_{Q2} to charge by resonance with the primary inductance; then D_1 clamps the voltage across Q_1, and the switch can turn on at zero voltage. Conversely, the latter initiates when Q_4 is turned off; the current drained by the inductance charges C_{Q3} and C_{Q4}, and as soon as D_3 becomes forward-biased, Q_3 can be turned on at zero-voltage switching.

4.1.2 Thermal Analysis

The estimation of the core temperature is essential to verify that the ferrite operates close to optimal thermal conditions in order to reduce power losses. Such optimal thermal range for soft ferrites usually spans from 60 to 80 degrees.

The electrical equivalent of the *thermal resistance* can be used to estimate the core temperature, given its power losses [55]. Each pot-core

half can be divided into several regions, connected together by thermal resistances, as shown in Fig. 4.4.The smaller the regions, the more accurate the temperature estimation. Thermal resistances may be due to either heat *conduction* (within the structure of the core), or heat *convection* (across the boundary).

$$R_{\text{th,conv}} = \begin{cases} \frac{\Delta z}{h_d A} & \text{for the axial case } z \\ \frac{\ln(r_o/r_i)}{2\pi h_d \Delta z} & \text{for the radial case } r\,, \end{cases}$$

where Δz is the length of the axial segment considered; r_o, r_i are the outer and inner radii along the radial direction r; A is the considered area in the radian plane (i.e. $\pi(r_o^2 - r_i^2)$); and h_d represents the thermal conductivity, which lies between 3.5 and 5.0 $\text{Wm}^{-1}\text{K}^{-1}$ for MnZn ferrite and corresponds to 394 $\text{Wm}^{-1}\text{K}^{-1}$ for copper. The convection resistance assumes the following expression:

$$R_{\text{th,conv}} = \frac{1}{h_v A}\,,$$

where h_v is the convection heat-transfer coefficient, which depends on the boundary geometry, the temperature drop across the boundary, and properties of the external fluid. For a static cylinder immersed in air, h_v can be approximated to 12.7 and 8.5 $\text{Wm}^{-2}\text{K}^{-1}$ for the upper and the lower face (axial boundary), and its radial boundary, respectively.

The central spots of Fig. 4.4 represent heat sources. Five heat sources within the ferrite and one heat source within the copper for each half core are considered. Let P_c and P_w be the power dissipated within the core, and the copper, respectively. Then, under the assumption that the heat generation is equally distributed in the core, as well as in the copper, the heat supplied by each source is proportional to the respective volume

the source is located in. In Fig. 4.4 all the volumes have the same size, hence each core heat source supplies $P_c/10$ watts, whereas the copper heat source supplies $P_w/2$ watts, approximately. Since the transformer is considered symmetrical with respect to the gap plane, the proposed model fully describes its thermal behaviour.

In Section 1.5.4, an analytical procedure to estimate the core losses P_c is given.

4.1.3 Experimental Setups

A test bench able to transfer up to 1.3 kW through a CET device to a resistive load is now described. After applying the design procedure described in the previous section for a wide variety of configurations in terms of number of turns, wire types, and compensating capacitances, two different setups for experimental purposes are selected in order to verify the optimal trade-offs among efficiency, PF, feasibility, reliability, and EMC. The following rules have been chosen:

1. A purely-resistive equivalent input impedance (i.e. resonance condition) of the ICET link minimise the VA rating of the power supply. The equivalent input inductance of the ICET link, however, should not be completely compensated, otherwise the power inverter would require an additional inductor to achieve resonant commutation of its switches.

2. The copper losses increase with the winding wire length. Hence, the fewer turns, the better.

3. The ferrite losses increase with the magnetic flux density. Hence, the more turns, the better.

4. The voltage magnitude across C_1 (or C_2) decreases with the in-

Table 4.1: Configuration of setups.

	Setup 18	**Setup 27**
C_{Q1-4}	15 nF	5 nF
Litz wire	500×0.1 mm	84×0.18 mm
N_1	18	27
N_2	17	24
C_1	None	100 nF
C_2	None	None

verse of the capacitance, thus decreases with the increase in the inductance. Hence, the more turns, the better.

Results regarding the two setup, named *setup 18* and *setup 27* according to the number of primary turns, are discussed in the following. The two setups share the same ferrite core and the same inverter topology, whereas they differ on the number of turns and on the absence or presence of compensating capacitances, according to the different design priorities adopted. The main characteristics of the two setup configurations are summarised in Table 4.1.

The Ferroxcube P66/56 3C81-ferrite core is used in either setup as pot-core transformer [59]. The 3C81 material is a MnZn soft ferrite suitable for power applications at frequencies up to 200 kHz, with minimal losses around 70 °C. A switching frequency of 50 kHz is chosen, in order to contain ferrite losses and core heating.

The resistive nature of the welders requires the output waveform neither to be rectified nor to have sinusoidal shape. The employed ac/ac converter is built around a quasi-resonant full-bridge inverter that supplies a squared wave to the primary winding. Thanks to the integrated design procedure adopted, the inverter directly exploits the parasitic

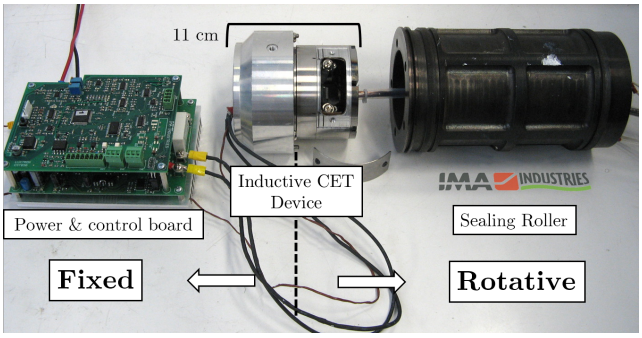

Figure 4.5: Test bench of the CET system.

leakage inductance of the transformer to achieve zero-voltage transitions on the switches, thus it does not require any additional series inductor to satisfy resonance conditions. The adopted power devices are four FDL100N50F FRFET MOSFETs manufactured by Fairchild Semiconductor. The value of the resistive load (44 Ω, fixed) is selected according to a large number of applications. Therefore, a feedback in the power supply design is not needed.

As suggested by Eq. 1.11, the use of litz wire for the windings is recommended to minimise the ac resistance. In litz wires, each copper strand is individually insulated from the others by a thin enamel coating, and the whole wire surface is wrapped in a two-layer Mylar film for further insulation. In either setup, the windings are wrapped in an adjacent fashion about two separate coil formers made in polyether ether ketone (PEEK) thermoplastic. A picture of the whole test bench is visible in Fig. 4.5.

The two experimental setups, emphasising the power loss minimisation in windings and the power factor maximisation, respectively, are now described in detail.

Setup 18

Minimal copper loss constraint is pursued by minimising the quantity expressed by Eq. 1.12.

The required litz strand section is ideal for 50-kHz signals, and the number of strands is maximised. Thick wires imply a small number of turns, resulting in greater ferrite losses. According to (1.10), at the selected frequency of 50 kHz the skin depth of copper is greater than 0.2 mm. Hence, a litz wire having a strand diameter of 0.1 mm can be adopted. In order to ensure a current density lower than 3 A/mm^2, 500 parallel strands are sufficient. 18 turns of the the resulting 500×0.1-mm strand litz wire fill the winding area of the core. The number of turns (17) of the secondary winding is chosen to obtain a suitable voltage on the load. According to (4.1), the lower the inductances, the higher the compensating capacitances. This may cause high voltage levels (almost prohibitive) at the capacitor terminals. For this reason, we avoided including any capacitive compensation, and therefore this setup is not intended to resonate. In the pseudo-resonant inverter, the parallel capacitances C_{Q1-4} are designed to ensure zero-voltage switches commutations at approximately 50 kHz; for the present configuration, the resulting C_{Q1-4} capacitances equal 15 nF.

Setup 27

Maximum PF constraint is pursued, which means minimisation of $\mathrm{Im}[Z_{\mathrm{in}}]$ in Eq. 4.2.

This requires the ICET device to operate close to its resonance frequency, at which $\mathrm{Im}[Z_{\mathrm{in}}]$ becomes sufficiently small. In this case, compensation capacitances must be included. In order to minimise space allocation at the secondary side, this experiment is carried out with

primary compensation only. Specifically, a primary capacitance of 100 nF results to be a suitable solution corresponding to a voltage drop of 300 V_{ac}, compatible with commercially available components. The input inductance of an ICET device composed by 27 primary turns and 24 secondary turns allows to operate in a pseudo-resonant condition, which is obtained by partially compensating the input inductance by the chosen series capacitor on the primary side. Indeed, a small input equivalent inductance is still necessary in order to ensure pseudo-resonance of the power supply. The inverter soft-switching is achieved by choosing capacitances C_{Q1-4} equal to 5 nF.

27 turns require the litz wire to reduce its section, in order to fit the primary winding in the area of the core. Commercially available 84×0.18-mm litz wire satisfies this requirement, although the resulting current density exceeds 4 A/mm^2. Thus, higher copper losses are expected.

Primary compensation results in an additional benefit consisting in the *LC*-network high-pass filtering on the low-frequency harmonics (e.g. due to the rectified 50-Hz mains), thus preventing the core from saturation. Moreover, as the input inductance increases, the higher harmonics are better rejected, thus improving system robustness from the EMI point of new.

A further tune of the inverter switching frequency and duty cycle has been performed on both prototypes to optimise soft-switching and ensure an optimal voltage on the load.

The thermal model of Fig. 4.4 is also used in either setup to estimate whether the core temperature might exceed maximum ratings during the heating cycles of the sealing rollers.

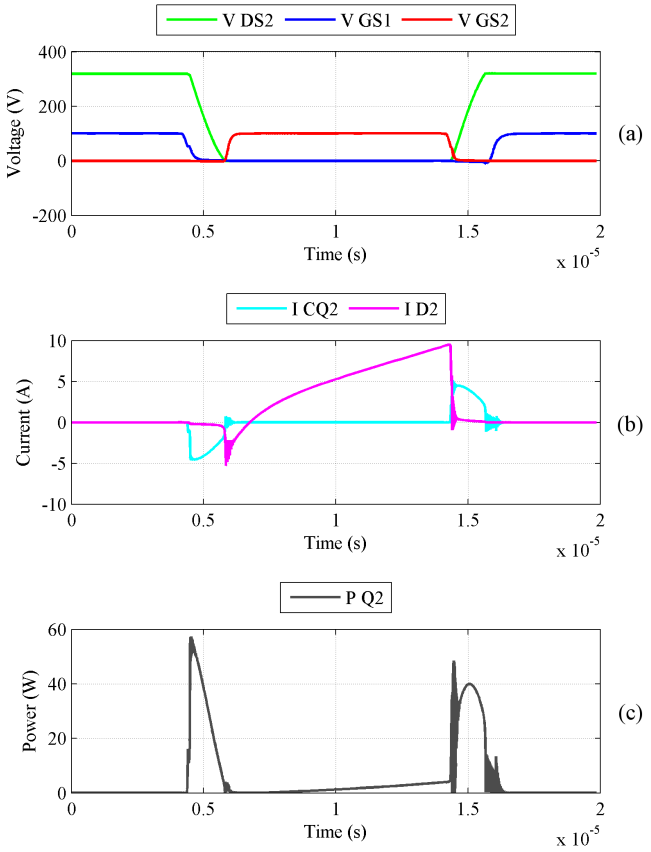

Figure 4.6: SPICE simulation of the ac/ac quasi-resonant converter for setup 18, with focus on Q_2. $V_{GS_{1,2}}$ are 10x magnified.

4.1.4 Results

In this section, the setups described above are numerically and experimentally characterised to validate the analytical models presented, including the finite element simulations of the pot-core transformer.

First, SPICE simulations of the converter are run, in order to verify that zero-voltage commutations are ensured in each setup. The plots of the inverter Q_2 voltage and current waveforms, reported in Figs. 4.6(a) and (b) respectively, confirm that design of the soft-switching behaviour is correctly reproduced. From the inspection of Fig. 4.6(c) it can be deduced that less than 5 Watts are wasted to support Q_2 commutations.

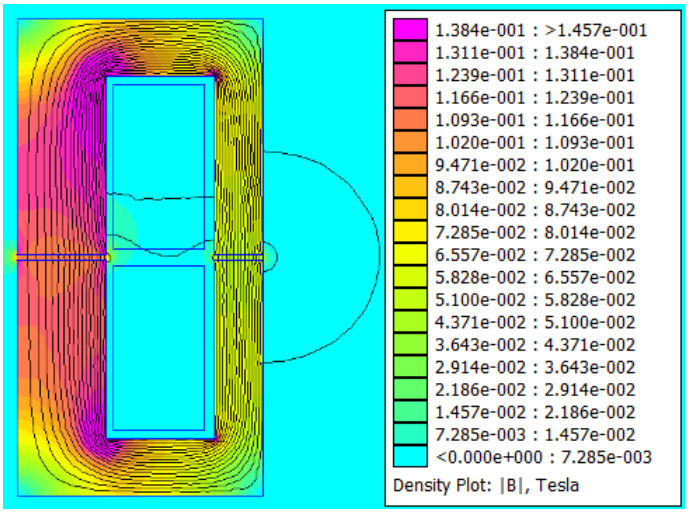

Figure 4.7: FEM simulation of the pot-core transformer showing the flux density and the flux lines for the setup 18 (FEMM software).

An extensive validation of the design approach is carried out and the electrical parameters of the circuit-equivalent model are compared with the results of the FEM simulation. Then, a systematic set of measurements are performed.

The FEM software used to compute the transformer electrical parameters is Finite Element Method Magnetics (FEMM) free software. FEMM is also used to simulate the magnetic flux density within the ferrite core in steady-state excitation conditions. Fig. 4.7 shows the magnitude of the **B** field and the flux lines for the setup 18. It is worth noting that the peak flux density, concentrated near the corners of the pot geometry, is well lower than the 3C81 ferrite saturation point (approximately 350 mT).

Comparisons among electrical parameters of the analytical model, FEM simulation based on the physical quantities of the CET link and the experimental measurements, are summarised in Table 4.2 for the two setups. Highly satisfactory results are obtained for all the parameters considered and small differences, among different domains of simulation,

Table 4.2: Electrical parameters of the transformers.

	Setup 18			Setup 27			
	Analyt.	**FEM**	**Meas.**	**Analyt.**	**FEM**	**Meas.**	**Units**
R_1	54.6	–	–	255	–	–	mΩ
R_2	47.2	–	–	174	–	–	mΩ
L_{lk1}	0.028	0.030	0.048	0.058	0.068	0.065	mH
L_{lk2}	0.025	0.027	0.010	0.050	0.053	0.049	mH
L_m	0.303	0.296	0.269	0.682	0.671	0.670	mH
L_1	0.331	0.326	0.317	0.739	0.736	0.735	mH
L_2	0.295	0.291	0.250	0.588	0.584	0.578	mH
M	0.286	0.279	0.254	0.606	0.597	0.596	mH
k	0.916	0.908	0.904	0.916	0.908	0.913	·

prove that the adopted model is able to provide accurate results.

As expected, windings resistance of setup 27 is greater than that of setup 18, due to the reduced litz wire diameter. The model inductances are also greater, because of the higher number of turns, whilst the coupling coefficients are similar.

In Fig. 4.8 the input impedance magnitude and phase of the ICET link are plotted for the two configurations. As can be derived from the

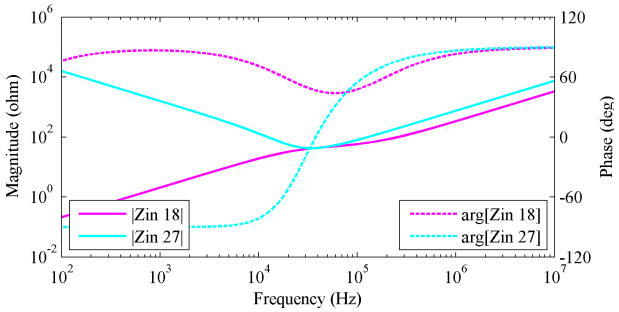

Figure 4.8: Input impedance magnitude and phase of the CET link ($R_{\mathrm{load}} = 44\ \Omega$).

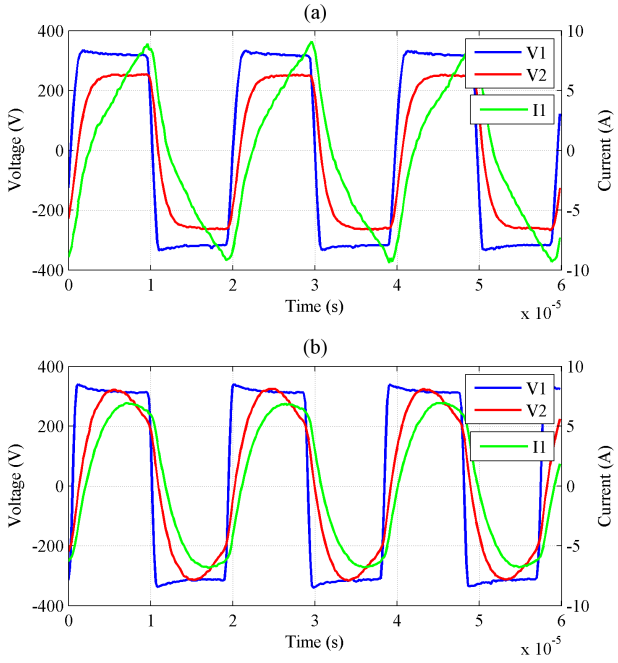

Figure 4.9: Measurement of primary and secondary winding voltage and primary current for: (a) setup 18; (b) setup 27.

plot, the resonance frequency of setup 27 lies at approximately 37 kHz. A switching frequency of 50 kHz ensures a high PF and, at the same time, enables pseudo-resonance of the power supply because of the residual inductive part of the input reactance.

Measures of the key waveforms of setup 18 and setup 27 are shown in Figs. 4.9 (a) and (b), respectively. The rough shape of the current waveform in setup 18 warns that severe EMI may occur in this configuration. In case of extensive wiring of the automatic machine, such interference might become a serious issue and must be taken into account. Fig. 4.10 shows the fast Fourier transform (FFT) spectra of the primary current in either setup. As setup 27 improves low-frequency rejection of primary current compared to setup 18, the higher-current harmonics only show a slight reduction due to the increased equivalent input inductance of setup 27.

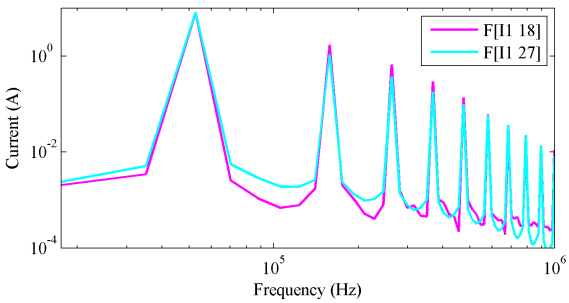

Figure 4.10: Computed FFT spectra of primary currents for the two setups.

Table 4.3: Losses and efficiency comparison.

	Setup 18	**Setup 27**	**Units**
Copper losses (estimated)	4	21	W
Ferrite losses (estimated)	13	8	W
Power factor (estimated)	0.718	0.938	·
Efficiency (estimated)	99.5	98.8	%
Efficiency (measured)	97.7	95.6	%

In Table 4.3 estimated losses, computed PFs, and measured efficiencies of the two setup are compared. Yet, the setup 27 represents a suitable solution for EMI, despite the slight inefficiency with respect to setup 18 and moderate additional efforts in terms of circuit complexity. Further tests should be carried out in order to verify the effective electro-magnetic compatibility of the proposed solutions.

Finally, the thermal model is used to estimate the temperature increase within the core with respect to the ambient temperature. Results for continuous power transfer operation are summarised in Table 4.4.

In real operating conditions of the automatic machine, however, the power transfer to the welding resistors is discontinuous and usually requires less than 50 % of the full duty cycle. This allows to predict a 50 % reduction in the temperature increase, at least.

Table 4.4: Core temperature increase.

	Setup 18	Setup 27	Units
Analytical model	55	134	°C
FEM simulation	57	152	°C
Error percentage	4	12	%

4.1.5 Remarks

The experiment proved that ICET links can be successfully employed as wireless rotary joints even beyond the kilowatt power level. This first experience 'on-the-field' shows that it is a good practise to set up different system configurations in order to find out the best trade-off that suits a particular application.

4.2 A Sliding WPT Application

Conceptually, movers are similar to moving vehicles models [65, 112], or to sliding loads in [66]. Usually, to solve the problem of variable couplings, long primary current loops are adopted, which unavoidably introduce large primary leakage inductances, and consequently a significant drop of the overall power transfer efficiency [20]. As an alternative, the segmentation of the transmitters, which allows a more energy efficient powering of the sliding path, is proposed. The last goal, whose achievement goes beyond the scope of this thesis, is the automatic serial activation of the transmitting coils along a certain path by sliding the movable one over them. It can be demonstrated that an optimum choice of the receiving and transmitting coil lengths exists, enabling a constant coupling coefficient, and thus a constant power transfer during the translation [113].

4.2.1 Analysis and Design

In a traditional moving vehicle scenario, the variation of the receiving coil position causes a significant oscillation of the coupling factor with the transmitters and thus a continuous variation of the transferred power. To overcome this issue, in [114], the proposed configuration has two transmitting coils active at a time. Tracking the load movement along the path, the coils turn on and off when the receiver is located on the previous and on the following transmitting coil, respectively. The distance, the shape, and the dimensions of the coils determine the variation of the coupling between transmitters and receiver.

Given the coil diagram of Fig. 4.11, where P_1, P_2, and P_3 represent the ports of the receiver, a first transmitter, and a second transmitter, respectively, the coupling factor between two ports, i and j is defined as

$$k_{ij} = \frac{\mathrm{Im}\left(Z_{ij}\right)}{\sqrt{\mathrm{Im}\left(Z_{ii}\right)\mathrm{Im}\left(Z_{jj}\right)}}\,, \tag{4.3}$$

where the impedances belong to the reciprocal impedance matrix $\mathbf{Z}$ defined as in the following relationship (voltages and currents are referred to respective ports):

$$\begin{bmatrix} V_1 \\ V_2 \\ V_3 \end{bmatrix} = \begin{bmatrix} Z_{11} & Z_{12} & Z_{13} \\ Z_{12} & Z_{22} & Z_{23} \\ Z_{13} & Z_{23} & Z_{33} \end{bmatrix} \begin{bmatrix} I_1 \\ I_2 \\ I_3 \end{bmatrix}\,.$$

In case of a series connection of transmitting ports P_2 and P_3, the system can be simplified to a 2-port network (P_1 and P_2'):

$$\begin{bmatrix} V_1 \\ V_2' \end{bmatrix} = \begin{bmatrix} Z_{11} & Z_{12}' \\ Z_{12}' & Z_{22}' \end{bmatrix} \begin{bmatrix} I_1 \\ I_2' \end{bmatrix}\,,$$

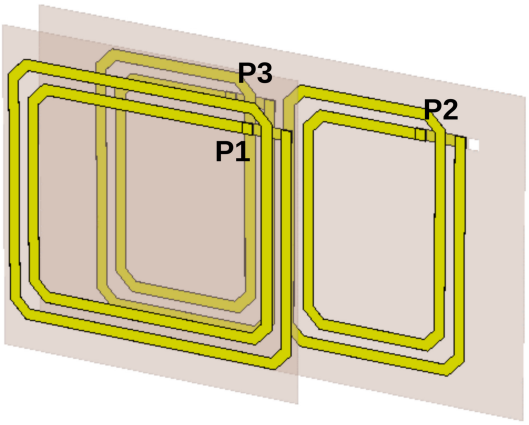

Figure 4.11: Example of planar coils for a sliding system.

where Z'_{12} and Z'_{22} are given by

$$Z'_{12} = Z_{12} + Z_{13}\,,$$
$$Z'_{22} = Z_{22} + 2Z_{23} + Z_{33}\,.$$

In case of identical transmitting coils, by using Eq. 4.3, the coupling factor between the P_1 and P'_2 becomes

$$k'_{12} = \frac{1}{\sqrt{2}} \frac{k_{12} + k_{13}}{\sqrt{1 + k_{23}}}\,.$$

Similar expressions can be derived in case of parallel connection of ports P_2 and P_3.

Given the geometrical definitions of Fig. 4.12, a numerical optimisation has been carried out to optimise the shape of the coils in order to obtain a flat coupling factor k'_{12} regardless the position of the receiving coil (P_1). Results are shown in Fig. 4.13 and Fig. 4.14 for different shapes and link distances. Simulated results have been also experimentally validated by measurements whose results are also plotted in Fig. 4.14. A photograph of the setup is shown in Fig. 4.15.

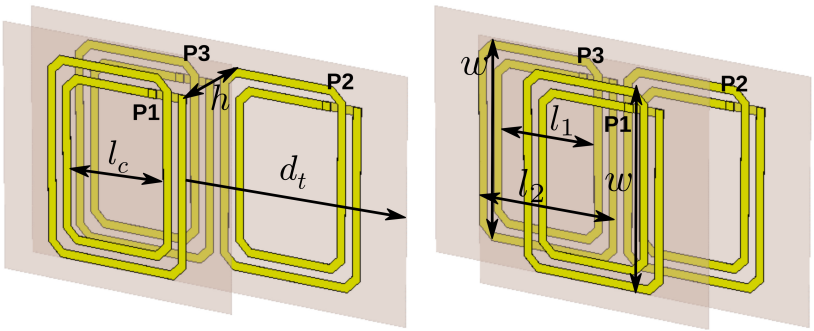

Figure 4.12: Geometrical definitions of the planar coils used for numerical optimisation.

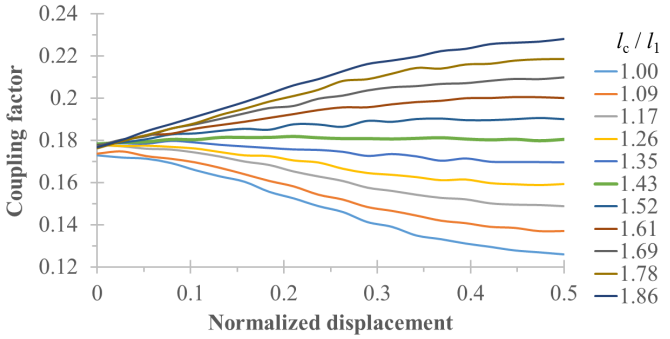

Figure 4.13: Coupling factor between moving and fixed coils connected in series as a function of the normalized displacement d_t ($l_1 = 118$ mm, $l_2 = 176$ mm, $w = 236$ mm, $h = 60$ mm).

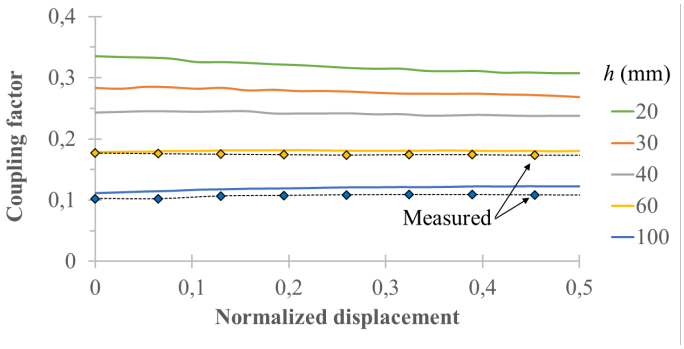

Figure 4.14: Measured and predicted coupling factor between the moving and the series-connected fixed coils, as a function of the normalized displacement d_t for different link distance h ($l_1 = 118$ mm, $l_2 = 176$ mm, $w = 236$ mm, $h = 60$ mm).

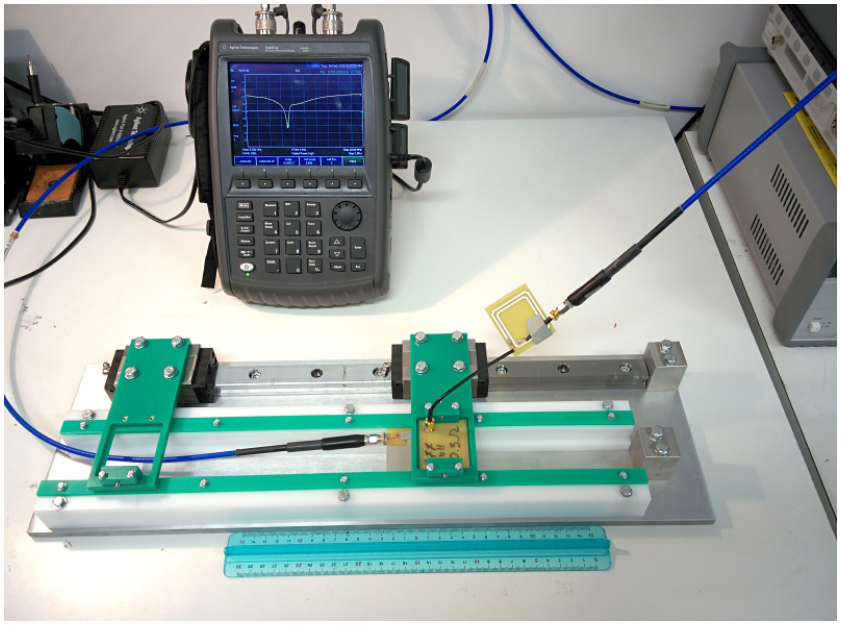

Figure 4.15: Photograph of the setup used for experimental validation. Transmitting coils are placed beneath the visible receiving coil. The system is downscaled for testing purposes.

4.2.2 Circuit Simulation

The lumped-element circuit equivalent of the optimised geometry is employed to simulate the entire link. Since the system is modular, as an arbitrary number of transmitting coils can be used, the simulation includes four transmitters. Given a constant-frequency constant-amplitude voltage source V_S, a network of switches is designed to ensure only the necessary coils are active at a time. Three switches are necessary for each transmitter, as shown in the system configuration depicted in Fig. 4.16.

By recalling the considerations of Section 2.1, a constant-amplitude voltage source at the primary side generates a constant-amplitude current at the secondary side, and vice-versa. The statement holds for any circuit that includes an *immittance inverter*, as mutually coupled inductors. In Section 2.4, this concept is exploited to describe a hybrid IPT

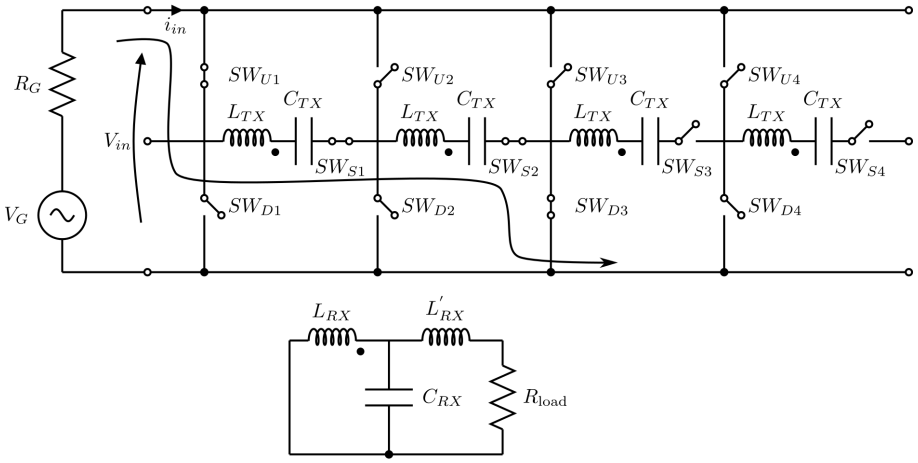

Figure 4.16: Circuit representation of the entire sliding link showing the current path when the receiving coil is located between the first two transmitting coils. The system is modular and can be replied by repeating the cell.

supply that converts a voltage generator into a current generator. In this case, the inductive link acts as a first immittance inverter that converts the primary-side voltage into a secondary-side current. Hence, a second immittance inverter is necessary to convert the secondary-side current into a load-side voltage. The immittance inverter can be either inserted between the power supply and the primary side of the link, or between the secondary side of the link and the final load. For convenience, the latter solution is adopted. The immittance inverter is also shown in Fig. 4.16: it consists of the secondary proper inductance L_{RX}, the mirror inductance $L'_{RX} = L_{RX}$, and the resonating capacitor $C_{RX} = 1/\left(\omega_0^2 L_{RX}\right)$. These three elements form an LCL network, as described in Section 2.4.

In Fig. 4.16, a specific current path through switches SW_{U1}, SW_{S1}, SW_{S2}, and SW_{D3} is shown. The receiving coil is supposed to stand between the first two transmitting coils. This configuration is simulated for $V_G = 1\,\text{V}$, $R_G = 50\,\Omega$, and $R_{\text{load}} = [1, 1000]\ \Omega$ and the results are shown in Fig. 4.17. Voltage curves are almost superimposable and this confirms the correctness of the chosen design approach. Output voltage

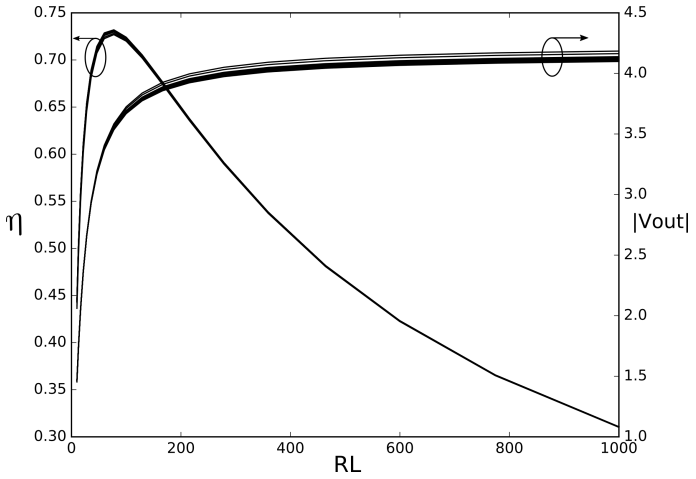

Figure 4.17: Predicted output voltage and power transfer efficiency of the link configured as in Fig. 4.16. The plots parameter is the receiver displacement d_t.

variations are lower than 1.2 % for any receiver position. For large load values (well greater than component losses) an almost constant output voltage can be observed, which is also a primary requirement of the proposed system architecture.

4.2.3 Remarks

This experiment proved the great potential of a modular sliding WPT system. Blocks can be assembled together to realize a linear track along a straight or curve path, as required by industrial equipment that employ intelligent movers. The switching network, whose design has to be finalised yet, represents a key aspect of the system: conduction losses should be minimised and the electric model during commutations must be carefully investigated for a realistic prediction of the system behaviour.

Chapter 5

Passive Sensing for WPT Systems

The exploitation of WPT in industrial applications can be intended for two different purposes: first, the contactless energy transfer in order to power industrial loads (i.e. power greater than 1 kW) or electric subsystems (i.e. power lower than 1 kW) [18, 69]; second, to achieve passive sensing by analysing the backscattered signal or estimating the remote load value [103, 115]. The combination of the two purposes gives incomparable benefits in designing wireless interfaces between static and moving mechanical assemblies.

Some wireless industrial designs do not necessarily have to cover large distances. In some cases, the contactless link is as short as a few millimeters, or even less, in order to replace traditional sliding contact devices with compact WPT units. As envisaged in [28, 116], it is possible to enclose a CET unit and a short-range wireless data link into a single WPT device. From the industry perspective, this represents an actual advantage because single WPT devices can ensure backward compatibility with existing wired interfaces, simplifying spare part replacements for techno-

logy update. Traditional wired interfaces, indeed, are usually based on multiple sliding contacts (e.g. slip rings) connected to power circuits and data links. Hence, the update procedure is pretty simple: power connections will be joined to the power port of the WPT device, whereas link connections to its data port.

5.1 WPT with Temperature Sensing at UHF

Recently, data transmission in rotary assemblies has been proposed in [103], by adopting sensor enabled RFID systems. This approach still requires an MCU at the remote side to modulate the backscattered tag signal with the sensor data.

In this experiment, we present an innovative solution combining wireless power and information transfer (WPIT), which pairs an RFID-based passive sensor link with the ferrite-based power CET 'setup 27' tested in Section 4.1.3, to be employed in a temperature-controlled heating system. Electric and magnetic coupling links are co-designed to simultaneously performs the two operations without interference. A new exploitation of the RFID technology is adopted in such a way that no active electronic circuitry is required in order to provide the temperature readout. The system design is optimised to be used with industrial resistive temperature probes in the range [0, 300] °C. The procedure to design layout-wise the entire system is described and an extensive experimental validation is provided.

5.1.1 Capacitive Data Channel

As previously described, the wireless power link of a WPIT unit is generally based on magnetically-coupled ferrite-wound coils, resonant or non-resonant depending on the level of power to be transferred, which could

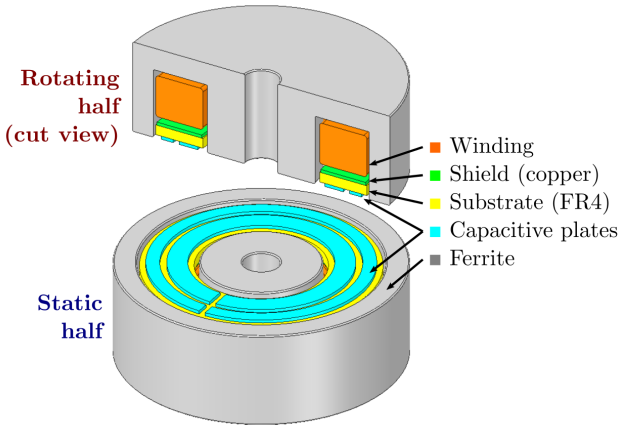

Figure 5.1: Cut view of a rotating implementation of a WPIT device. Small capacitive plates lay on top of the windings.

be at the kW level. On the contrary, the channel for the wireless information transfer does not have strong power requirements, and the ferrite cores can be omitted. The physical interface can be realized by small coils, or even by exploiting the electric field rather than the magnetic one (i.e. capacitive power transfer, CPT, instead of IPT). In this case, two pairs of capacitive plates are implemented. To comply with mechanical constraints, we include, as in [28], capacitive plates in the winding area of rotating cores (see Fig. 5.1), thus obtaining a very compact design. In this first realization the selected operating frequency is the ISO/IEC 14443 RFID standard frequency (13.56 MHz).

The simplified lumped-element equivalent circuits of the IPT and CPT units for power and data transfer, respectively, are reported in Fig. 5.2(a). The advantage of exploiting different fields for power (magnetic) and data (electric) is that the parasitic coupling between the two is negligible, and they can be modelled as isolated sub-systems. This is a significant advantage for high-power systems, where exploitation of IPT for both power and data [117] is not possible due to excessive cross coupling. Fig. 5.2(b) shows the CPT link layout and the corresponding

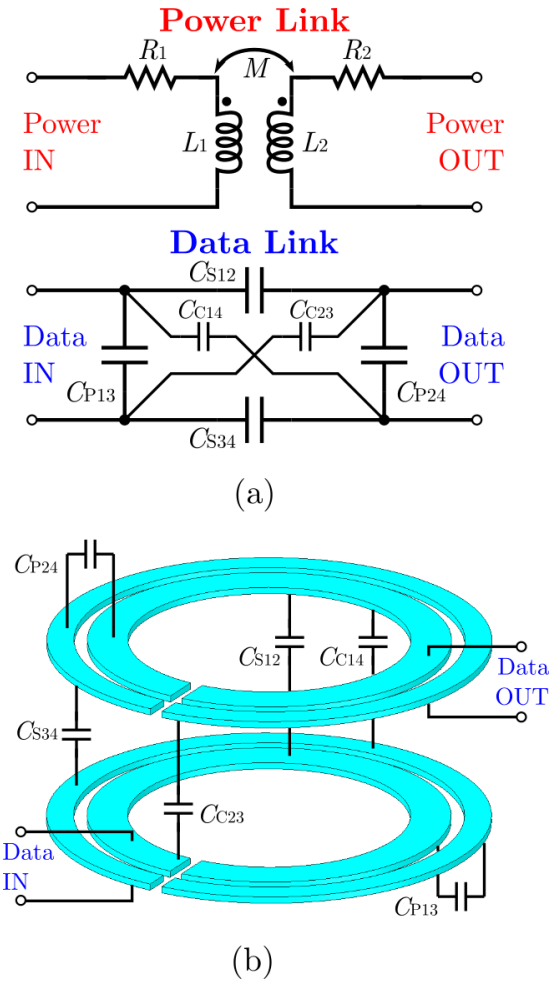

Figure 5.2: (a) equivalent electric diagram of a WPIT device that implements an IPT unit as power link and a CPT unit as data link; (b) physical realization of the CPT link.

equivalent components of the data link, including the parasitic ones. In particular, parallel and cross capacitances (C_{P13}, C_{P24} and C_{C14}, C_{C23}, respectively) are responsible for a significant increase in the link insertion loss and need to be minimized by an overall link optimisation.

5.1.2 Direct Passive Sensing Implementation

Due to the severe parasitic components of industrial probes—not to be supplied at RF—the RF output port of the CPT link cannot be loaded directly with the sensor. This problem can be overcome by inserting

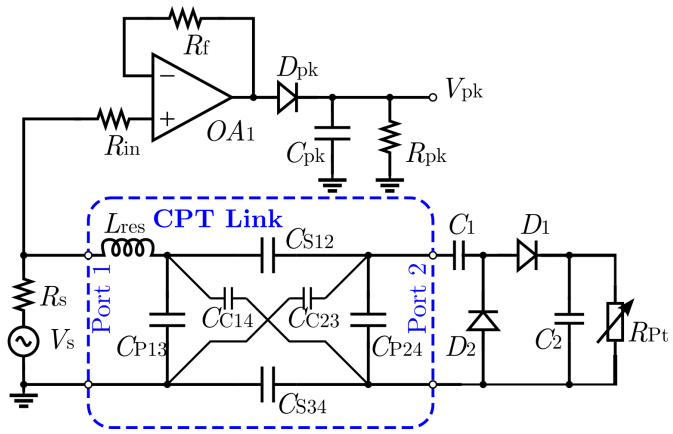

Figure 5.3: Electric diagram of the DP-RFID link.

between the link and the load an RF-to-dc rectifier, commonly used in passive tags. The system has been referred to as direct passive RFID (DP-RFID) [90]. This is shown in Fig. 5.3, where the entire system overview is presented. The inductor L_{res} is designed to resonate with the link series capacitances (i.e. C_{S12} and C_{S34} of Fig. 5.2). It is worthy to note that the active electronic circuitry is on the reader side only and is based on an opamp peak detector to sense the voltage magnitude. Such detector features a high-input impedance in order not to affect the measured voltage.

5.1.3 Experimental System Results

A prototype of the system has been built, and a photograph of its main sub-blocks is shown in Fig. 5.4. The top view of one link branch and the corresponding optimised dimensions of the capacitive plates are shown in Fig. 5.5 and Table 5.2, respectively. A lumped-element equivalent circuit of the CPT link has also been identified, according to the network of Fig. 5.3 and the numerical values of the equivalent capacitances are reported in Table 5.1. A 1.6 mm-FR4 substrate has been adopted, with a copper thickness of 35 μm; the distance between opposite plates (i.e. the air gap

Table 5.1: DP-RFID component values.

Ref.	Value	Units	Ref.	Value	Units
R_f	10	Ω	C_{S12}	13.7	pF
R_{in}	47	Ω	C_{P13}	13.3	pF
R_{pk}	100	Ω	C_{C14}	2.3	pF
R_s	50	Ω	C_{S34}	13.7	pF
L_{res}	5.6	μH	C_{P24}	13.4	pF
C_1	68	pF	C_{C23}	2.3	pF
C_2	100	nF	D_{pk}	MMDL770T1G	
C_{pk}	100	nF	$D_{1,2}$	MMDL101T1G	
V_s	3.0	nF	OA_1	LT1818CS8	
f_s	14.26	MHz			

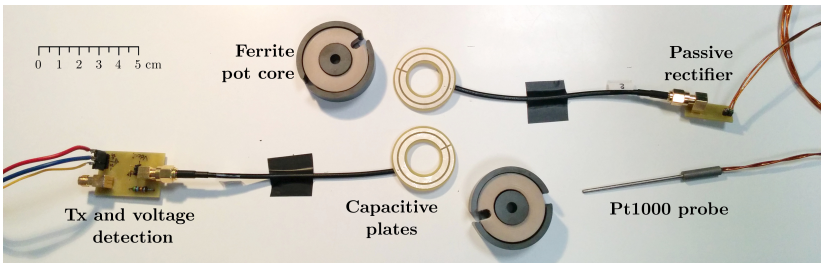

Figure 5.4: Picture of the prototype.

between the two halves of Fig. 5.1) is 0.5 mm. The sensing element RPt is a custom industrial Pt1000 temperature probe operating between 0 and 300 °C; the corresponding resistance variation range is [1000, 2121] Ω.

To validate the design procedure, the system has been characterized by means of EM simulations, equivalent circuit model, and VNA measurements. Fig. 5.6 shows the S_{21}-parameter comparison for these three cases of the CPT link (including L_{res}) of Fig. 5.3. Very good agreement is obtained between the EM simulations and the optimised equivalent

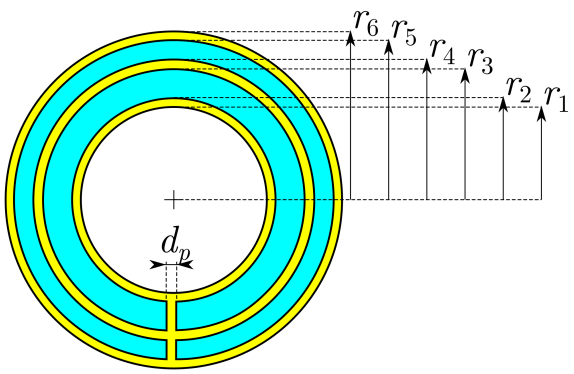

Figure 5.5: Geometrical definitions of the prototyped DP-RFID link.

Table 5.2: Geometrical dimensions of the DP-RFID link.

Quantity	Value	Units
r_1	9.6	mm
r_2	10.5	mm
r_3	13.5	mm
r_4	14.5	mm
r_5	16.5	mm
r_6	17.4	mm
d_p	1.0	mm

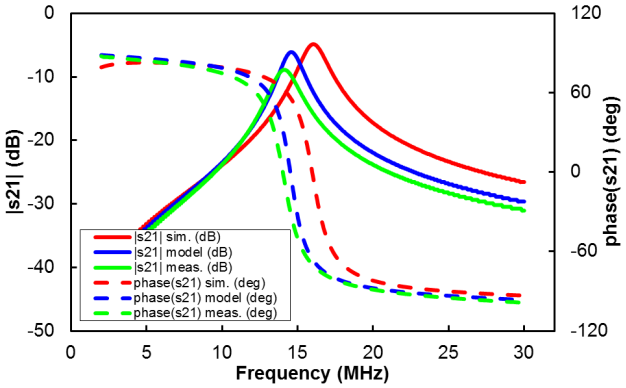

Figure 5.6: S_{21} of the resonant capacitive link: numerical simulation, equivalent circuit model, and VNA measures are compared.

circuit model. A slight deviation from measured results is observed in terms of resonance frequency (9 %). This may be due to the parasitic effects of connections whose equivalent models were not included in the simulation. A 15% frequency shift with respect to the nominal operating one was also observed, which will be tuned in the second run of the design.

Measured results of the sensor readout are summarized in Fig. 5.7. The plot shows the voltage magnitude at the peak detector output V_{pk} and the power entering the CPT link versus temperature, measured by the Pt1000 resistive sensor (see Fig. 5.3). Temperature values have been simultaneously verified by an independent thermometer. The range magnitude spans from 1.40 to 1.49 V, resulting in a 90-mV range. Not a wide scale, but larger than an E-type thermocouple junction (roughly 22 mV) in the same temperature extent.

This first characterization has been carried out without including the ferrite body and the windings of the WPT unit. In order to rule out possible interferences of the WPT unit on the data link performances, the insertion loss of the capacitive link has been numerically simulated with and without the WPT unit body. A very reduced deviation was observed

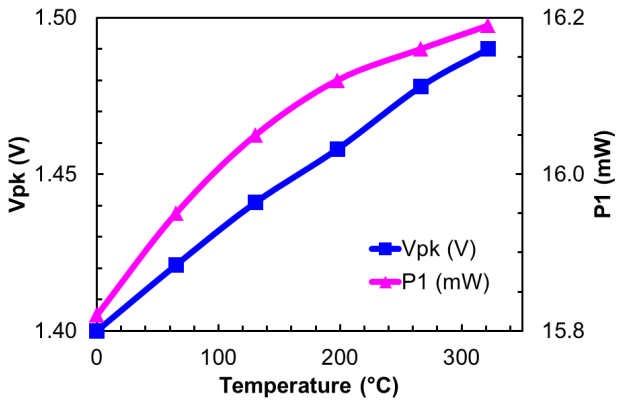

Figure 5.7: Measured voltage at the peak detector output and estimated power input versus sensed temperature.

in the S_{21} indicating that the WPT unit does not substantially modify the data link, indicating that the proposed solution can be implemented in a complete WPIT system.

5.1.4 Remarks

Due to the relatively low value of the link capacitances, large resonant inductors are needed. Thus, to contain inductor losses at RF, special attention should be paid to its choice. Furthermore, inductances in the order of the μH may have a wide tolerance at the RFID frequency. Hence, small deviations from their nominal value produce significant shifts of the link resonant frequency, representing a critical issue if cheap components are employed.

5.2 UHF Sensing Link

Following the research activity through this topic by expanding the previous experimental step, where a 13.56-MHz capacitive link is exploited for remote temperature sensing, in this section the design of a UHF link based on near-field coupled split-ring resonators for a passive sensing

platform is introduced. The link is intended to be adapted to the existing wireless power transfer (WPT) system. Numerical and experimental validations of the UHF link itself and of the entire sensing system are also provided. The fundamental aspects of the proposed remote sensing technique are discussed, which are based on the exploitation of the mismatch between the source and the load of the rectifying side of a near-field link for WPT; the near-field link is described more in detail by focusing on the choices of its physical layout and compares this solution with a previously proposed low-frequency realization of the link based on coupled capacitive plates [118]; finally, the experimental validation for the split ring resonator-based UHF near-field link and for the entire chain realized for the readout of a remote sensor temperature are provided.

5.2.1 Near-Field Resonating Link

In the previous section, the possibility to integrate independent power and sensing links into a single WPT device was presented. In order to provide a reliable solution, a different approach is presented here, with respect to [118]. The main goal is to overcome loss and tolerance issues reported in such work due to lumped resonating elements represented by fixed inductors. First, the link operating frequency is shifted up to 868 MHz, which makes an uncommon choice for near-field design, though fully compliant with RFID standards [17]. Consequently, the sensing link cannot be characterized as a capacitive one anymore. Now, at 868 MHz, the plates behave as strip conductors, having their length of the order of the wavelength, and thus also exhibit a self- and mutual-inductive behaviour. Finally, such strips realize an auto-resonant structure, as shown in the following. This allows to drop the performance limitations set by tolerance and loss of external resonating inductors, as they are

not necessary any more.

A possible solution, compatible with the geometric constraints of [118] is to use the same capacitive plates in a split-ring resonator (SRR) arrangement. These structures were first proposed in [119] to obtain an effective magnetic permeability in nonmagnetic conducting materials. Sensing platforms based on SRRs have also been proposed [120]. In these cases, however, the SRR is used as the passive sensing element. Differently, as will be shown in the following, SRRs can be successfully exploited in the near-field wireless link as self-resonant reactive structures to achieve power or data transfer [121].

Single SRR

The geometric shape of the SRR is shown in Fig. 5.8. The two open rings resemble the capacitive plates of Fig. 5.1, although the inner ring is 180°-rotated and both microstrips have the same width in the case of the SRR. Many authors proposed equivalent circuital representations of SRRs [122, 123, 124]. In this case, for a single SRR with ground plane, the model proposed in [125] and shown in Fig. 5.9 was used inside our circuit simulator, validated by EM simulations and resulted to consistently represent its circuital behaviour. It consist of the two pairs of coupled transmission lines TL_{11}, TL_{21} and TL_{25}, TL_{15} that model the SRR in the absence of the slots. The transmission lines $TL_{12,14,16,17}$ account for the length difference of the external microstrips. The slots circuital contributions are modeled as a π-network of capacitances, whose values are derived by circuit optimisation, with the goal of matching the EM simulated [118] S-parameter over the frequency band of interest. To do so, two further lines $TL_{13,23}$ model the opposite microstrip segments with respect to the slot positions.

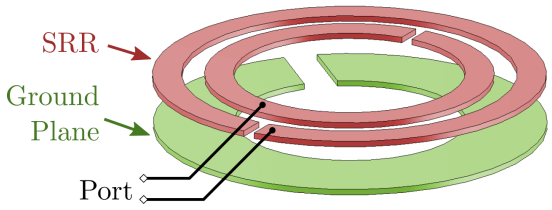

Figure 5.8: Drawing of a split-ring resonator with ground plane. The substrate between the SRR and the ground is omitted.

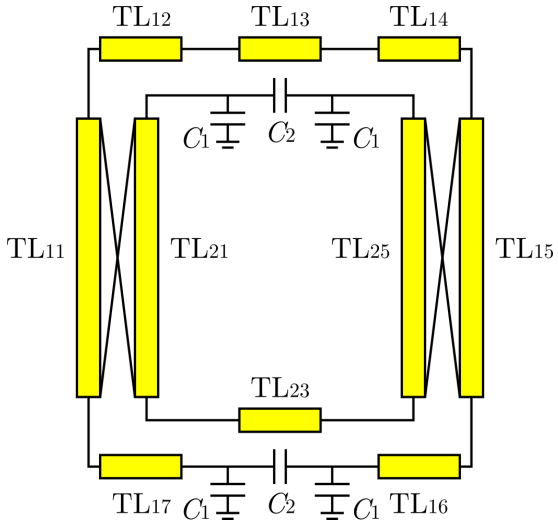

Figure 5.9: Model representation of a SRR with ground plane as in [16].

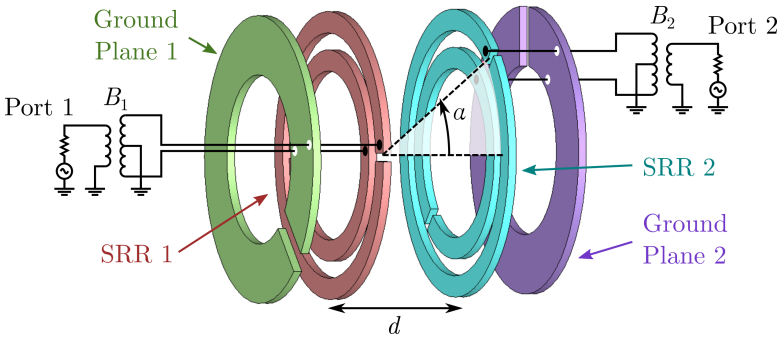

Figure 5.10: Final stack up of the SRR link. Two separate substrates are considered: each SRR belongs to the substrate of the corresponding ground plane. The distance d represents the clearance between the facing SRRs, whereas the angle α is the relative angular position of the outer strips slots positions.

Coupled SRRs

A UHF near-field link can then be efficiently realized by exploiting two faced SRRs, whose geometries are fine-tuned by EM simulations with respect to the single SRR design, to realize a resonant link at 868 MHz. A rendering of the final link arrangement is shown in Fig. 5.10 where the distance d represents the clearance between the facing SRRs, whereas the angle α is the relative angular position of the outer strips slots positions. The differential input and output ports of the SRR-based link are connected to the respective unbalanced feeding circuits by means of two identical baluns, B_1 and B_2. Each side of the near-field link, composed by the SRR and its own ground plane is free to rotate with respect to the other. As explained in the next section, this can be used to finely tune the resonance frequency. The fine tuning of the SRRs-based link is carried out by means of EM simulators, with the starting-point layout derived from the equivalent ciruit model of Fig.5.9. The final EM-derived circuit model of Fig.5.10 is then analysed at the circuit level and its port parameters are compared with the experimental measurements.

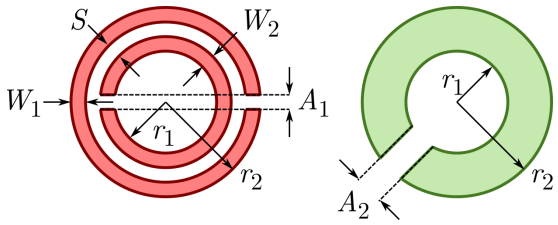

Figure 5.11: Geometric definitions of the manufactured SRRs.

5.2.2 Experimental Setup

Some prototypes of SRRs have been manufactured. The geometrical specification of the design are given in Fig. 5.11 and Table 5.3. The outer diameter of the board is determined by the available radial space in the ferrite core cavity of Fig. 5.1, whereas the width of the microstrips has been numerically optimised starting from the circuit-equivalent capacitive link model. The adopted substrate is an FR4 Panasonic 4-layer R1566/R1551 substrate ($\varepsilon_r = 5.0$, $\tan\delta = 0.015$). Two sets of measurements have been carried out: the first one was devoted to validate the single SRR in the band of interest; the second one is dedicated to the frequency behaviour of the two faced coupled SRRs, realizing the RF near-field data link.

5.2.3 Single SRR

The stand-alone SRR has been characterized by means of measurements, numerical simulations, and model simulations in the frequency band of interest. In Fig. 5.12, a picture of the multi-layer manufactured resonator used for the reflection coefficient measurement is shown: on the left, the top copper metallization-strips are visible; the ground plane is realized as an inner layer, whereas the integrated balun and the SMA connector are soldered on the bottom copper shown on the right side of the picture. The selected balun is model 0900BL18B100 manufactured

Table 5.3: SRR geometric dimensions.

Symbol	Description	Value	Units
S	Spacing between rings	2	mm
W_1	Inner ring width	2.5	mm
W_2	Outer ring width	2.5	mm
r_1	Inner ring inner radius	10	mm
r_2	Outer ring outer radius	17	mm
A_1	Ring slot width	1	mm
A_2	Ground plane slot width	3	mm
t	Substrate thickness (metal to ground)	1.118	mm
d	Clearance between faced SRRs	0.6	mm
θ	Relative angle between faced SRRs	45	°

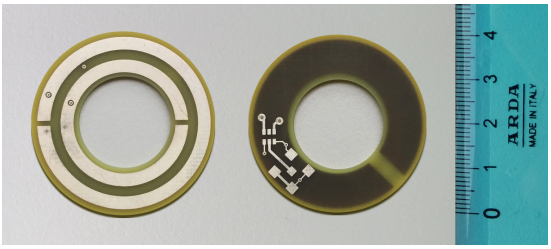

Figure 5.12: Picture of the first SRR prototype. On the right, the bottom layer is shown; the ground plane is visible as a dark inner layer.

by Johanson Technology.

In Fig. 5.13, the results of the SRR reflectivity comparison are shown. The CST software has been used to compute the numerical simulation of the model, and Keysight ADS has been adopted to implement its microstrip equivalent circuit representation of Fig. 5.9. There is an excellent agreement between the measured and the simulated results in the considered frequency band, especially with the microstrip model. The single SRR structure does not show any resonant behaviour below 1 GHz. The reflectivity trend, visible in the rightmost part of the plot,

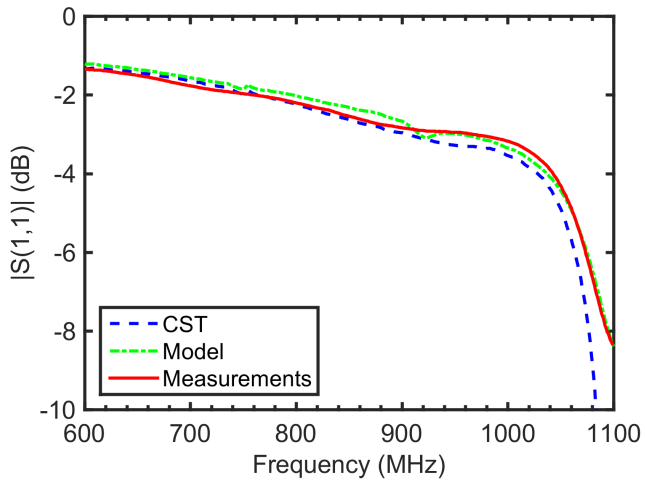

Figure 5.13: Comparison of the port reflectivity of a single SRR as in Fig. 5.8 (CST numerical results, electrical model simulation, measurements).

however, suggests that it may resonate close to 1.1 GHz, in any case outside the considered frequency band.

5.2.4 Reactive link based on two faced SRRs

The choice of employing faced SRRs has a major drawback with respect to capacitive plates: the link loses its axial symmetry, which was particularly useful in rotary applications such as slip ring replacement. Nonetheless, for those applications addressed in this work and related to industrial automatic machines, this does not represent a criticism of the proposed system, since the angular speed of the rotary side (300 rpm) is many orders of magnitude slower than the data readout rate at UHF (at least 1000 times the average time for data readout, more than 170000 times the UHF signal period). Thus, for the purpose of data communications, the rotating side can been assumed in static conditions and the best angular position of the SRRs can be used. Indeed, the on-board machine encoders can provide this information to activate the sensor reading in the proper time-slot, as explained at the end of this section.

An assembly composed by two stacked facing SRRs has been ar-

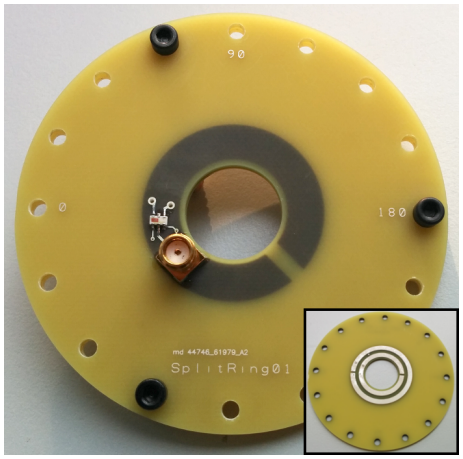

Figure 5.14: Picture of the two stacked SRR prototypes. The drilled holes allow to test different angular orientations. In the inset, a faced layer is shown.

ranged, as shown in Fig. 5.14. The drilled holes allow to test different relative angular positions of the two faced SRR boards. The clearance d between the SRRs, as indicated in Table 5.3, is ensured by three shims in correspondence with the screws that tighten the prototypes together. As also reported in Table 5.3, given a 0.6-mm clearance, a relative rotation of 45 degrees represents the optimal choice to maximize the transfer coefficient of the link. Finally, the same balun of the single SRR setup has been used for the two boards.

The comparison between CST simulations and measurements is shown in Fig. 5.15 and Fig. 5.16 for the link ports reflection and transmission coefficients, respectively. The exact resonance frequency is 867 MHz, although in the frequency range between 864 MHz and 883 MHz the link insertion loss remains approximately constant and equal to 4 dB.

Different arrangements can be tested. In particular, in Fig. 5.17, the measured plots of the amplitude of the link transmission coefficient for different angular positions are shown. As can be seen, deviations greater than 20° from the nominal relative angle α can be exploited to tune the resonance frequency within a certain range of extent. Above

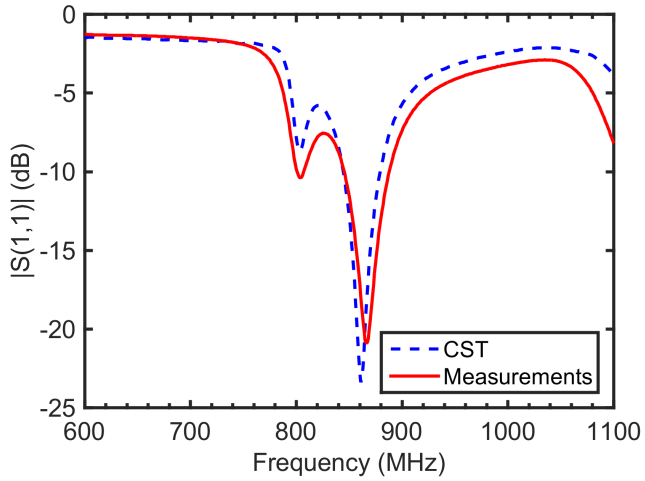

Figure 5.15: Comparison of the reflection coefficient at the port 1 of two faced SRRs as in Fig. 5.10 (CST numerical results, measurements).

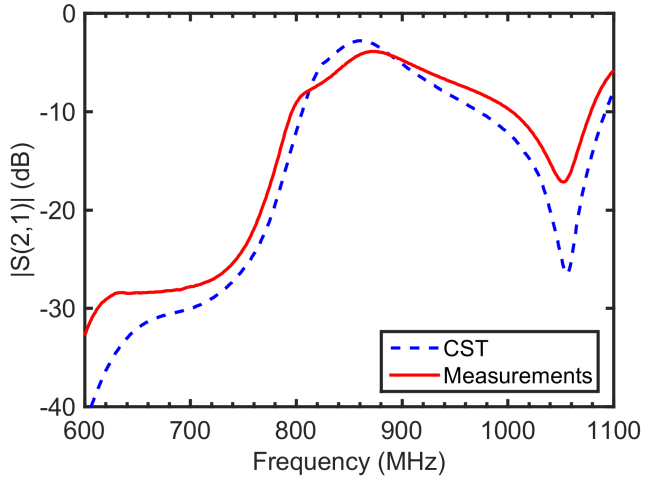

Figure 5.16: Comparison of the transmission coefficient of two faced SRRs as in Fig. 5.10 (CST numerical results, measurements).

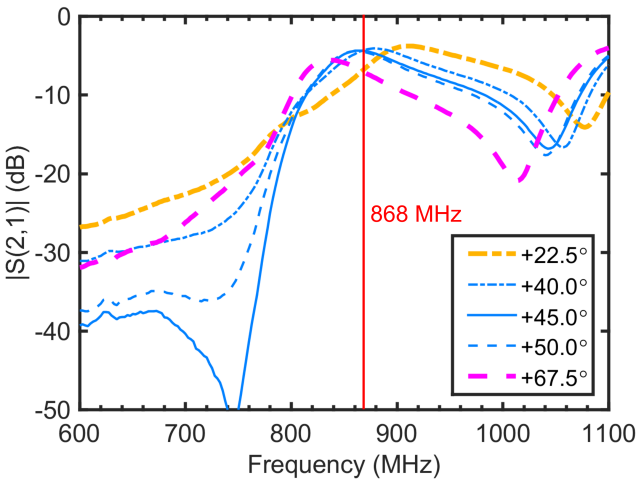

Figure 5.17: Comparison of the measured transmission coefficients of two faced SRRs as in Fig. 5.10 for different angular positions.

all, it has to be noticed that, within an angle interval of 10° around the 45° reference, the same link performance are obtained. In this interval, the remote temperature measurements are not affected by any link performance variations. This ensures a safe accuracy of temperature measurement during the receiver rotation.

This is also confirmed by the plots of Fig. 5.18 where the split ring angular position and the corresponding link transmission coefficient variation versus time are compared. The average time to complete the temperature sensing operation, which is mainly determined by the A/D conversion time, is also superimposed on the same plot. These results clearly confirm that a safe operational area is largely guaranteed.

5.2.5 Experimental System Results

The described UHF near-field link has been included in the design of a passive sensing system. The circuit-equivalent schematic of the whole system is reported in Fig. 5.19. The component values adopted in the circuit simulation are reported in Table 5.4. As per the reactive link, its measured frequency-dependent S-parameters are used. The sub-circuit

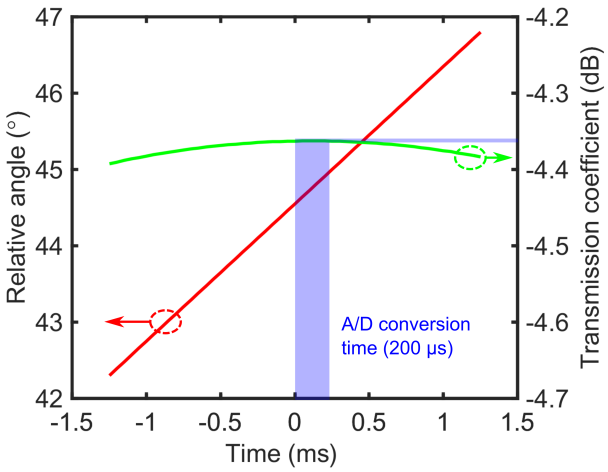

Figure 5.18: Relationship between the time required for temperature conversion and the rotation of the remote split ring.

loading the link receiver side consists of (from right to left): the temperature probe R_{RTD}, the rectifier ($D_{1,2}$, $C_{D1,D2}$), and the (mis)matching network C_m, L_m, which is the same as in Fig. 3.6. The near-field link representation is also included: namely the coupled SRRs (SRR_1, SRR_2), the two baluns (B_1, B_2), and the matching networks ($C_{1,2}$, $L_{1,2}$). It is noteworthy that the two capacitances C_2 and C_m are kept separated in the circuit representation for the sake of clarity. The hybrid (H_1) coupled ports (1,2) and (3,4) allow the incident RF power to be transferred from the RF source to the receiver and the RF power reflected by the receiver loading circuit to the power detector U_1. A conventional matching network C_U, L_U and a dc-block capacitor C_C are used to join the power detector to the hybrid coupler.

The sensing system is intended to detect temperature variations in the range $[0, 323]$ °C. The corresponding range of variation of the RTD is $[1, 2.2]$ kΩ. The matching networks ($C_{1,2}$, $L_{1,2}$) realize the simultaneous conjugate matching of the link, including the baluns, as required by (7). The input power P_{av} and the mismatching network C_m, L_m (see Fig. 5.19) have been simultaneously optimised, as anticipated in Section II.B,

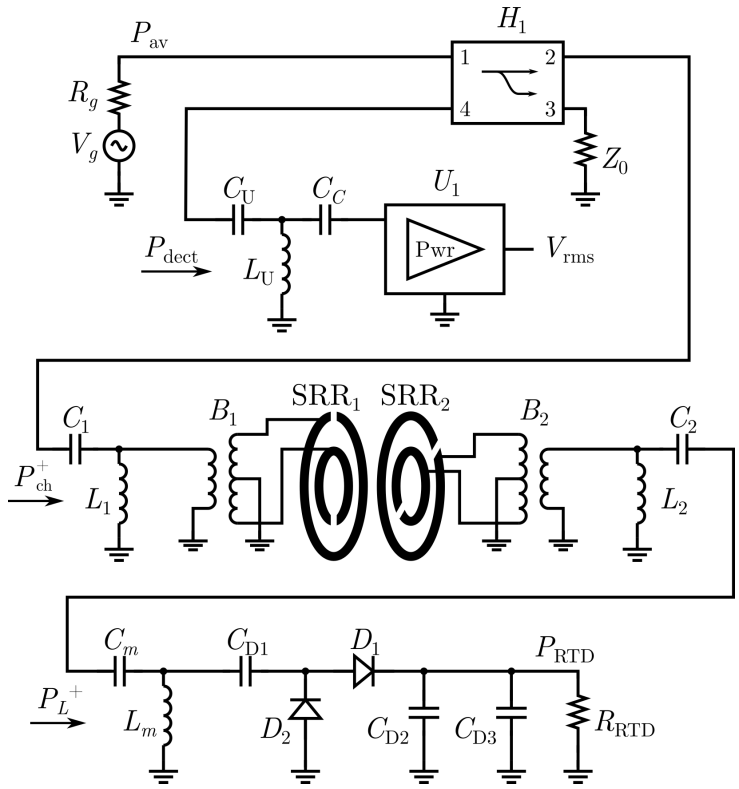

Figure 5.19: Circuit-equivalent schematic of the entire wireless UHF passive sensing system.

Table 5.4: System component values

Symbol	Value	Units
P_{av}	10	dBm
H_1	C0810J503AHF	
U_1	AD8361	
C_U	2.4	pF
L_U	12	nH
C_C	100	pF
Z_0	50	Ω
L_1, L_2	22	nH
C_1, C_2	5.6	pF
T_1, T_2	0900BL18B100	
X_1, X_2	SRRs as in Table 5.3	
C_m	47	pF
L_m	100	nH
C_{D1}, C_{D2}	22	pF
D_1, D_2	BAT15-03W	
C_{D3}	10	nF
R_{RTD}	$[1000, 2200]$	Ω

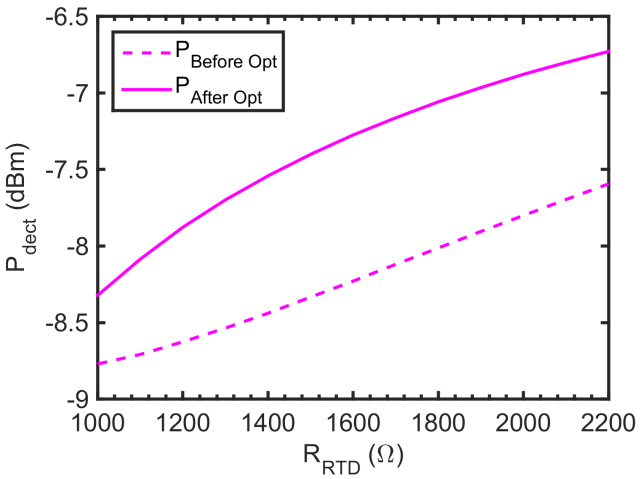

Figure 5.20: Power range at the detector input port before and after optimisation of the input power and of the mismatching network of the system receiving side.

in order maximize the reflected power variation at the receiver port. The quasi-Newton algorithm has been adopted for the circuit optimisation. In Fig. 5.20, the result of the optimisation in terms of the power reflected at the transmitter side, and available at the detector input port, all over the system load, is shown: a 0.51 dB increase of in the reflected power dynamics is observed. Constrained optimisation was carried out within the following intervals: $P_{\text{av}} = [-10, 10]$ dBm, $C_m = [1\,\text{p}, 100\,\text{n}]$ F, $L_m = [1, 100]$ nF; starting values: $P_{\text{av}} = 0\,\text{dBm}, C_m = 1.5\,\text{nF}, L_m = 15\,\text{nF}$, according to load impedance resulting from (3.7).

By supplying the system with $P_{\text{av}} = 10$ dBm, the rectifier is ensured to receive roughly $[-2.5, -0.5]$ dBm, depending on the load value. This optimised power level ensures the lowest reduction in the load reflection coefficient dynamics due to the nonlinear network, as discussed in Section 2.2. Circuital simulation results based on the manufacturers' models of employed components are hereinafter presented. The required transmitted power is relatively high, but since the system has no restrictions on power availability at the transmitter side [69], this is not an issue. On

the contrary, its first requirement is to be able to track the temperature at the far-end location of the sensor, where it is preferable not to locate further circuits for sensor read-out, due to high temperatures.

In Fig. 5.21, the different power levels predicted and measured at selected subsystem interconnecting ports are compared and plotted versus the link dc load: P_{RTD} represents the dc power on the RTD, P_L^+ the power delivered to the load, which includes the rectifier, and P_{dect} the power detector input power. Since H_1 is a hybrid coupler, P_{dect} equals half of the reflected power by the link (P_{ch}, not shown in Fig. 5.19). The selected power detector is the AD8361 manufactured by Analog Devices. The resulting power variation at the detector input port spans between -6.44 and -5.26 dBm. The analog processing of the AD8361 converts this power range to dc voltage varying between 1.47 and 1.69 V, respectively. In Fig. 5.22, the measured relationship between the temperature and the dc voltage level is finally shown and compared to the simulated results. The relationship between temperature and system dc load is implicitly defined, thanks to the extremely good linearity of the RTDs [118]. The resulting V_{rms} vs Temperature curve exhibits a moderate, but expected, nonlinear behaviour due to the rectifier. The corresponding voltage range detected is 212 mV for temperature variations between 0 and 323 °C, and 203 mV between 0 and 300 °C. The resulting average sensitivity is 0.66 mV / °C. For completeness, in Fig. 5.23 the end-to-end link efficiency is shown; the plotted quantity is obtained by measuring the power on the RTD load, whose maximisation is not—on purpose—a goal of this work.

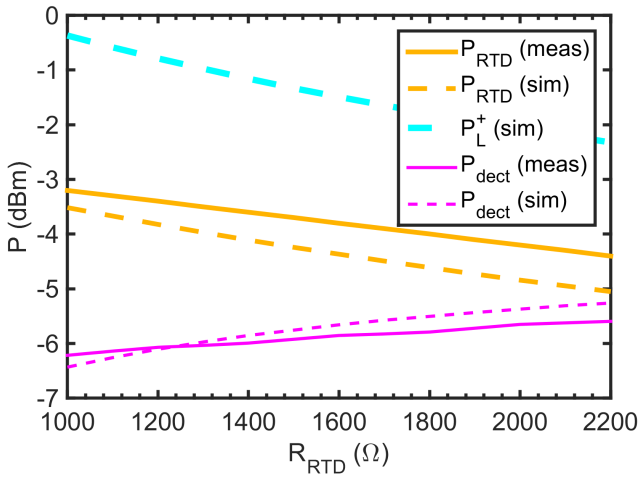

Figure 5.21: Measured and predicted power levels versus the resistive dc load (RTD) with reference to subscripts of Fig. 5.19. P_L^+ cannot be measured (no available test points); simulated result is shown.

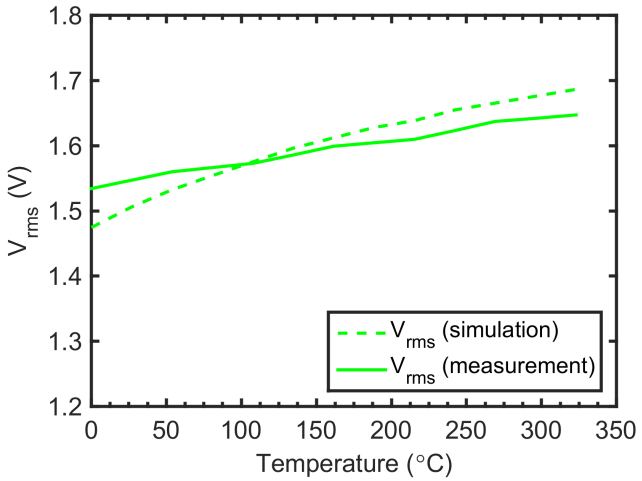

Figure 5.22: Measured and predicted relationship between the sensed temperature and the power detector output voltage.

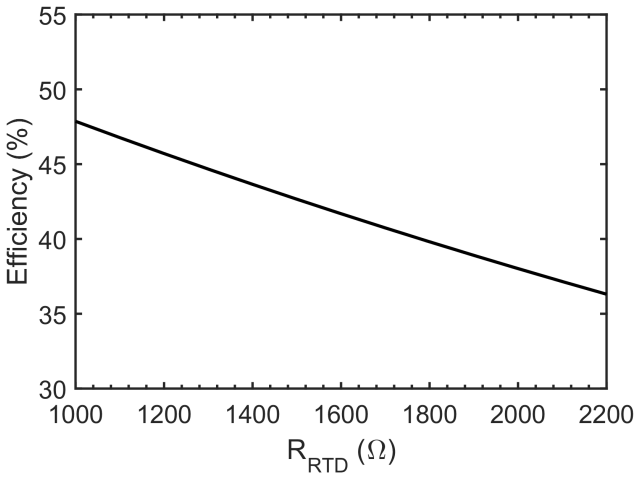

Figure 5.23: End-to-end link efficiency measured on the RTD load.

5.2.6 Remarks

The experiments demonstrates how to solve the drawback of the previous setup, explained at the end of Section 5.1. The adoption of self-resonant structures, realized by SRRs in a higher frequency band, allows to increase accuracy and repeatability of measures, while complying with the same geometry constraints for simultaneous power and data transfer.

Conclusions

The adventure through the disclosure of Tesla's legacy revealed to be rich of fascinating discoveries to be shared among the scientific community. The industrial interest in experimenting WPT solutions made the work even more challenging. By shortly recalling the topics of this thesis, a deep discussion on the actual performances and challenges of the CET system design was presented; state-of-the-art power converters, specifically designed for WPT, were introduced, and the topologies briefly compared; a passive solution based on the RFID technology for the remote monitoring of industrial sensors was proposed and analytically discussed; finally, several industrial applications implementing industrial CET and WPIT were analysed and the experimental results explained.

From the CET analysis of Chapter 1, it turns out that different design rules, with respect to traditional low-power WPT solutions, should be taken into account. For example, the capacitive compensation may be difficult to be implemented, due to high voltage levels on capacitors. Thus, because of the tiny disadvantage in terms of efficiency for highly coupled systems, a non-resonant design of the CET device can be considered. On the contrary, power losses represent a major issue on CET units, because of the resulting increase in the device temperature, rather than source-to-load efficiency concerns. Seeking optimal trade-off between winding losses and core losses is essential in order to

ensure best CET performance and reliability over time. This, however, requires a fine-tuning of several design parameters, such as core geometries, wire choice, frequency, and number of turns. Power sources may also be responsible for a considerable amount of power loss. Guidelines for choosing the optimal power converter topology according to application requirements were also provided in Chapter 2; in any case, soft switching of active devices must be ensured to maximise the power conversion efficiency and minimise EMI. An application that combines a CET unit with a resonant power converter is presented in Chapter 4: results prove that EMI concerns are sometimes in contrast with strict requirements on power losses and an optimal trade-off should be identified.

The scope of CET systems, however, is not limited to power transfer applications. In many cases, one or more feedback signals are required to be sent back from the moving load to the controlling/supplying unit (Chapter 3). Therefore, a combined wireless power and information transfer problem arise. Two completely passive solutions were proposed in Chapter 5: first, a combination of capacitive and inductive couplings for wireless data and power, respectively; second, a UHF near-field sensing system along with the traditional IPT. In both cases, a smart exploitation of the nonlinear dc-power to dc-load relationship of a standard RFID rectifier is adopted to convert the data of a remote temperature sensor, representing the system variable load. The UHF-based solution resulted to be a better solution in terms of sensitivity and accuracy, thanks to the SRR self-resonant structure that replaces both the capacitive plates and the external resonator of the former solution.

Throughout the thesis, design procedures were proposed and combination of technologies tested out. For a few possible industrial applications, prototypes were also built and validated. These represented an

inconvertible proof that WPT became mature to be adopted not only by consuming electronics, but in factories as well, where the integration of wireless power, radio signals, and design flexibility must be ensured. At the end, the *transmission of electrical energy without wires* is far from being considered over.

Acknowledgements

Foremost, I would like to express my sincere gratitude to my advisor Prof. Alessandra Costanzo who drove me through the steps toward my doctoral graduation, and Ing. Dario Rea, head of the Innovation division in IMA, who led my research activities toward solutions of industrial applicability. A kindly cooperation between academia and industry has grown during the PhD. Thanks to their will, I have been hired in IMA as full-time electronic designer in the R&D department, and the collaboration with the University of Bologna has been renewed after my PhD.

I am extremely indebted to Prof. Salmon Cinotti, who proposed me the opportunity of an industrial PhD with IMA and introduced me to Ing. Dario Rea and Roberto Romagnoli during an assessment meeting back in July 2012. Without their intention and utmost encouragement all of this would not have been possible.

I gratefully acknowledge Roberto Romagnoli, my former supervisor at IMA, for the detailed description of automatic machines and for the explanations on the packaging industry. I am grateful to Dr. Massimo Balma, my actual supervisor and mentor, for the insightful comments and the scientific knowledge shared with me during the late months of doctoral apprenticeship.

I would like to extend my thanks to all the people who assisted me in IMA. Especially, Daniele Libanori and Massimo Pieni for their technical

abilities and the time they spent with me in designing, manufacturing, and testing experimental prototypes in Ozzano and abroad.

I am also grateful to Dr. Diego Masotti, Prof. Franco Mastri, Alex Pacini, Massimo Del Prete and the rest of the UniBo EM Lab team that supported me during the research activities in Bologna and during the conferences abroad.

I would also like to express my gratitude to the reviewers of my thesis, Prof. Nuno Borges Carvalho (University of Aveiro, Portugal), Prof. Mauro Mongiardo (University of Perugia, Italy), and Prof. Peter Russer (Technical University of Munich, Germany), who provided deep insights and useful remarks.

Lastly, but not less important, I wish to express my heartfelt thanks to my family, Sonia and Daniele. They encouraged and supported me all through the academic path and during the doctoral apprenticeship in IMA.

List of Achievements

Publications

- R. Trevisan and A. Costanzo, "A 1-kW wireless power transfer link for welding rollers," in *Proc. PIERS 2013 Stockholm*, (Stockholm, Sweden), pp. 1566–1570, Aug. 2013.

- R. Trevisan and A. Costanzo, "A 1-kW contactless energy transfer system based on a rotary transformer for sealing rollers," *IEEE Trans. Ind. Electron.*, vol. 61, pp. 6337–6345, Nov. 2014.

- R. Trevisan and A. Costanzo, "State-of-the-art of contactless energy transfer (CET) systems: design rules and applications," *Wireless Power Transfer*, Cambridge Journals Online, 2014, no. 1, pp. 10–20.

- R. Trevisan and A. Costanzo, "Exploitation of passive RFID technology for wireless read-out of temperature sensors," in *Proc. 2014 IEEE RFID Technology and Applications Conf.*, (Tampere, Finland), pp. 150–154, Sept. 2014.

- R. Trevisan and A. Costanzo, "Wireless sensing and power transfer in a rotary tool," in *Proc. 2015 IEEE MTT-S Int. Microwave Symp.*, (Phoenix, AZ), pp. 1–4, May 2015.

- R. Trevisan and A. Costanzo, "Exploitation of capacitive coupling at UHF for remote sensing in a kW WPT system," in *Proc. 2015 IEEE European Microwave Conference*, (Paris, France), pp. 490–493, Sept. 2015.

Accepted Journal Papers

- R. Trevisan and A. Costanzo, "A UHF Near-field Link for Passive Sensing in Industrial Wireless Power Transfer Systems," submitted to *IEEE Trans. Microw. Theory Tech.*, Nov. 2015, accepted for publication.

Accepted Conference Papers

- A. Pacini, F. Mastri, R. Trevisan, A. Costanzo, and D. Masotti, "Theoretical and experimental characterization of moving wireless power transfer systems," *2016 10th European Conf. on Antennas and Propagation*, (Davos, Switzerland), Apr. 2016, accepted for publication.

- A. Pacini, F. Mastri, R. Trevisan, A. Costanzo, and D. Masotti, "Geometry optimization of sliding inductive links for position-independent wireless power transfer," *2016 IEEE MTT-S Int. Microwave Symp.*, (San Francisco, CA), May 2016, accepted for publication.

Invited Talks

- R. Trevisan and A. Costanzo, "Contactless kW power transfer for industrial machines," in *2015 IEEE European Microwave Week*, (Rome, Italy), Oct. 2014.

- R. Trevisan and A. Costanzo, "Circuit-level design of systems integrating wireless power transfer and sensors read-out," in *2015 IEEE MTT-S Int. Microwave Symp.*, (Phoenix, AZ), May 2015.

- R. Trevisan and A. Costanzo, "Circuit level design of wireless systems for simultaneous data and power transfer," in *2016 IEEE MTT-S Int. Microwave Symp.*, (San Francisco, CA), May 2016.

Patents

- A. Costanzo, R. Trevisan, and D. Rea, "Working unit equipped with a device for contactless electricity transfer and method for contactless electricity transfer in a working unit," Int. Patent Application WO 2015/177759 A1, filing date 22 May 2015.

.

Bibliography

[1] M. P. Kazmierkowski and A. J. Moradewicz, "Unplugged but connected: review of contactless energy transfer systems," *IEEE Ind. Electron. Mag.*, vol. 6, no. 4, pp. 47–55, 2012.

[2] A. Esser and H.-C. Skudelny, "A new approach to power supplies for robots," *IEEE Trans. Ind. Appl.*, vol. 27, no. 5, pp. 872–875, 1991.

[3] K. Klontz, D. Divan, D. Novotny, and R. Lorenz, "Contactless power delivery system for mining applications," *IEEE Trans. Ind. Appl.*, vol. 31, pp. 27–35, Jan 1995.

[4] C.-s. Wang, O. H. Stielau, and G. A. Covic, "Design considerations for a contactless electric vehicle battery charger," *IEEE Trans. Ind. Electron.*, vol. 52, no. 5, pp. 1308–1314, 2005.

[5] J. A. Russer, M. Dionigi, M. Mongiardo, and P. Russer, "A moving field inductive power transfer system for electric vehicles," in *Proc. 2013 IEEE 43rd European Microwave Conf.*, (Nuremberg, Germany), pp. 519–522, 2013.

[6] V. Rizzoli, A. Costanzo, D. Masotti, and F. Donzelli, "Integration of numerical and field-theoretical techniques in the design of single-

and multi-band rectennas for micro-power generation," *Int. J. Microwave and Wireless Technologies*, vol. 2, pp. 293–303, 8 2010.

[7] A. Costanzo, A. Romani, D. Masotti, N. Arbizzani, and V. Rizzoli, "RF/baseband co-design of switching receivers for multiband microwave energy harvesting," *Sensors and Actuators A: Physical*, vol. 179, no. 1, pp. 158–168, 2012.

[8] T. Ohira, "Via-wheel power transfer to vehicles in motion," in *Proc. 2013 IEEE Wireless Power Transfer Conf.*, (Perugia, Italy), pp. 242–246, 2013.

[9] J. Hirai, T.-w. Kim, and A. Kawamura, "Wireless transmission of power and information and information for cableless linear motor drive," *IEEE Trans. Power Electron.*, vol. 15, no. 1, pp. 21–27, 2000.

[10] M. Reinhard, C. Spindler, T. Schuer, V. Birk, and J. Denk, "New approaches for contactless power transmission systems integrated in PM motor drives transferring electrical energy to rotating loads," in *Proc. 2011 IEEE 14th European Conf. Power Electronics and Applications*, (Birmingham, UK), pp. 1–10, 2011.

[11] A. Sample, B. Waters, S. Wisdom, and J. Smith, "Enabling seamless wireless power delivery in dynamic environments," *IEEE Proc.*, vol. 101, no. 6, pp. 1343–1358, 2013.

[12] M. Budhia, G. Covic, and J. Boys, "Design and optimization of circular magnetic structures for lumped inductive power transfer systems," *IEEE Trans. Power Electron.*, vol. 26, no. 11, pp. 3096–3108, 2011.

[13] G. Covic and J. Boys, "Inductive power transfer," *Proc. IEEE*, vol. 101, no. 6, pp. 1276–1289, 2013.

[14] S. Weinberger, "Preliminary design development of 100 kW rotary power transfer device," tech. rep., NASA, 1982.

[15] K. Papastergiou, D. Macpherson, and F. Fisher, "A 1kW phase-shifted full bridge converter incorporating contact-less transfer of energy," in *Proc. 2005 Power Electronics Specialists Conf.*, (Recife, Brazil), pp. 83–89, 2005.

[16] A. J. Moradewicz and M. P. Kazmierkowski, "Contactless Energy Transfer System With FPGA-Controlled Resonant Converter," *IEEE Trans. Ind. Electron.*, vol. 57, no. 9, pp. 3181–3190, 2010.

[17] D. Pedder, A. Brown, and J. Skinner, "A contactless electrical energy transmission system," *IEEE Trans. Ind. Electron.*, vol. 46, no. 1, pp. 23–30, 1999.

[18] K. D. Papastergiou and D. E. Macpherson, "An airborne radar power supply with contactless transfer of energy–Part I: rotating transformer," *IEEE Trans. Ind. Electron.*, vol. 54, no. 5, pp. 2874–2884, 2007.

[19] S. Valtchev, B. Borges, K. Brandisky, and J. B. Klaassens, "Resonant contactless energy transfer with improved efficiency," *IEEE Trans. Power Electron.*, vol. 24, no. 3, pp. 685–699, 2009.

[20] J. Smeets, T. Overboom, J. Jansen, and E. Lomonova, "Comparison of position-independent contactless energy transfer systems," *IEEE Trans. Power Electron.*, vol. 28, no. 4, pp. 2059–2067, 2013.

[21] J. Sibue, G. Kwimang, J.-p. Ferrieux, and G. Meunier, "A Global Study of a Contactless Energy Transfer System: Analytical Design,

Virtual Prototyping and Experimental Validation," *IEEE Trans. Power Electron.*, vol. 28, no. 10, pp. 4690–4699, 2013.

[22] R. Trevisan and A. Costanzo, "State-of-the-art of contactless energy transfer (CET) systems: design rules and applications," *Wireless Power Transfer*, vol. 1, pp. 10–20, 3 2014.

[23] K. D. Papastergiou and D. E. Macpherson, "An airborne radar power supply with contactless transfer of energy–Part II: converter design," *IEEE Trans. Ind. Electron.*, vol. 54, no. 5, pp. 2885–2893, 2007.

[24] G. Marrocco, "Pervasive electromagnetics: sensing paradigms by passive RFID technology," *IEEE Wireless Commun.*, vol. 17, pp. 10–17, December 2010.

[25] A. Sample, D. Yeager, P. Powledge, A. Mamishev, and J. Smith, "Design of an RFID-based battery-free programmable sensing platform," *IEEE Trans. Instrum. Meas.*, vol. 57, pp. 2608–2615, Nov 2008.

[26] S. Capdevila, L. Jofre, J. Romeu, and J.-C. Bolomey, "Passive RFID based sensing," in *Proc. 2011 IEEE Int. Conf. RFID-Technologies and Applications*, (Sitges, Spain), pp. 507–512, Sept 2011.

[27] J. Dowling, M. Tentzeris, and N. Beckett, "RFID-enabled temperature sensing devices: A major step forward for energy efficiency in home and industrial applications?," in *Proc. 2009 IEEE MTT-S Int. Microwave Workshop Wireless Sensing, Local Positioning, and RFID*, (Catvat, Croatia), pp. 1–4, Sept 2009.

[28] A. Esser, "Contactless charging and communication for electric vehicles," *IEEE Ind. Appl. Mag.*, vol. 1, pp. 4–11, Nov 1995.

[29] M. Theodoridis, "Effective capacitive power transfer," *IEEE Trans. Power Electron.*, vol. 27, no. 12, pp. 4906–4913, 2012.

[30] M. Yang, Y. Wang, X. Zhang, and J. Li, "Analysis of reflected load model for inductively coupled power transfer systems," in *Proc. 2010 IEEE Asia-Pacific Power and Energy Engineering Conf.*, (Wuhan, China), pp. 1–4, 2010.

[31] A. Sample, D. Meyer, and J. Smith, "Analysis, experimental results, and range adaptation of magnetically coupled resonators for wireless power transfer," *IEEE Trans. Ind. Electron.*, vol. 58, no. 2, pp. 544–554, 2011.

[32] J. A. Russer, P. Russer, M. Mongiardo, and M. Dionigi, "A bidirectional wireless power transfer system for roadway powered electric vehicles," *Microwave Review*, vol. 19, no. 2, pp. 68–75, 2013.

[33] W. Zhang, S.-C. Wong, C. Tse, and Q. Chen, "Analysis and comparison of secondary series- and parallel-compensated inductive power transfer systems operating for optimal efficiency and load-independent voltage-transfer ratio," *IEEE Trans. Power Electron.*, vol. 29, pp. 2979–2990, June 2014.

[34] A. Costanzo, M. Dionigi, F. Mastri, M. Mongiardo, J. A. Russer, and P. Russer, "Design of magnetic-resonant wireless power transfer links realized with two coils: comparison of solutions," *Int. J. Microwave and Wireless Technologies*, vol. 7, pp. 349–359, June 2015.

[35] C.-J. Chen, T.-H. Chu, C.-L. Lin, and Z.-C. Jou, "A study of loosely coupled coils for wireless power transfer," *IEEE Trans. Circuits Syst. II*, vol. 57, no. 7, pp. 536–540, 2010.

[36] C.-S. Wang, G. A. Covic, and O. H. Stielau, "Power transfer capability and bifurcation phenomena of loosely coupled inductive power transfer systems," *IEEE Trans. Ind. Electron.*, vol. 51, no. 1, pp. 148–157, 2004.

[37] M. Kiani and M. Ghovanloo, "A figure-of-merit for designing high-performance inductive power transmission links," *IEEE Trans. Ind. Electron.*, vol. 60, no. 11, pp. 5292–5305, 2013.

[38] M. Pinuela, D. Yates, S. Lucyszyn, and P. Mitcheson, "Maximizing DC-to-load efficiency for inductive power transfer," *IEEE Trans. Power Electron.*, vol. 28, no. 5, pp. 2437–2447, 2013.

[39] Z. N. Low, R. Chinga, R. Tseng, and J. Lin, "Design and test of a high-power high-efficiency loosely coupled planar wireless power transfer system," *IEEE Trans. Ind. Electron.*, vol. 56, no. 5, pp. 1801–1812, 2009.

[40] M. Dionigi, M. Mongiardo, and R. Perfetti, "Rigorous network and full-wave electromagnetic modeling of wireless power transfer links," *IEEE Trans. Microw. Theory Techn.*, vol. 63, pp. 65–75, Jan 2015.

[41] B. H. Waters, A. P. Sample, and J. R. Smith, "Adaptive impedance matching for magnetically coupled resonators," in *Proc. Progress In Electromagnetics Research Symp. 2012 in Moscow*, (Moscow, Russia), pp. 694–701, August 2012.

[42] D. Ahn and S. Hong, "A transmitter or a receiver consisting of two strongly coupled resonators for enhanced resonant coupling in wireless power transfer," *IEEE Trans. Ind. Electron.*, vol. 61, no. 3, pp. 1193–1203, 2014.

[43] A. Esser and A. Nagel, "Contactless high speed signal transmission integrated in a compact rotatable power transformer," in *Proc. 1993 IEEE 5th European Conf. Power Electronics and Applications*, (Brighton, UK), pp. 409–414 vol.4, 1993.

[44] J. Lastowiecki and P. Staszewski, "Sliding transformer with long magnetic circuit for contactless electrical energy delivery to mobile receivers," *IEEE Trans. Ind. Electron.*, vol. 53, no. 6, pp. 1943–1948, 2006.

[45] J. Smeets, D. Krop, J. Jansen, and E. Lomonova, "Contactless power transfer to a rotating disk," in *Proc. 2010 IEEE Int. Symp. Industrial Electronics*, (Bari, Italy), pp. 748–753, 2010.

[46] T. Gerrits, D. C. J. Krop, L. Encica, and E. A. Lomonova, "Development of a linear position independent inductive energy transfer system," in *Proc. 2011 IEEE Int. Electric Machines & Drives Conf.*, (Niagara Falls, ON), pp. 1445–1449, 2011.

[47] A. Costanzo, M. Dionigi, F. Mastri, M. Mongiardo, J. A. Russer, and P. Russer, "Rigorous network modeling of magnetic-resonant wireless power transfer," *Wireless Power Transfer*, vol. 1, pp. 27–34, 3 2014.

[48] D. Kurschner, C. Rathge, and U. Jumar, "Design methodology for high efficient inductive power transfer systems with high coil

positioning flexibility," *IEEE Trans. Ind. Electron.*, vol. 60, no. 1, pp. 372–381, 2013.

[49] R. Mecke and C. Rathge, "High frequency resonant inverter for contactless energy transmission over large air gap," in *Proc. 2004 IEEE 35th Annu. Power Electronics Specialists Conf*, vol. 3, (Aachen, Germany), pp. 1737–1743, 2004.

[50] R. Trevisan and A. Costanzo, "A 1-kW wireless power transfer link for welding rollers," in *Proc. PIERS 2013 Stockholm*, (Stockholm, Sweden), pp. 1566–1570, 2013.

[51] A. Lotfi and F. Lee, "A high frequency model for litz wire for switch-mode magnetics," in *Conf. Rec. 1993 IEEE Industry Applications Society Annu. Meeting*, (Toronto, ON), pp. 1169–1175 vol.2, 1993.

[52] P. Dowell, "Effects of eddy currents in transformer windings," *Proc. of the Inst. of Elect. Eng.*, vol. 113, no. 8, pp. 1387–1394, 1966.

[53] J. A. Ferreira, "Improved analytical modeling of conductive losses in magnetic components," *IEEE Trans. Power Electron.*, vol. 9, no. 1, pp. 127–131, 1994.

[54] C. R. Sullivan, "Optimal choice for number of strands in a litz-wire transformer winding," *IEEE Trans. Power Electron.*, vol. 14, no. 2, pp. 283–291, 1999.

[55] J. Smeets, D. Krop, J. Jansen, M. Hendrix, and E. Lomonova, "Optimal design of a pot core rotating transformer," in *Proc. 2010 IEEE Energy Conversion Congr. and Expo.*, (Atlanta, GA), pp. 4390–4397, 2010.

[56] C. P. Steinmetz, "On the law of hysteresis," *Proc. IEEE*, vol. 72, no. 2, pp. 197–221, 1984.

[57] F. van Horck, *A Treatise on Magnetics and Power Electronics*. Eindhoven, The Netherlands: Eindhoven Univ. Technol., 2010.

[58] N. Mohan, T. M. Undeland, and W. P. Robbins, *Power Electronics: Converters, Applications, and Design*. Hoboken, NJ: Wiley, 3 ed., 2003.

[59] Ferroxcube, *Soft ferrite and accessories 2009 data handbook*. The Netherlands: Ferroxcube International Holding B.V., 2008.

[60] D. D.-C. Lu, D. K.-W. Cheng, and Y.-S. Lee, "A single-switch continuous-conduction-mode boost converter with reduced reverse-recovery and switching losses," *IEEE Trans. Ind. Electron.*, vol. 50, no. 4, pp. 767–776, 2003.

[61] M. M. Jovanovic and Y. Jang, "State-of-the-art, single-phase, active power-factor-correction techniques for high-power applications - an overview," *IEEE Trans. Ind. Electron.*, vol. 52, no. 3, pp. 701–708, 2005.

[62] R. W. Erickson and D. Maksimovic, *Fundamentals of power electronics*. London, UK: Springer London Ltd., 2 ed., 2001.

[63] O. D. Patterson and D. M. Divan, "Pseudo-resonant full bridge DC/DC converter," *IEEE Trans. Power Electron.*, vol. 6, no. 4, pp. 671–678, 1991.

[64] J. de Boeij, E. Lomonova, J. Duarte, and A. Vandenput, "Contactless energy transfer to a moving actuator," in *Rec. 2006 IEEE Industry Applications Conference*, vol. 4, (Tampa, FL), pp. 2020–2025, 2006.

[65] C.-S. Lin, S.-G. Lin, C.-F. Chang, H.-H. Li, and T.-R. Chen, "Model of contactless power transfer system for linear track," in *Proc. 2009 IEEE Int. Conf. Power Electronics and Drive Systems*, (Taipei, Taiwan), pp. 1075–1079, 2009.

[66] F. F. A. van der Pijl, M. Castilla, and P. Bauer, "Adaptive sliding-mode control for a multiple-user inductive power transfer system without need for communication," *IEEE Trans. Ind. Electron.*, vol. 60, no. 1, pp. 271–279, 2013.

[67] J. Smeets, T. Overboom, J. Jansen, and E. Lomonova, "Modeling framework for contactless energy transfer systems for linear actuators," *IEEE Trans. Ind. Electron.*, vol. 60, no. 1, pp. 391–399, 2013.

[68] J. de Boeij, E. Lomonova, and A. Vandenput, "Contactless energy transfer to a moving load part I : topology synthesis and FEM simulation," in *Proc. 2006 IEEE Int. Symp. Industrial Electronics*, (Montreal, Canada), pp. 739–744, 2006.

[69] R. Trevisan and A. Costanzo, "A 1-kW contactless energy transfer system based on a rotary transformer for sealing rollers," *IEEE Trans. Ind. Electron.*, vol. 61, pp. 6337–6345, Nov 2014.

[70] J. Smeets, L. Encica, and E. Lomonova, "Comparison of winding topologies in a pot core rotating transformer," in *Proc. 2010 IEEE 12th Int. Conf. Optimization of Electrical and Electronic Equipment*, (Brasov, Romania), pp. 103–110, 2010.

[71] U. Madawala and D. Thrimawithana, "A bidirectional inductive power interface for electric vehicles in V2G systems," *IEEE Trans. Ind. Electron.*, vol. 58, no. 10, pp. 4789–4796, 2011.

[72] R. Redl, L. Balogh, and D. W. Edwards, "Optimum ZVS full-bridge DC/DC converter with PWM phase-shift control: analysis, design considerations, and experimental results," in *Proc. 1994 IEEE 9th Annu. Applied Power Electronics Conf. and Expo.*, (Orlando, FL), pp. 159–165 vol.1, 1994.

[73] Y. Jang, M. M. Jovanovic, and Y.-M. Chang, "A new ZVS-PWM full-bridge converter," *IEEE Trans. Power Electron.*, vol. 18, no. 5, pp. 1122–1129, 2003.

[74] Y. Jang and M. M. Jovanovic, "A new family of full-bridge ZVS converters," *IEEE Trans. Power Electron.*, vol. 19, no. 3, pp. 701–708, 2004.

[75] Y. Jang, S. Member, and M. M. Jovanovic, "A new PWM ZVS full-bridge converter," *IEEE Trans. Power Electron.*, vol. 22, no. 3, pp. 987–994, 2007.

[76] G. Covic, J. Boys, M. Kissin, and H. Lu, "A three-phase inductive power transfer system for roadway-powered vehicles," *IEEE Trans. Ind. Electron.*, vol. 54, pp. 3370–3378, Dec 2007.

[77] M. Budhia, J. Boys, G. Covic, and C.-Y. Huang, "Development of a single-sided flux magnetic coupler for electric vehicle IPT charging systems," *IEEE Trans. Ind. Electron.*, vol. 60, no. 1, pp. 318–328, 2013.

[78] M. K. Kazimierczuk and D. Czarkowski, *Resonant power converters.* John Wiley & Sons, 2012.

[79] M. Kazimierczuk and A. Abdulkarim, "Current-source parallel-resonant DC/DC converter," *IEEE Trans. Ind. Electron.*, vol. 42, pp. 199–208, Apr 1995.

[80] M. Kazimierczuk and R. Cravens, "Current-source parallel-resonant DC/AC inverter with transformer," *IEEE Trans. Power Electron.*, vol. 11, pp. 275–284, Mar 1996.

[81] B. Yuan, X. Yang, X. Zeng, J. Duan, J. Zhai, and D. Li, "Analysis and design of a high step-up current-fed multiresonant DC-DC converter with low circulating energy and zero-current switching for all active switches," *IEEE Trans. Ind. Electron.*, vol. 59, pp. 964–978, Feb 2012.

[82] T.-P. Hung, A. Metzger, P. Zampardi, M. Iwamoto, and P. Asbeck, "Design of high-efficiency current-mode class-D amplifiers for wireless handsets," *IEEE Trans. Microw. Theory Techn.*, vol. 53, pp. 144–151, Jan 2005.

[83] A. Hu, G. Covic, and J. Boys, "Direct ZVS start-up of a current-fed resonant inverter," *IEEE Trans. Power Electron.*, vol. 21, pp. 809–812, May 2006.

[84] G. Dimitrakakis and E. Tatakis, "Analysis and design of a current-fed resonant inverter for sinusoidal excitation of magnetic components in the megahertz range," *IEEE Trans. Ind. Electron.*, vol. 58, pp. 5411–5423, Dec 2011.

[85] C.-S. Wang, G. Covic, and O. Stielau, "Investigating an LCL load resonant inverter for inductive power transfer applications," *IEEE Trans. Power Electron.*, vol. 19, pp. 995–1002, July 2004.

[86] M. Kissin, C.-Y. Huang, G. Covic, and J. Boys, "Detection of the tuned point of a fixed-frequency LCL resonant power supply," *IEEE Trans. Power Electron.*, vol. 24, pp. 1140–1143, April 2009.

[87] M. Borage, S. Tiwari, and S. Kotaiah, "Analysis and design of an LCL-T resonant converter as a constant-current power supply," *IEEE Trans. Ind. Electron.*, vol. 52, pp. 1547–1554, Dec 2005.

[88] M. Borage, S. Tiwari, and S. Kotaiah, "LCL-T resonant converter with clamp diodes: a novel constant-current power supply with inherent constant-voltage limit," *IEEE Trans. Ind. Electron.*, vol. 54, pp. 741–746, April 2007.

[89] M. Borage, K. Nagesh, M. Bhatia, and S. Tiwari, "Design of LCL-T resonant converter including the effect of transformer winding capacitance," *IEEE Trans. Ind. Electron.*, vol. 56, pp. 1420–1427, May 2009.

[90] R. Trevisan and A. Costanzo, "Exploitation of passive RFID technology for wireless read-out of temperature sensors," in *Proc. 2014 IEEE RFID Technology and Applications Conf.*, (Tampere, Finland), pp. 150–154, Sept 2014.

[91] X. Zhang, J. Yan, B. Vermeire, F. Shadman, and J. Chae, "Passive wireless monitoring of wafer cleanliness during rinsing of semiconductor wafers," *Sensors Journal, IEEE*, vol. 10, pp. 1048–1055, June 2010.

[92] G. De Vita and G. Iannaccone, "Design criteria for the RF section of UHF and microwave passive RFID transponders," *IEEE Trans. Microw. Theory Techn.*, vol. 53, pp. 2978–2990, Sept 2005.

[93] Z. Safarian and H. Hashemi, "Wirelessly powered passive systems with dynamic energy storage mechanism," *IEEE Trans. Microw. Theory Techn.*, vol. 62, pp. 1012–1021, April 2014.

[94] D. Girbau, A. Ramos, A. Lazaro, S. Rima, and R. Villarino, "Passive wireless temperature sensor based on time-coded UWB chipless RFID tags," *IEEE Trans. Microw. Theory Techn.*, vol. 60, pp. 3623–3632, Nov 2012.

[95] S. Capdevila, L. Jofre, J.-C. Bolomey, and J. Romeu, "RFID multiprobe impedance-based sensors," *IEEE Trans. Instrum. Meas.*, vol. 59, pp. 3093–3101, Dec 2010.

[96] W.-S. Chung and K. Watanabe, "A temperature difference-to-frequency converter using resistance temperature detectors," *IEEE Trans. Instrum. Meas.*, vol. 39, pp. 676–677, Aug 1990.

[97] C. Occhiuzzi, C. Paggi, and G. Marrocco, "Passive RFID strain-sensor based on meander-line antennas," *IEEE Trans. Antennas Propag.*, vol. 59, pp. 4836–4840, Dec 2011.

[98] P. Nikitin and K. Rao, "Theory and measurement of backscattering from RFID tags," *IEEE Antennas Propagat. Mag.*, vol. 48, pp. 212–218, Dec 2006.

[99] G. Marrocco, L. Mattioni, and C. Calabrese, "Multiport sensor RFIDs for wireless passive sensing of objects—Basic theory and early results," *IEEE Trans. Antennas Propag.*, vol. 56, pp. 2691–2702, Aug 2008.

[100] C. A. Balanis, *Antenna Theory: Analysis and Design.* Hoboken, NJ: John Wiley & Sons, Inc., 3 ed., 2005.

[101] C. A. Balanis, *Advanced Engineering Electromagnetics.* Hoboken, NJ: John Wiley & Sons, Inc., 2 ed., 2012.

[102] A. Ramos, A. Lazaro, D. Girbau, and R. Villarino, "Time-domain measurement of time-coded UWB chipless RFID tags," *Progress In Electromagnetics Research*, vol. 116, no. 1, pp. 313–331, 2011.

[103] H. Solar, A. Beriain, I. Zalbide, E. d'Entremont, and R. Berenguer, "A robust, -40deg to +150degC wireless rotor temperature monitoring system based on a fully passive UHF RFID sensor tag," in *Proc. 2014 IEEE MTT-S Int. Microwave Symp.*, (Tampa, FL), pp. 1–3, June 2014.

[104] S. Shrestha, M. Balachandran, M. Agarwal, V. Phoha, and K. Varahramyan, "A chipless RFID sensor system for cyber centric monitoring applications," *IEEE Trans. Microw. Theory Techn.*, vol. 57, pp. 1303–1309, May 2009.

[105] A. Ramos, D. Girbau, A. Lazaro, A. Collado, and A. Georgiadis, "Solar-powered wireless temperature sensor based on UWB RFID with self-calibration," *Sensors Journal, IEEE*, vol. 15, pp. 3764–3772, July 2015.

[106] D. Pozar, *Microwave Engineering*, ch. 2, p. 57. Wiley, 4th ed., 2011.

[107] D. Masotti, A. Costanzo, P. Francia, M. Filippi, and A. Romani, "A load-modulated rectifier for RF micropower harvesting with start-up strategies," *IEEE Trans. Microw. Theory Techn.*, vol. PP, no. 99, pp. 1–11, 2014.

[108] D. M. Pozar, *Microwave Engineering*. Boston, MA: Wiley, 4th ed. ed., 2011.

[109] K. Sawa, S. Kakino, K. Endo, G. Ou, and H. Hagino, "Degradation process of a sliding system with Au-plated slip-ring and AgPd

brush for power supply," in *Proc. 51st IEEE Holm Conf. on Electrical Contacts*, (Chicago, IL), pp. 312–317, 2005.

[110] M. Perrottet, *Transmission électromagnétique rotative d'énergie et d'information sans contact.* Ph.d. dissertation, Département d'Électricité, École Polytechnique Fédérale de Lausanne, Lausanne, Switzerland, 2000.

[111] T. C. Beh, M. Kato, T. Imura, S. Oh, and Y. Hori, "Automated impedance matching system for robust wireless power transfer via magnetic resonance coupling," *IEEE Trans. Ind. Electron.*, vol. 60, no. 9, pp. 3689–3698, 2013.

[112] J.-Y. Lee, H.-Y. Shen, and K.-C. Chan, "Design and implementation of removable and closed-shape dual-ring pickup for contactless linear inductive power track system," *IEEE Trans. Ind. Appl.*, vol. 50, pp. 4036–4046, Nov 2014.

[113] A. Pacini, F. Mastri, R. Trevisan, A. Costanzo, and D. Masotti, "Theoretical and experimental characterization of moving wireless power transfer systems," in *2016 10th European Conf. on Antennas and Propagation*, (Davos, Switzerland), April 2016.

[114] A. Pacini, F. Mastri, R. Trevisan, D. Masotti, and A. Costanzo, "Geometry optimization of sliding inductive links for position-independent wireless power transfer," in *Proc. 2014 IEEE MTT-S Int. Microwave Symp.*, (San Francisco, CA), May 2016.

[115] R. Trevisan and A. Costanzo, "Exploitation of capacitive coupling at UHF for remote sensing in a kW WPT system," in *Proc. 2015 IEEE European Microwave Conference*, (Paris, France), pp. 490–493, Sept 2015.

[116] A. Kawamura, S. Member, K. Ishioka, and J. Hirai, "Wireless transmission of power and information through one high-frequency resonant ac link inverter for robot manipulator applications," *IEEE Trans. Ind. Appl.*, vol. 32, no. 3, pp. 503–508, 1996.

[117] T. Bieler, M. Perrottet, V. Nguyen, and Y. Perriard, "Contactless power and information transmission," *IEEE Trans. Ind. Appl.*, vol. 38, no. 5, pp. 1266–1272, 2002.

[118] R. Trevisan and A. Costanzo, "Wireless sensing and power transfer in a rotary tool," in *Proc. 2015 IEEE MTT-S Int. Microwave Symp.*, (Phoenix, AZ), pp. 1–4, May 2015.

[119] J. Pendry, A. Holden, D. Robbins, and W. Stewart, "Magnetism from conductors and enhanced nonlinear phenomena," *IEEE Trans. Microw. Theory Techn.*, vol. 47, pp. 2075–2084, Nov 1999.

[120] T. Thai, F. Chebila, J. Mehdi, P. Pons, H. Aubert, G. DeJean, M. Tentzeris, and R. Plana, "A novel passive ultrasensitive RF temperature transducer for remote sensing and identification utilizing radar cross sections variability," in *Proc. 2010 IEEE Antennas and Propagation Soc. Int. Symp.*, (Toronto, ON, Canada), pp. 1–4, July 2010.

[121] J. Dong and X. Li, "UHF near-field tags design based on split ring resonator," in *Proc. 2011 IEEE Asia-Pacific Microwave Conf.*, (Melbourne, Australia), pp. 1794–1797, Dec 2011.

[122] J. Baena, J. Bonache, F. Martin, R. Sillero, F. Falcone, T. Lopetegi, M. Laso, J. Garcia-Garcia, I. Gil, M. Portillo, and M. Sorolla, "Equivalent-circuit models for split-ring resonators and complementary split-ring resonators coupled to planar transmission

lines," *IEEE Trans. Microw. Theory Techn.*, vol. 53, pp. 1451–1461, April 2005.

[123] M. Shamonin, E. Shamonina, V. Kalinin, and L. Solymar, "Resonant frequencies of a split-ring resonator: Analytical solutions and numerical simulations," *Microwave and Optical Technology Letters*, vol. 44, no. 2, pp. 133–136, 2005.

[124] J. Naqui, A. Fernandez-Prieto, M. Duran-Sindreu, F. Mesa, J. Martel, F. Medina, and F. Martin, "Common-mode suppression in microstrip differential lines by means of complementary split ring resonators: theory and applications," *IEEE Trans. Microw. Theory Techn.*, vol. 60, pp. 3023–3034, Oct 2012.

[125] V. Zhurbenko, T. Jensen, V. Krozer, and P. Meincke, "Analytical model of planar double split ring resonator," in *Proc. 2007 IEEE MTT-S Microwave and Optoelectronics Conf.*, (Brazil), pp. 753–756, Oct 2007.